

DTIC FILE COPY

2

RIVERSIDE RESEARCH INSTITUTE



330 West 42nd Street / New York, New York 10036 / (212) 563-4545

AD-A221 380

20 April 1990

FINAL TECHNICAL REPORT FR-1/C49-701
INNOVATIVE TECHNIQUES FOR HIGH-RESOLUTION
IMAGING AND PRECISION TRACKING

Report Submitted to:

DTIC
ELECTE
MAY 09 1990
S E D

Department of the Navy
Office of Naval Research
495 Summer Street
Boston, MA 02210

Office of Naval Research
Applied Physics Field Division
800 N. Quincy Street
Arlington, VA 22217-5000

Attn: Dr. Robert J. Mongeon
ONR/Boston

Attn: Dr. Matthew B. White
Code 126

This report is submitted in compliance with
CDRL Seq. No. A002 under Contract No. N00014-89-C-0124.

The views and findings of this report are those of the
Riverside Research Institute and should not be disclosed - in
whole or in part - outside the Government without the
permission of the Office of Naval Research and the Riverside
Research Institute.

REPRODUCED FROM
BEST AVAILABLE COPY

90 03 03 225

REPORT DOCUMENTATION PAGE			Form Approved OMB No. 0704-0188	
<small>Public reporting burden for this collection of information is estimated to average 1 hour per response, including the time for reviewing instructions, searching existing data sources, gathering and maintaining the data needed, and completing and reviewing the collection of information. Send comments regarding this burden estimate or any other aspect of this collection of information, including suggestions for reducing this burden, to Washington Headquarters Service, Directorate for Information Operations and Reports, 1215 Jefferson Davis Highway, Suite 1204, Arlington, VA 22202-4302, and to the Office of Management and Budget, Paperwork Reduction Project (0704-0188), Washington, DC 20503.</small>				
1. AGENCY USE ONLY (Leave Blank)	2. REPORT DATE 20 April 1990	3. REPORT TYPE AND DATES COVERED Final		
4. TITLE AND SUBTITLE Innovative Techniques for High-Resolution Imaging and Precision Tracking			5. FUNDING NUMBERS Contract No: N00014-89-C-0124	
6. AUTHOR(S) J. Nowakowski, D. Gutkowicz-Krusin, G. Lind				
7. PERFORMING ORGANIZATION NAME(S) AND ADDRESS(ES) Riverside Research Institute 330 West 42nd Street New York, NY 10036			8. PERFORMING ORGANIZATION REPORT NUMBER <i>RRI</i> FR-1/C49-701	
9. SPONSORING/MONITORING AGENCY NAME(S) AND ADDRESS(ES) Office of Naval Research Department of the Navy 800 N. Quincy Street Arlington, VA 22217			10. SPONSORING/MONITORING AGENCY REPORT NUMBER	
11. SUPPLEMENTARY NOTES				
12a. DISTRIBUTION/AVAILABILITY STATEMENT The views and findings of this report are those of the Riverside Research Institute and should not be disclosed - in whole or in part - outside the Government without the permission of the Office of Naval Research and the Riverside Research Institute.			12b. DISTRIBUTION CODE	
13. ABSTRACT (Maximum 200 words) <p>Collection of quantitative data on signatures of space objects requires knowledge of atmospheric transmission at the geographical site of interest. A method for direct measurement utilizing a unique real-time multipath laser radar is described.</p> <p>Techniques are analytically evaluated for optical autodyne detection which offers the potential of improving the performance of passive and conventional active sensors in detection, recognition and tracking. Optical autodyne detection is a direct detection method for measuring relative Doppler shifts using a coherent laser illuminator. Various frequency components of the received optical signal are mixed together on a square law photodetector to produce an output containing the spectrum of frequencies related to the relative velocity spectrum of the target and background components.</p> <p>Fundamental limits are established for the accuracy of the estimation of range and velocity resolution for autodyne detection of a two point target with a pulsed laser radar. The Cramer-Rao bounds were computed for both the signal shot noise and background limited cases.</p>				
14. SUBJECT TERMS Laser Radar, Autodyne Tracking, Doppler Tracking, Atmospheric Extinction Coefficients, (E.C.)			15. NUMBER OF PAGES 82	
			16. PRICE CODE	
17. SECURITY CLASSIFICATION OF REPORT Unclassified	18. SECURITY CLASSIFICATION OF THIS PAGE Unclassified	19. SECURITY CLASSIFICATION OF ABSTRACT Unclassified	20. LIMITATION OF ABSTRACT SAR	

RIVERSIDE RESEARCH INSTITUTE

AUTHORIZATION

This report describes research performed by Riverside Research Institute under Contract No. N00014-89-C-0124 sponsored by the Office of Naval Research.

This report was prepared by J. Nowakowski, D. Gutkowitz-Krusin, G. Lind.

Submitted by:

Jerry Nowakowski
J. Nowakowski
Member, Research Staff

Approved by:

D. Pollock
D. Pollock
Vice President, Research



STATEMENT "A" per Dr. M. White
ONRDET Boston/Code 126, 495 Sumner St.,
Boston, MA 02210-2109
TELECON 5/8/90 VG

Accession For	
NTIS GRA&I	<input checked="" type="checkbox"/>
DTIC TAB	<input type="checkbox"/>
Unannounced	<input type="checkbox"/>
Justification	
By _____	
Distribution/ _____	
Availability Codes	
Dist	Avail and/or Special
A-1	

TABLE OF CONTENTS

<u>SEC. NO.</u>	<u>DESCRIPTION</u>	<u>PAGE</u>
1.	INTRODUCTION AND SUMMARY	1
1.1	Introduction	1
1.2	Summary	3
1.3	References	6
2.	REAL-TIME MEASUREMENTS OF ATMOSPHERIC TRANSMISSION	8
2.1	Review of Techniques for Atmospheric Transmission Measurements	9
2.2	Novel Single-Ended Multipath Ladar	11
2.3	Calculations of Atmospheric Transmission and Backscattering	18
2.4	Conclusions and Recommendations	28
2.5	References	32
3.	AUTODYNE DETECTION	33
3.1	Background, Technical Approach, and Anticipated Benefits	35
3.1.1	Background	35
3.1.2	Technical Approach	36
3.1.3	Anticipated Benefits	44
3.2	Fundamental Limits on Range and Velocity Resolution for Autodyne Detection of Two Point Target	45
3.2.1	Statistics and Parametrization of Echo Signals	47
3.2.2	Performance Measures	54
3.2.3	Expressions Used In Numerical Calculations	56
3.2.4	Discussion of Results	60
3.2.5	Summary and Conclusions	77
3.3	References	80
	Appendix 1	82

RIVERSIDE RESEARCH INSTITUTE

LIST OF FIGURES

<u>SEC. NO.</u>	<u>DESCRIPTION</u>	<u>PAGE</u>
Fig. 2.1	Schematic illustration of the multipath ladar for real-time measurements of atmospheric transmission and scattering	13
Fig. 2.2	Minimum angular separation of two beams in the multipath ladar for $\epsilon = 0.1$.	16
Fig. 2.3	Horizontal separation of two beams in the multipath ladar in units of altitude z for $\epsilon = 0.1$ (minimum value = ϵ).	17
Fig. 2.4	<u>Two-way atmospheric transmission at 0.53 μm</u> calculated with LOWTRAN7 for Mid-Latitude Summer Atmosphere (30° elevation angle).	21
Fig. 2.5	<u>Two-way atmospheric transmission at 0.7 μm</u> calculated with LOWTRAN7 for Mid-Latitude Summer Atmosphere (30° elevation angle).	22
Fig. 2.6	<u>Two-way atmospheric transmission at 1.06 μm</u> calculated with LOWTRAN7 for Mid-Latitude Summer Atmosphere (30° elevation angle).	23
Fig. 2.7	<u>Two-way transmission at 3.0 μm</u> calculated with LOWTRAN7 for Mid-Latitude Summer Atmosphere (30° elevation angle). <u>Note that the vertical scale is from 0 to 1%.</u>	24
Fig. 2.8	<u>Two-way atmospheric transmission at 5.0 μm</u> calculated with LOWTRAN7 for Mid-Latitude Summer Atmosphere (30° elevation angle). <u>Note that the vertical scale is from 0 to 0.2%.</u>	25
Fig. 2.9	<u>Two-way atmospheric transmission at 10.6 μm</u> calculated with LOWTRAN7 for Mid-Latitude Summer Atmosphere (30° elevation angle).	26
Fig. 2.10	<u>Two-way atmospheric transmission at 10.6 μm</u> calculated with LOWTRAN7 for 1976 U.S. Standard Atmosphere (30° elevation angle).	27

RIVERSIDE RESEARCH INSTITUTE

LIST OF FIGURES (Cont'd)

<u>SEC. NO.</u>	<u>DESCRIPTION</u>	<u>PAGE</u>
Fig. 2.11	Fraction of transmitted energy collected by the ladar receiver as a function of altitude for <u>different zenith angles and $\lambda = 0.53 \mu\text{m}$.</u>	29
Fig. 2.12	Fraction of transmitted energy collected by the ladar receiver as a function of altitude for <u>different zenith angles and $\lambda = 1.06 \mu\text{m}$.</u>	30
Fig. 3.1	Echo signal patterns from two equal strength, stationary backscatters, with changing values of separation. <u>Solid line phase angle $\Psi = 90^\circ$; dotted line - phase angle $\Psi = 180^\circ$ for this and all subsequent figures (3.1 - 3.13).</u>	52
Fig. 3.2	Echo signal patterns from two equal strength, moving backscatters with changing values of relative velocity and separation value of zero.	52
Fig. 3.3	Echo signal patterns from two equal strength backscatters; selected values of separation and relative velocity.	53
Fig. 3.4	Dependence of scaled CRB (\hat{tdd}) on temporal separation of two point targets of equal strength; selected cases for different values of relative velocity. <u>Signal shot noise limited conditions.</u>	62
Fig. 3.5	Dependence of scaled CRB (\hat{tdd}) on temporal separation of two point targets of equal strength; selected cases for different values of relative velocity. <u>Background shot noise limited conditions.</u>	63
Fig. 3.6	Dependence of scaled CRB (\hat{vd}) on temporal separation of two point targets of equal strength; selected cases for different values of relative velocity. <u>Signal shot noise limited conditions.</u>	64
Fig. 3.7	Dependence of scaled CRB (\hat{vd}) on temporal separation of two point targets of equal strength; selected cases for different values of relative velocity. <u>Background shot noise limited conditions.</u>	65
C49-701		

LIST OF FIGURES (Cont'd)

<u>SEC. NO.</u>	<u>DESCRIPTION</u>	<u>PAGE</u>
Fig. 3.8	Dependence of scaled CRB ($\hat{t}d$) on temporal separation of two point targets of equal strength; selected cases for different values of relative velocity. <u>Signal shot noise limited conditions.</u>	66
Fig. 3.9	Dependence of scaled CRB ($\hat{t}d$) on temporal separation of two point targets of equal strength; selected cases for different values of relative velocity. <u>Background shot noise limited conditions.</u>	67
Fig. 3.10	Dependence of scaled CRB ($\hat{v}d$) and CRB ($t\hat{d}d$) on temporal separation of two point targets of differing strength; selected cases for different values of relative velocity. <u>Signal shot noise limited conditions.</u>	73
Fig. 3.11	Dependence of scaled CRB ($\hat{v}d$) and CRB ($t\hat{d}d$) on temporal separation of two targets of differing strength; selected cases for different values of relative velocity. <u>Background shot noise limited conditions.</u>	74
Fig. 3.12	Dependence of scaled CRB ($\hat{v}d$) and CRB ($t\hat{d}d$) on relative angular Doppler shift; of two point targets of equal strength; selected cases for different values of temporal separation. <u>Signal shot noise limited conditions.</u>	75
Fig. 3.13	Dependence of scaled CRB ($\hat{v}d$) and CRB ($t\hat{d}d$) on relative angular Doppler shift; at two point targets of different strength; selected cases for different values of temporal separation. <u>Signal shot noise limited conditions.</u>	76
Fig. 3.14	Dependence of scaled CRB ($\hat{t}d$) and CRB ($\hat{v}d$) on the number of unknown parameters. Panels A and C: phase angle $\psi = 0^\circ$; panels B and D: phase angle $\psi = 180^\circ$. For panels A and B, curve designations are: a - all parameters unknown; b - all parameters except p unknown; c - all parameters except ψ unknown; d - all parameters except p and ψ unknown (in this case identical curves are obtained if all parameters are known). For panels C and D, curve designations are: a, b, c and d - as in panels A and B; e - all parameters except $t\hat{d}$ and $t\hat{d}d$ unknown; f - all parameters are known.	78

1. INTRODUCTION AND SUMMARY

1.1 Introduction

The SDI requirements for near real-time identification, discrimination and precision tracking of boosters, post-boost vehicles, and midcourse targets present a formidable technological challenge. As discussed below there are many situations where the performance requirements cannot be met with conventional imaging and tracking systems and innovative techniques are needed.

For example, recent data on booster plume and hardbody signatures suggest that many of the conventional passive and active fine tracking schemes are inadequate¹⁻⁴. RRI's study for STARLAB indicates that the technical value of near-term space-based demonstrations must be enhanced through a broader-scope experimental program directed toward assessing the feasibility of precision tracking and pointing concepts. Due to an insufficient data base on booster signatures, the feasibility of crucial passive-to-active handover functions with sufficient accuracy is yet to be demonstrated; the hardware requirements for passive and active trackers are yet to be credibly defined; and the tracking and fire control algorithms are yet to be developed.

For PBV's and midcourse targets, there is the well known problem that conventional monostatic laser radars can be easily "blinded" by simple optical countermeasures such as corner cubes. These countermeasures have forced the use of bistatic laser radar architectures, which significantly increase their cost and complexity. In addition, the feasibility of bistatic ladars for DEW applications has not been evaluated, particularly in terms of integration and boresighting with the weapon platform.

Typically, innovative techniques are the result of: 1) Newly found properties of target signatures, e.g., spatio-temporal fluctuations of passive booster plume signatures^{2,3}, or

RIVERSIDE RESEARCH INSTITUTE

radiation scattering by solid-fuel booster plumes in the UV, the visible, and the near IR^{1,4}; 2) Newly developed hardware components, e.g., coherent medium-power lasers operating in the UV or in the visible; 3) New algorithms for extracting the target information which constitute the basis for novel receiver structures, e.g., laser correlography,^{5,6} imaging correlography,⁷ autodyne⁸ and image texture tracking⁹, self-reference holography¹⁰, etc.

RRI has made major contributions towards a realistic assessment of the feasibility of active high-resolution imaging for target identification and precision tracking of interest to SDIO. Our research produced the first quantitative characterization of passive and active booster signatures²⁻⁴, which was then used by the SDIO community to predict the performance of conventional fine tracking of boosters. This performance analysis led to the conclusion that in numerous cases conventional techniques are not adequate and innovative approaches are necessary.

Riverside Research Institute proposed three novel techniques for fine tracking to meet the unprecedented performance requirements: Autodyne and Image Texture Tracking for boosters and Coherent-Radiation Imaging and Tracking via Illumination Coding (CRITIC) for robust imaging and tracking of post-boost and midcourse targets and satellites. These techniques are described in detail in Section 3 and Appendix 1 and can be demonstrated using the IST ground-based experimental facilities.

The challenge facing the IST is to develop, test, and select the techniques or sensor systems for operational space conditions based on experiments performed with the ground-based sensors. Thus, one will have to develop the experimental field facilities of interest to the IST (the ISTEf in Florida and the Downrange in Puerto Rico) to a state-of-the-art level which will allow them to meet the following interrelated objectives: 1) to collect high-resolution signature data on targets of interest and 2) to perform proof-of-concept experiments with both innovative and conventional systems. To meet the above objectives one has to design experiments such that their results will be conclusive and scalable to operational

RIVERSIDE RESEARCH INSTITUTE

conditions. In Section 2 we describe a novel lidar concept, developed during RRI's evaluation of IST facilities, that offers the potential for real-time measurements of atmospheric transmission. This technique will be important for addressing scalability issues. Realistic estimations of detection performance of ladars against threats is dependent upon knowing atmospheric transmission over the slant path of the encounter geometry. Consequently, atmospheric extinction coefficient is a parameter which needs evaluation to support estimations and interpretations of test results.

1.2 Summary

Collection of quantitative data on signatures of space objects requires knowledge of atmospheric transmission at the geographical site of interest. Many different techniques for measuring atmospheric transmission have been developed. In general, direct measurements of transmission as a function of altitude require an airborne transmitter or receiver and are, therefore difficult to carry out in real time. Remote sensing of the atmosphere by single-ended ladars avoids this difficulty, but at a price of often unjustified assumptions about extinction and backscattering coefficients. The recent lidar techniques which avoid such assumptions have other types of difficulties.

Review of different techniques for transmission measurements led to the conclusion that such measurements are either difficult to implement in real time, or require untested assumptions about the nature of extinction, scattering, or multiple scattering. Therefore, we began the development of a novel real-time multipath lidar. The main disadvantage of this multipath lidar, common to all remote sensing ladars, is that the signal may be limited by weak scattering at high altitudes. On the other hand, it has many advantages. It is very simple and except for the steering mechanism can be built with off-the-shelf hardware. Measurements can be made in real time. Simple data processing is required to obtain the values of transmission coefficient as a function of range without a priori assumptions about scattering

RIVERSIDE RESEARCH INSTITUTE

and extinction and absolute calibration is not required. The multipath lidar can be tested by varying the beam azimuth angle for a fixed zenith angle. Radiation scattered by horizontally homogeneous atmosphere is independent of the azimuth angle. Therefore, comparisons between the signals returned for different azimuth angles can be used to determine the characteristic length scales for horizontal inhomogeneities in scatterer properties at different altitudes.

Sizing of ground-based active systems for the detection of space objects and of the proposed multipath requires information about the atmospheric transmission. In the absence of data collected at a site of interest, LOWTRAN7 was used to estimate atmospheric transmission as a function of range for different wavelengths. In addition, molecular contribution to the backscattering was calculated in the Rayleigh limit and aerosol contribution using the Mie scattering for standard atmospheric models. At present, the validity of these models cannot be assessed. A detailed discussion of this research is provided in Section 2.0.

In Section 3 we evaluate optical autodyne detection techniques which offer the potential of improving the performance of passive and conventional active sensors in detection, recognition and tracking. The autodyne technique can be applied against ground and aerospace targets in a variety of scenarios as well as for booster and satellite imaging and tracking. The work presented here is part of a continuing effort to develop an analytic framework for the detection and parameter estimation of autodyne signals. The analysis is applicable in a variety of scenarios involving rotating (or vibrating) satellites, or in tracking the booster hardbody-plume interface. This analysis will be useful in providing a framework for evaluating other techniques based on: light intensity interferometry such as correlography; techniques applicable to diffuse and complex targets with strong specular components; and will be extended to the more general case of spatio-temporal light intensity interferometry where correlography and autodyning are limiting special cases.

Optical autodyne detection is a direct detection method for measuring relative Doppler shifts using a coherent laser illuminator. Various frequency components of the received optical signal are mixed together on a square-law photodetector to produce an output containing the spectrum of frequencies related to the relative velocity spectrum of the target and background components. The main advantage of autodyne detection, as compared with the usual heterodyning techniques, is its simplicity; a local oscillator is not necessary. The increased robustness of an autodyne system makes it attractive for many applications. Such an active system may consist of a pulsed laser transmitter and a photon bucket receiver, although an array of autodyne detectors in the focal plane of the imaging sensor may also be employed. One deficiency of autodyne detection is that it provides information about the autocorrelation of functions proportional to the reflectivity of elements moving with a given radial velocity, while the heterodyne technique in principle can provide direct information about the reflectivity as a function of radial velocity. In many scenarios, however, a simple autodyne detector will provide a signature sufficiently complementing the information obtained by the passive - active sensor suite.

The results of our research are described in detail in Section 3 and summarized below.

Fundamental limits were established for the accuracy of the estimation of range and velocity resolution for autodyne detection of a two point target with a pulsed laser radar consisting of a transmitter collocated with a photon bucket receiver. The Cramer-Rao bounds (CRB's) were computed for both the signal shot noise and background limited cases. From these bounds, the number of signal photons necessary to estimate a parameter with a desired accuracy may be determined.

The sensitivity of the bounds to different parameter values and changes in the number of unknown parameters was established. The value of a priori knowledge in parameter estimation was demonstrated and related to the number of unknown parameters. An important issue of practical consequence, which remains to be addressed in future work, is the effect of detector response time on parameter estimation of echo signals.

RIVERSIDE RESEARCH INSTITUTE

The double point target provides us with a wide parameter space. This work would be useful in introducing the natural metric in parameter space for the proper evaluation of the information content in echo signals. The bound on estimator performance was obtained for a single laser pulse. Evaluating the performance of a multipulse system is certainly of great interest and will be addressed in future efforts.

One of the important results obtained was that for a large relative Doppler shift a few tens of photons are required to measure Doppler shift with moderate accuracy. To put such predictions on a firm footing, one has to construct estimators with variances approaching the CRB. An example applicable to problems in which fine parameter estimation is of interest, e.g., alignment and calibration when the uncertainty of the parameter value is small, is provided (e.g, equation 3.41).

Another important class of estimators useful for many applications are the maximum likelihood estimators (MLE). These estimators are applicable for large parameter variations, and approach the CRB for large signal values. The methods of implementation for the MLE estimators, together with other practical considerations, and types of estimators are important problems which should be addressed in future work.

It is expected that this ongoing effort will lead to the development of a new class of autodyne sensors useful in various scenarios of practical interest. It will also help to establish which additional measurements of channel, target, and background signature are required, and what additional data related to sensor pattern selection are necessary to arrive at a realistic assessment of the feasibility of advanced sensors for IST applications.

1.3 REFERENCES

1. D. Brenner, "WSMR Signature Data Analysis", Report 87-036, Riverside Research Institute, 1987 (S)
2. D. Gutkowitz-Krusin, "Uncertainties in Low-Altitude Booster Plume Signatures in the IR", Report 87-044, Riverside Research Institute, 1987 (S)

RIVERSIDE RESEARCH INSTITUTE

3. D. Gutkowicz-Krusin, "Comparison of Temporal Properties of Missile Plumes at Low and High Altitudes", Report 87-078, Riverside Research Institute, 1987 (S)
4. D. Brenner, B. Kingsbury, and D. Gutkowicz-Krusin, "Light Scattering by Particulates in Rocket Exhaust Plumes", Report 88-036, Riverside Research Institute, 1988 (S)
5. M. Elbaum, M. King, and M. Greenbaum, "Laser correlography: Transmission of High Resolution Signatures Through the Turbulent Atmosphere", Riverside Research Institute, Technical Report T-1/306-3-11, 1974
6. P. S. Idell, J. R. Fienup, R. S. Goodman, Opt. Lett. 12, 858 (1987)
7. J. Nowakowski, Y. Gorlin, and M. Elbaum, "Imaging Correlography", preprint, 1987
8. M. Elbaum, D. Brenner, B. Kingsbury, J. Nowakowski, "Autodyning Tracking of Moving Targets Indicator", Patent Disclosure, 1988
9. M. Elbaum, D. Brenner, B. Kingsbury, J. Nowakowski, "Texture Imaging and Tracking", Patent Disclosure, 1988
10. M. Elbaum, J. Nowakowski, D. Gutkowicz-Krusin, M. Wlodawski, and Y. Gorlin, Opt. Lett. 13, 81 (1988)

2. REAL-TIME MEASUREMENTS OF ATMOSPHERIC TRANSMISSION

Knowledge of atmospheric transmission is important in many situations. For example, to detect objects in the earth's atmosphere, the wavelength of measurement is often chosen to minimize atmospheric losses along the line-of-sight (LOS). Even when detection is not a problem it may be desirable to obtain quantitative data on the radiation scattered or emitted by the object under study. In this case radiation detected must be corrected for atmospheric losses. The values of transmission (or extinction) coefficient as a function of wavelength could also be used to determine concentrations of various molecular species in the atmosphere, and to detect the presence of pollutants such as smoke. Sizing of ground-based active systems for the detection of space objects also requires information about transmission losses in the atmosphere.

Not surprisingly, many different techniques for measuring atmospheric transmission have been developed.¹⁻³ These techniques are reviewed in Sec. 2.1. In general, direct measurements of transmission as a function of altitude require an airborne transmitter or receiver and are, therefore, difficult to carry out in real time. Remote sensing of the atmosphere by single-ended lidars avoids this difficulty, but at a price of often unjustified assumptions about backscattering and extinction coefficients. The bipath lidar^{4,5}, which does not make such assumptions, requires an airborne lidar and again would be difficult to use in real time. The multiple-field-of-view lidar^{6,7} requires its own set of assumptions about multiple scattering in the atmosphere, and has not yet been tested.

Collection of quantitative data on signatures of space objects requires real-time measurements of atmospheric transmission at the geographical site of interest. In order to carry out such measurements, we began the development of a novel real-time multipath lidar which is described in detail in Sec. 2.2.

The collected knowledge of atmospheric properties is summarized in standard atmospheric models⁸. Based on these models, codes like LOWTRAN and FASCODE were

developed to predict transmission as a function of wavelength and range for a chosen LOS; some predictions of codes are discussed in Sec. 2.3. The models attempt to describe "typical" atmospheric conditions, assumed to vary only with altitude, and may be inappropriate for a particular geographic site. In addition, these static models cannot account for temporal variability of atmospheric conditions which is easily observed at low altitudes. Finally, the predicted extinction coefficient is highly sensitive to the assumed aerosol composition⁹, which is not well known and variable as well. Nevertheless, in the absence of data collected at a geographical site of interest, the available codes provide the means to estimate the values of the atmospheric transmission, which are not too far removed from the realistic values. At present, however, the validity of this assumption cannot be assessed.

Sec. 2.4 contains conclusions and recommendations.

2.1. Review of Techniques for Atmospheric Transmission Measurements

Various techniques for measuring atmospheric transmission have been reviewed in Refs. 1-3. They can be divided into three categories: contrast, transmission, and scattering measurements.

Contrast measurements determine the apparent radiance of a known target (either natural, such as sky, or artificial) and can, therefore, be used to calculate atmospheric losses. While very sensitive and portable, these "fair-weather" measurements can only be made in daylight. In addition, measurements as a function of altitude would require airborne targets.

Transmission measurements can rely on either natural or artificial sources. Measurements of starlight attenuation determine only the total optical depth of the earth atmosphere. Artificial sources (lamps or lasers) could be used at various distances from the receiver to determine transmission as a function of range. The main difficulty is the proper alignment of the transmitter and receiver. However, these measurements are most direct and

could be used to test other techniques. Again, an airborne platform for either the transmitter or receiver is required for measurements at different altitudes.

One class of scattering measurements, nephelometry, relates the unknown extinction coefficient to the scattering coefficients measured at various scattering angles. These techniques work well only if absorption is negligible. In addition, they require samples of air to perform measurements, and are, therefore, difficult to use for measurements as a function of altitude.

The other class of scattering measurements uses single-ended ladars in which the transmitter and receiver are co-located. The power returned to the receiver from radiation scattered at a range R, from the transmitter, is given by the standard ladar equation,²

$$P(R) \propto P_0 \frac{\beta(R)}{R^2} \cdot e^{-2 \int_0^R k_{\text{ext}}(z) dz} \quad (2.1)$$

where P_0 is the transmitted power, $\beta(R)$ is the volume backscattering coefficient, and $k_{\text{ext}}(R)$ is the extinction coefficient. It is evident that the measured signal $P(R)$ is a function of both β and k_{ext} ; in order to determine both of these quantities from the ladar returns, it is necessary to assume a special relationship between the extinction $k_{\text{ext}}(R)$ and backscattering $\beta(R)$.^{2,10}

It is desirable to extract both $\beta(R)$ and $k_{\text{ext}}(R)$ from the ladar data without assuming any ad hoc relationship between the two. Recently two methods have been proposed for achieving this. One is the bipath ladar^{4,5} and the other is the multiple-field-of-view ladar.^{6,7}

The bipath method employs two separate single-ended ladar systems to measure both the backscattering and extinction coefficients unambiguously. The second ladar provides a second independent equation in the two variables of interest; this set of two equations for two unknowns can be easily solved. Hughes and Paulson⁵ have shown that the backscattering and

extinction coefficients obtained from a single lidar using Klett's reconstruction algorithm¹⁰ were significantly different from those obtained with the bipath method.

Since it is often necessary to make measurements as a function of altitude, one of the lidars must be flown on a platform (either a plane or a balloon). In addition, both lidars must be calibrated. Thus, the bipath method is difficult to use for real-time measurements and a single-ended technique would be preferable.

One such single-ended method, the multiple-field-of-view lidar, has been suggested by Bissonnette et al.^{6,7} at DREV in Canada. This method makes use of information about backscattering and extinction which is contained in multiply scattered radiation returned to the receiver. Although no assumption is made about a relationship between the backscattering and extinction coefficients, Bissonnette et al. do make some assumptions about the multiple scattering contributions to the lidar signal which will have to be verified. At present this system, built by Optech in Toronto, is being tested at DREV in Canada.

2.2 Novel Single-Ended Multipath Lidar

As discussed in Sec. 2.1, lidars can sense atmospheric properties in real time. This great advantage comes at a price of often unjustified assumptions about backscattering and extinction coefficients. The bipath lidar which does not make such assumptions requires an airborne lidar and is, therefore, difficult to use in real time. The multiple-field-of-view lidar has not yet been tested and requires its own set of assumptions about multiple scattering in the atmosphere. Here we describe a novel multipath lidar which can be used in real time and which requires only some weak assumptions about horizontal inhomogeneities in the earth atmosphere.

RIVERSIDE RESEARCH INSTITUTE

Consider a standard lidar pointed along a LOS with zenith angle θ and azimuth angle ϕ . This is illustrated schematically in Fig. 2.1. Energy $E(R)$ of backscattered radiation from the range R detected by the receiver during integration time τ_D is

$$E(\lambda, R) = E_0 \frac{c \tau_D A_0}{2R^2} \zeta(\lambda) \xi(R) \beta(\lambda, R) e^{-2 \int_0^R k_{\text{ext}}(\lambda, r) dr} , \quad (2.2)$$

where E_0 is the transmitted pulse energy, A_0 is the receiver aperture, $\zeta(\lambda)$ is the receiver transmission factor, $\xi(R)$ is the geometrical form factor which depends on the transmitter and receiver geometry, and c is the speed of light. Let N_i denote the number density of scatterers (molecules or aerosols). Then the volume scattering coefficient is

$$\beta(\lambda, R) = \sum_i N_i(R) \sigma_i(\lambda, \theta^S) , \quad (2.3)$$

and extinction coefficient is

$$k_{\text{ext}}(\lambda, R) = \sum_i N_i(R) \sigma_i^{\text{ext}}(\lambda) , \quad (2.4)$$

where $\sigma_i(\lambda, \theta^S)$ is the differential scattering cross-section at an angle θ^S (usually for lidars $\theta^S = \pi$) and $\sigma_i^{\text{ext}}(\lambda)$ is the total extinction cross-section which contains contributions from both scattering and absorption.

In the coordinate system shown in Fig. 2.1

$$R = z / \cos \theta \quad (2.5)$$

and

$$x = z \tan \theta . \quad (2.6)$$

Hence, the scattering coefficient may be written as

$$\beta(R) = \beta(x, z) = \beta(z \tan \theta, z) \quad (2.7)$$

and, similarly, extinction coefficient becomes

$$k_{\text{ext}}(R) = k_{\text{ext}}(x, z) = k_{\text{ext}}(z \tan \theta, z) , \quad (2.8)$$

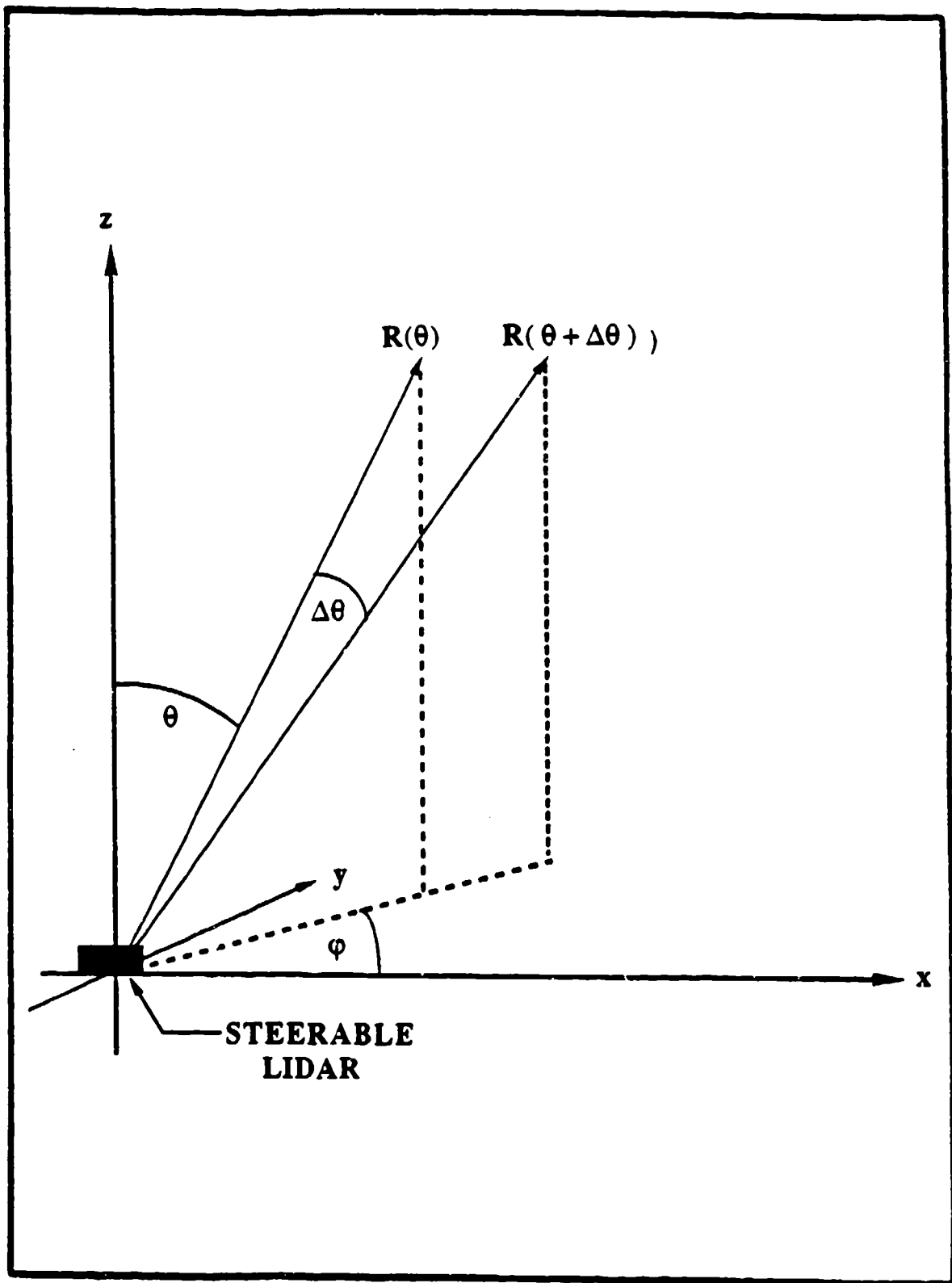


Fig. 2.1 Schematic illustration of the multipath lidar for real-time measurements of atmospheric transmission and scattering.

where the wavelength dependence is implicit. In this coordinate system the ladar equation (2.2) can be written as

$$E\left(\frac{z}{\cos\theta}\right) = E_0 \frac{c r_D}{2} \frac{A_0}{z^2} \cos^2\theta \zeta(\lambda) \xi\left(\frac{z}{\cos\theta}\right) \beta(z \tan\theta, z) \times \exp\left\{-\frac{2}{\cos\theta} \int_0^z dz' k_{\text{ext}}(z' \tan\theta, z')\right\}. \quad (2.9)$$

Consider two lines-of-sight with zenith angles θ and $\theta + \Delta\theta$, respectively. Let $\Delta\theta$ be sufficiently small so that

$$\left| \frac{\partial \ln \beta(x, z)}{\partial x} \Delta x(z) \right| \ll 1 \quad (2.10)$$

and

$$\left| \frac{\partial \ln k_{\text{ext}}(x, z)}{\partial x} \Delta x(z) \right| \ll 1, \quad (2.11)$$

where

$$\Delta x(z) \equiv z [\tan(\theta + \Delta\theta) - \tan\theta], \quad (2.12)$$

Conditions (2.10) and (2.11) indicate that the angular separation between two beams must be less than the typical angular size of horizontal inhomogeneities in the scatterer distribution and composition. These conditions are essential for the proposed multipath ladar. They are not very restrictive since horizontal inhomogeneities are expected to be most pronounced at lower altitudes where the horizontal separation between the two beams is small. At high altitudes the beam separation becomes large but the atmosphere is probably quite homogeneous at these altitudes. A technique for testing these assumptions is described later in this section.

On the other hand, let $\Delta\theta$ be large enough so that

$$\left| \frac{1}{\cos\theta} - \frac{1}{\cos(\theta + \Delta\theta)} \right| \gtrsim \epsilon, \quad (2.13)$$

RIVERSIDE RESEARCH INSTITUTE

where ϵ is a constant chosen to maximize the path length differences for the two beams subject to constraints (2.10) and (2.11).

The values of $\Delta\theta$ which satisfy condition (2.13) for $\epsilon = 0.1$ are shown in Fig. 2.2. It is seen that the required angular separation between the two beams decreases rapidly with increasing zenith angle. Since, with the exception of clouds, the characteristic length scales for horizontal inhomogeneities in the atmosphere are not known, the multipath ladar should operate at a zenith angle of about 45° . Horizontal separation between the two beams is shown in Fig. 2.3 in units of altitude as a function of zenith angle θ . It is seen that for $\theta > 45^\circ$, the horizontal separation becomes insensitive to the value of θ ; the minimum separation between the beams is ϵz .

Assuming that conditions (2.10) - (2.13) are satisfied we can determine the extinction coefficient as a function of altitude from

$$k_{\text{ext}}(z \tan \theta, z) = \frac{1}{2} \left(\frac{1}{\cos(\theta + \Delta\theta)} \frac{1}{\cos \theta} \right) \frac{\partial}{\partial z} \ln Q(z), \quad (2.14)$$

where

$$Q(z) \equiv \frac{E(z/\cos \theta)}{E(z/\cos(\theta + \Delta\theta))} \frac{\cos^2(\theta + \Delta\theta)}{\cos^2(\theta)} \frac{\xi(z/\cos(\theta + \Delta\theta))}{\xi(z/\cos \theta)}. \quad (2.15)$$

Since $Q(z)$ depends only on the ratio of the received signals, absolute calibration is not required to obtain the extinction coefficient. This is also true for the one-way transmission coefficient which is given by

$$T(R=z/\cos \theta) = [Q(z)]^{\frac{\cos(\theta + \Delta\theta)}{2[\cos(\theta + \Delta\theta) - \cos \theta]}}. \quad (2.16)$$

Given the value of the transmission coefficient, the volume scattering coefficient β can be obtained using the ladar equation (2.2). Note that this requires absolute calibration of the ladar.

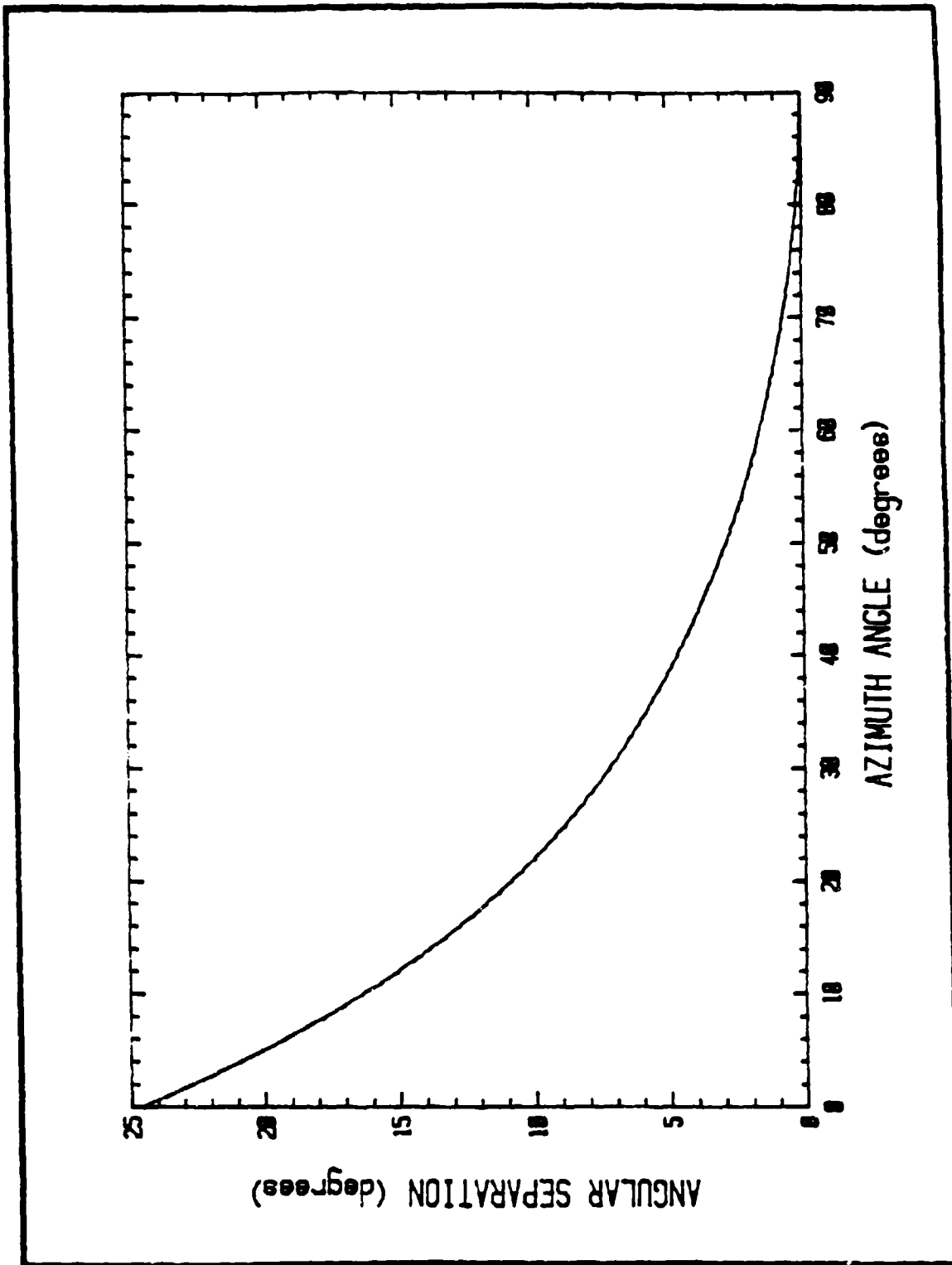


Fig. 2.2 Minimum angular separation of two beams in the multipath lidar for $\epsilon = 0.1$

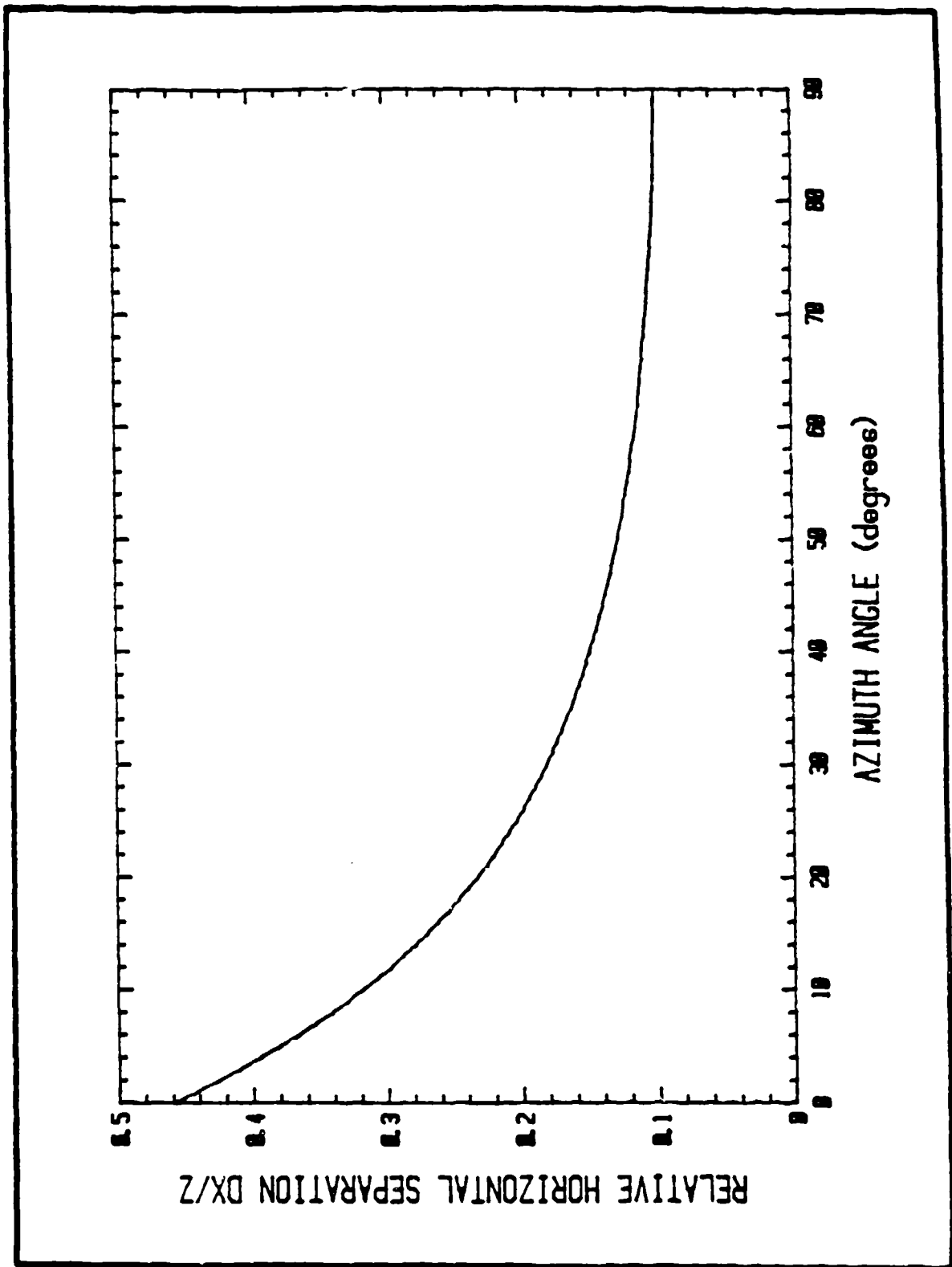


Fig. 2.3 Horizontal separation of two beams in the multipath lidar in units of altitude z for $e = 0.1$ (minimum value = e).

The formulae (2.14) and (2.16) for the extinction and transmission coefficients were derived under an additional assumption that the scattering cross-section depends on scattering angle but not on the incidence angle. This is true for spherical or randomly oriented nonspherical scatterers. This assumption may break down in the case of nonspherical particles which may be partially aligned, for example ice particles in cirrus clouds. In such cases it may become necessary to carry out measurements at higher zenith angles. Effects of such possible particle alignment on polarization (or depolarization) of scattered light should be considered.

The multipath lidar can be tested by varying the azimuth angle ϕ of the beam for a fixed value of the zenith angle θ , as shown in Fig. 2.1. Under the assumption of horizontal homogeneity, the signal received from a given altitude should be independent of the azimuth angle ϕ . Comparisons between received signals as a function of altitude and azimuth angles can be used to determine the characteristic length scales of inhomogeneities at different altitudes. The beam pointing parameters could then be adjusted in real time so that conditions (2.10) - (2.13) are satisfied during measurements. The multipath lidar could also measure scattering and extinction by inhomogeneities such as clouds provided their angular size exceeds the required angular separation between the beams. In addition, by continuing measurements as a function of the zenith angle, it may be possible to determine the two-dimensional distribution of scattering and extinction. Temporal variability could be determined on time scales which will depend on the laser pulse rate and the beam steering time.

2.3 Calculations of Atmospheric Transmission and Backscattering

In order to design the proposed multipath lidar, it is necessary to estimate that fraction of transmitted energy which will be collected by the receiver as a function of range. Clearly, this fraction depends strongly on the values of the transmission and backscattering coefficients.

RIVERSIDE RESEARCH INSTITUTE

All the transmission calculations discussed in this report were obtained using a modification of LOWTRAN7 to determine transmission coefficient at a particular wavelength as a function of range. This is not the intended use of LOWTRAN7, which was designed to calculate transmission coefficient integrated over some spectral band. For losses in propagation of laser beams it is more appropriate to use FASCODE; such calculations will be carried out in the future.

In the calculations, percentage of radiation transmitted in a round trip from the ground-based transmitter to the monostatic receiver has been determined as a function of target range along a line of sight with the elevation angle of 30° . Calculations were carried out at 0.53, 0.7, 1.06, 3.0, 5.0, and 10.6 μm . Mid-Latitude Summer Atmospheric Model was chosen, as most appropriate for the ISTEf site.

Specification of the season determines the tropospheric and background stratospheric aerosol profiles used in calculations. Volcanic aerosols in the stratosphere may also contribute to the transmission losses but have not been included in the calculations since it is not clear which model is appropriate. It should be noted, that their effect would be to reduce the calculated transmission.

In addition it was necessary to specify the nature of the boundary layer, i.e., 0 to 2 km altitude. For the location of the ISTEf site, the NAVY MARITIME model was chosen as the most appropriate one. In this model, the air mass character in the boundary layer can be varied from open ocean to strong continental influence. In order to obtain bounds on the expected value of transmission, calculations were done for both of these extreme cases.

The NAVY MARITIME model also requires specification of the meteorological range V which is defined as

$$V = 3.912/k_{\text{ext}} \quad (2.17)$$

RIVERSIDE RESEARCH INSTITUTE

where k_{ext} is the total extinction coefficient at $0.55 \mu\text{m}$. To test the sensitivity of the transmission coefficient, calculations were done for $V = 5 \text{ km}$ (low visibility) and $V = 50 \text{ km}$ (very high visibility).

The results are shown in Figs. 2.4 - 2.9, in which transmission for the continental boundary layer is shown by solid curves while for the open ocean boundary layer by dashed curves. It is seen that, according to LOWTRAN7, essentially all of the losses occur in the first 20 - 30 km from the ground and losses at 3.0 and $5.0 \mu\text{m}$ are significantly greater than at other wavelengths, due to strong absorption by water and carbon dioxide. For comparison, 1976 U.S. Standard Atmospheric Model has been used to calculate transmission at $10.6 \mu\text{m}$; the result is shown in Fig. 2.10. It should be noted that the calculated transmission is very sensitive to the choice of atmospheric model.

Backscattering in the earth's atmosphere is due to molecules and aerosols. Molecular contribution to the backscattering coefficient was calculated using the Rayleigh approximation for the 1976 U.S. Standard Atmospheric Model. The aerosol constituents of the atmosphere are not known with high accuracy and, in addition, may be highly variable, especially at low altitudes. In this report we used the aerosol models compiled in the "Handbook of Geophysics and the Space Environment" published by AFGL.⁸ The aerosol backscattering was calculated using the Mie theory.¹¹

The fraction of energy received by the lidar was estimated by assuming the following system parameters:

$$\begin{aligned}\tau_D &= 1 \mu\text{s}, \\ A_0 &= 0.1 \text{ m}^2, \\ \xi(\lambda)\xi(R) &= 0.1.\end{aligned}$$

Note that with this integration time, the lidar would be capable of range resolution of 0.15 km .

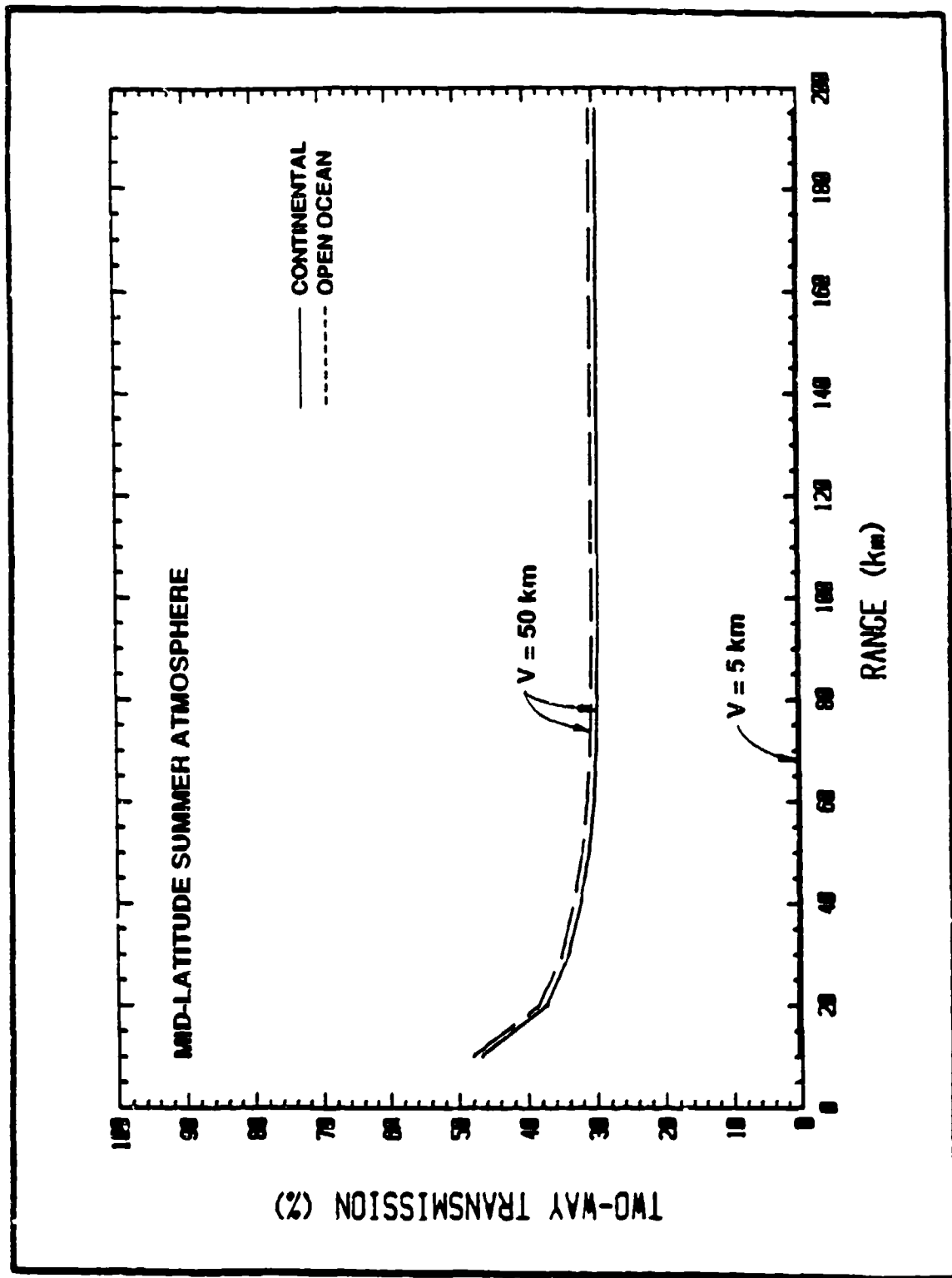


Fig. 2.4 Two-way atmospheric transmission at $0.53 \mu\text{m}$ calculated with LOWTRAN7 for Mid-Latitude Summer Atmosphere (30° elevation angle).

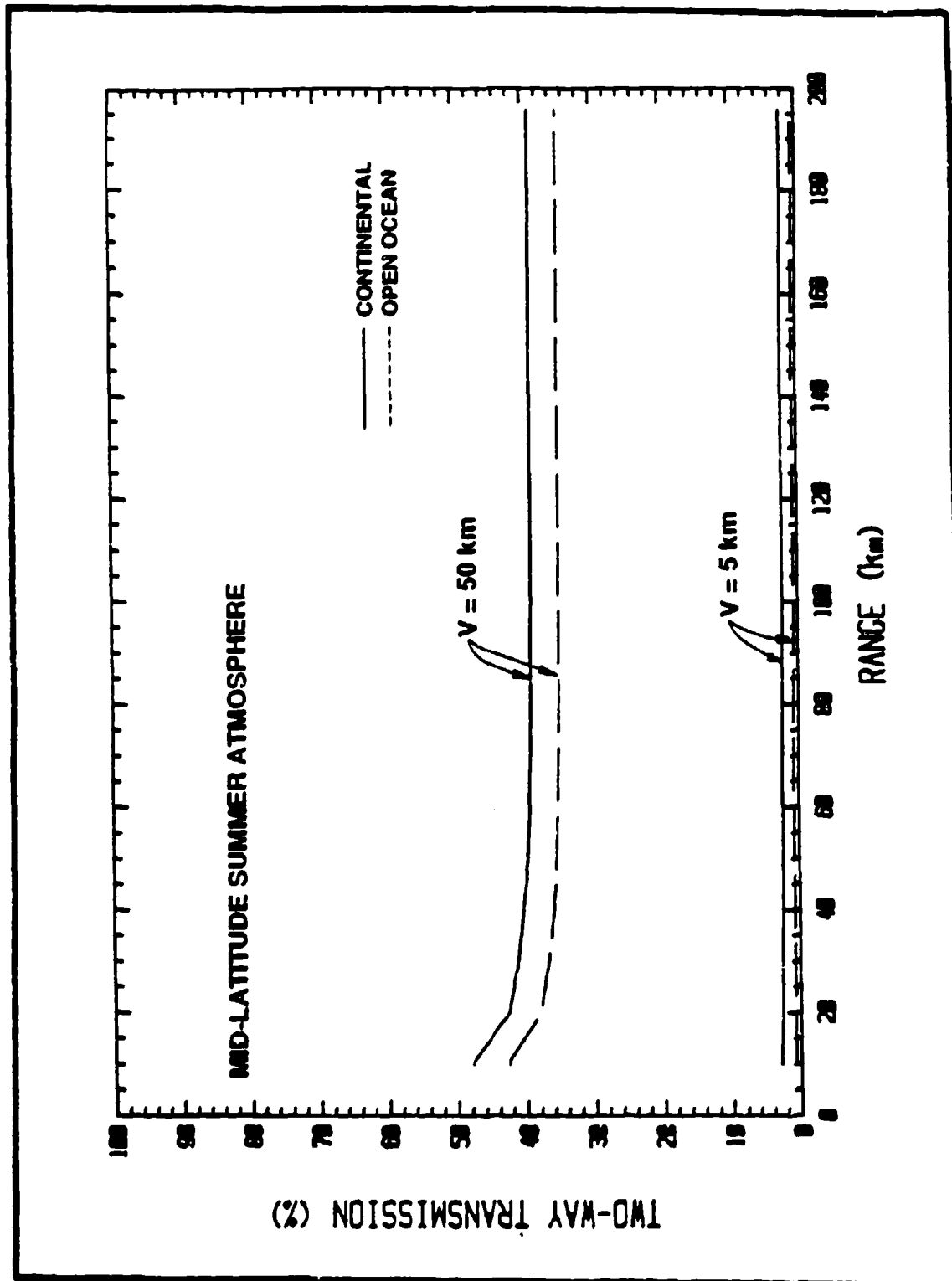


Fig. 2.5 Two-way atmospheric transmission at $0.7 \mu\text{m}$ calculated with LOWTRAN7 for Mid-Latitude Summer Atmosphere (30° elevation angle).

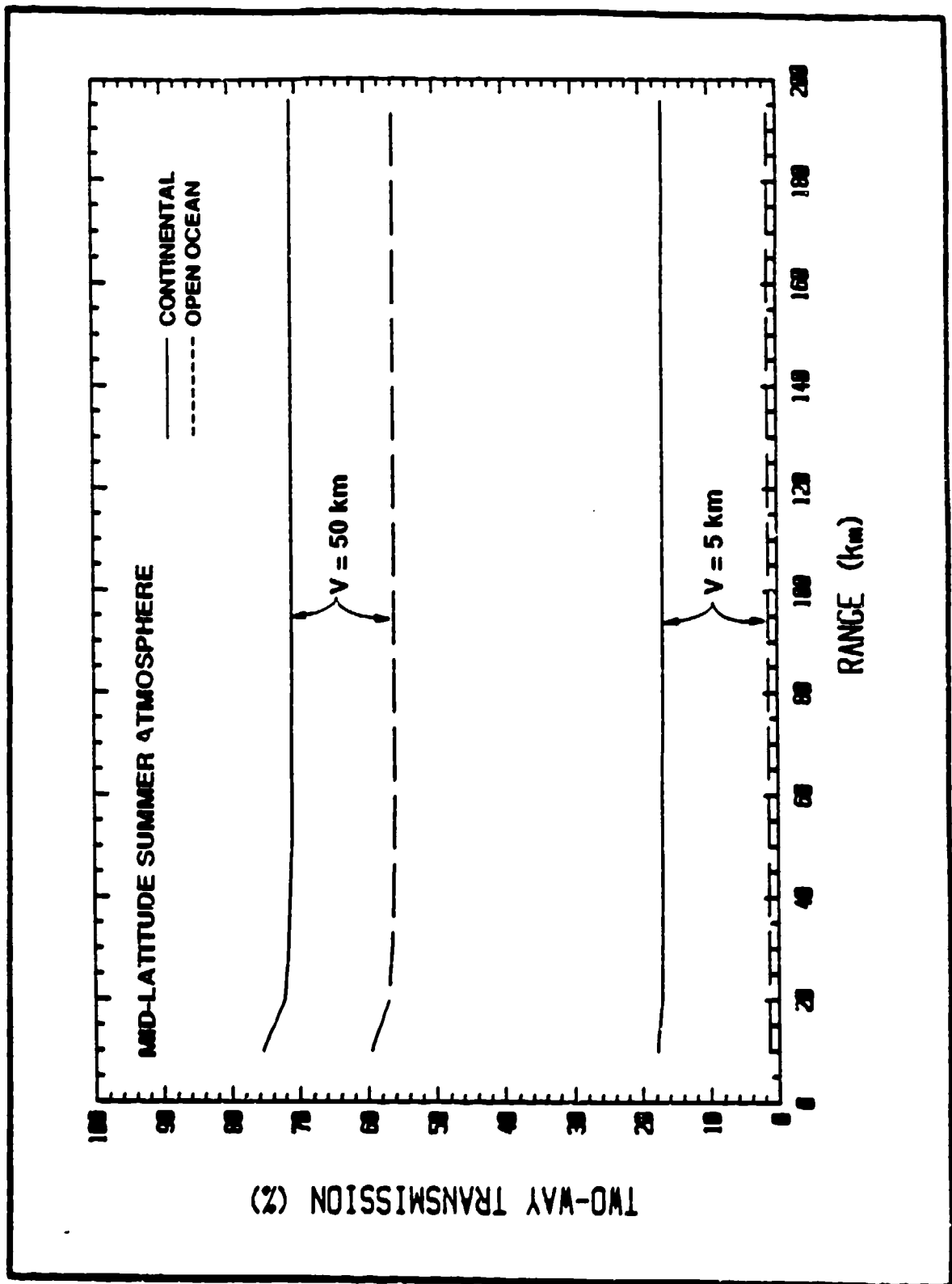


Fig. 2.6 Two-way atmospheric transmission at $1.06 \mu\text{m}$ calculated with LOWTRAN7 for Mid-Latitude Summer Atmosphere (30° elevation angle).

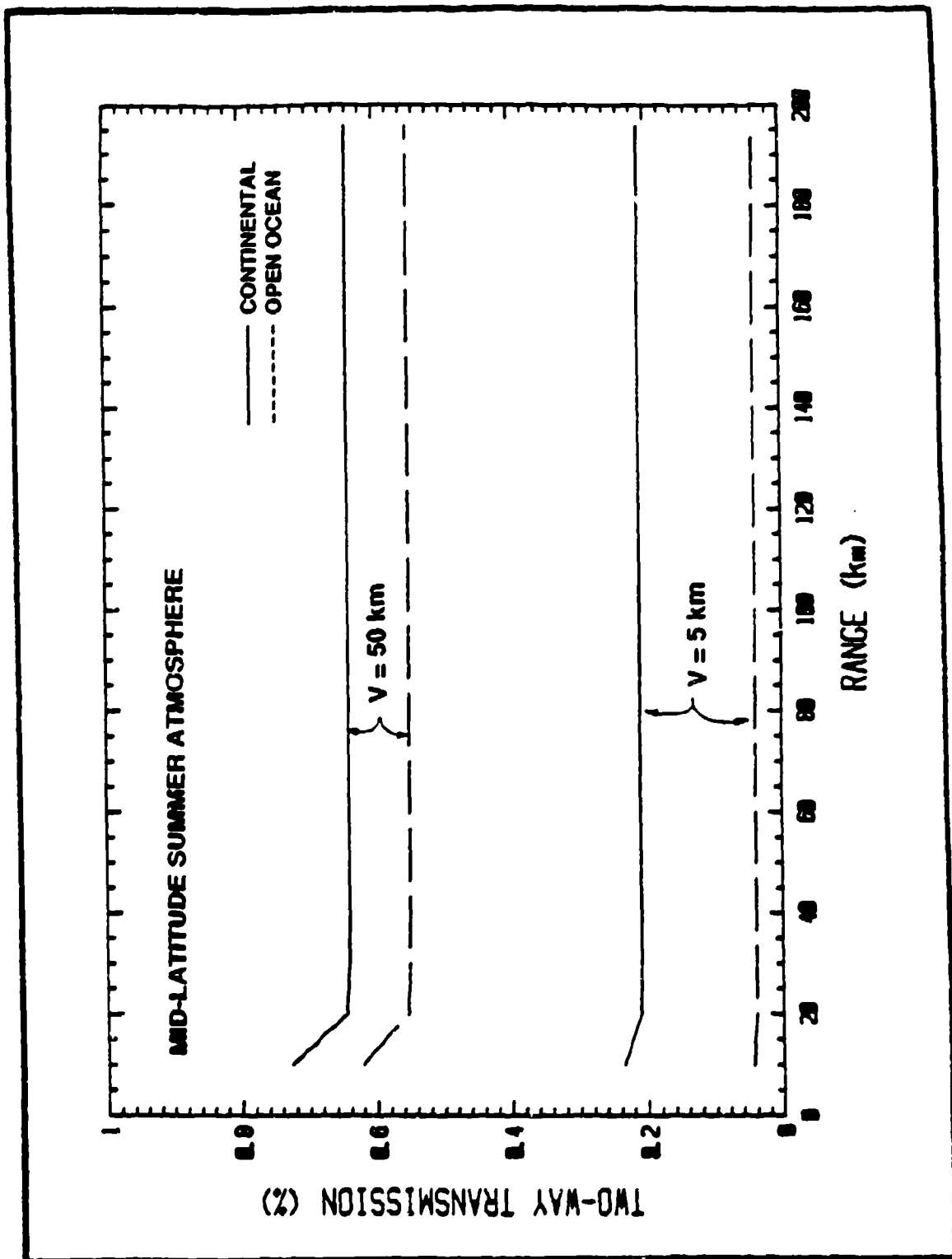


Fig. 2.7 Two-way atmospheric transmission at $3.0 \mu\text{m}$ calculated with LOWTRAN7 for Mid-Latitude Summer Atmosphere (30° elevation angle). Note that the vertical scale is from 0 to 1%.

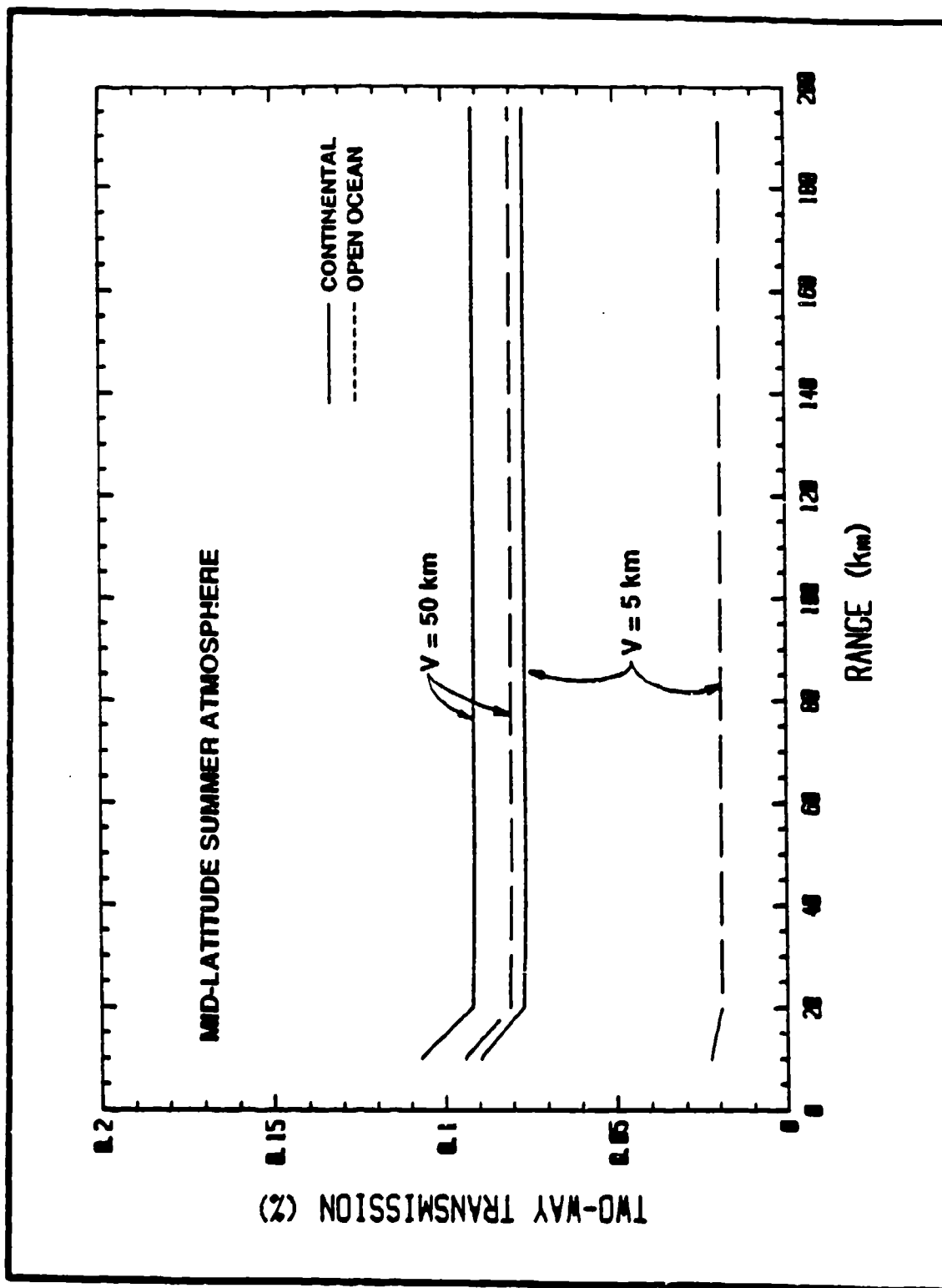


Fig. 2.8 Two-way atmospheric transmission at $5.0 \mu\text{m}$ calculated with LOWTRAN7 for Mid-Latitude Summer Atmosphere (30° elevation angle). Note that the vertical scale is from 0 to 0.2%.

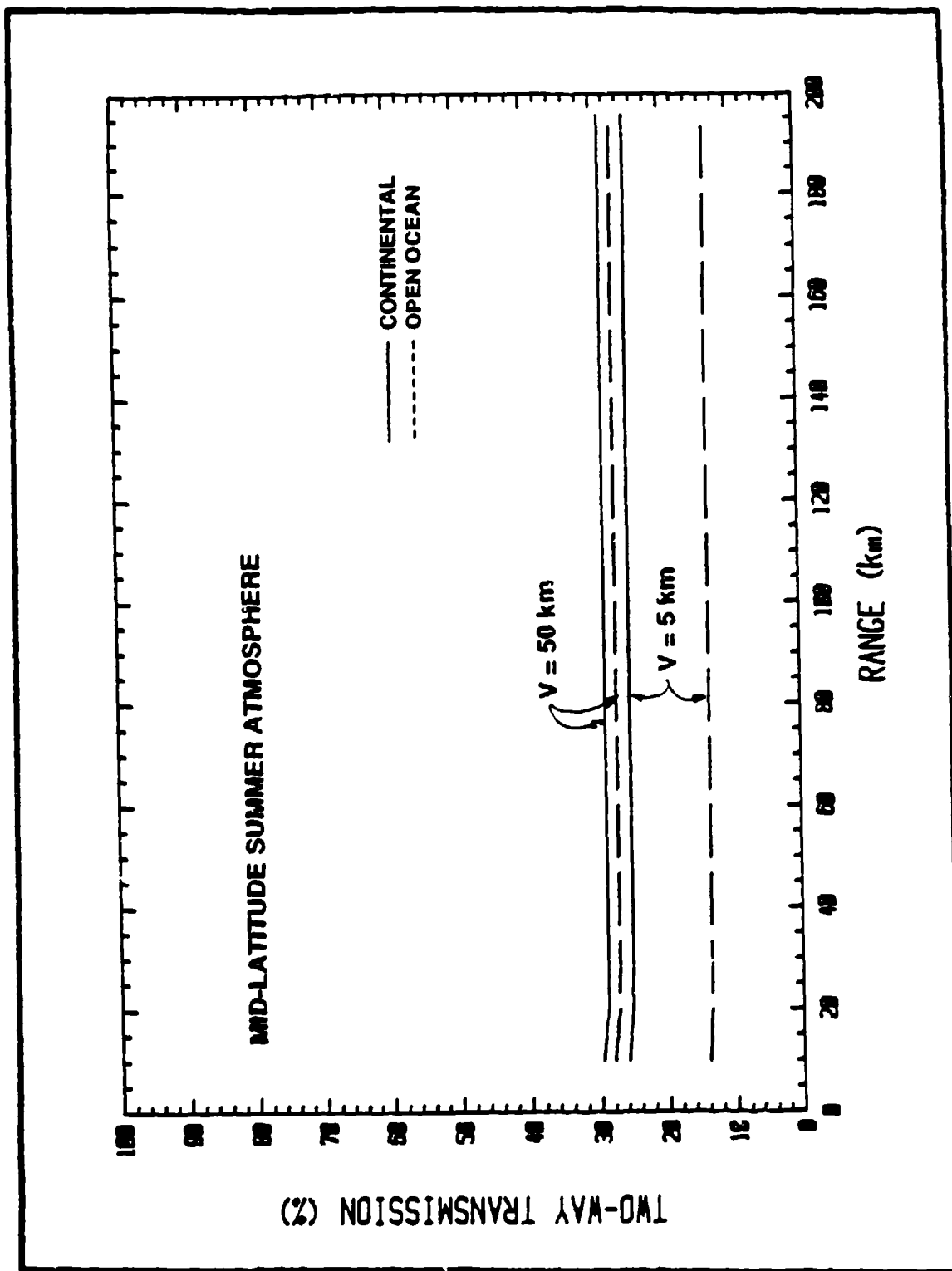


Fig. 2.9 Two-way atmospheric transmission at $10.6 \mu\text{m}$ calculated with LOWTRAN7 for Mid-Latitude Summer Atmosphere (30° elevation angle).

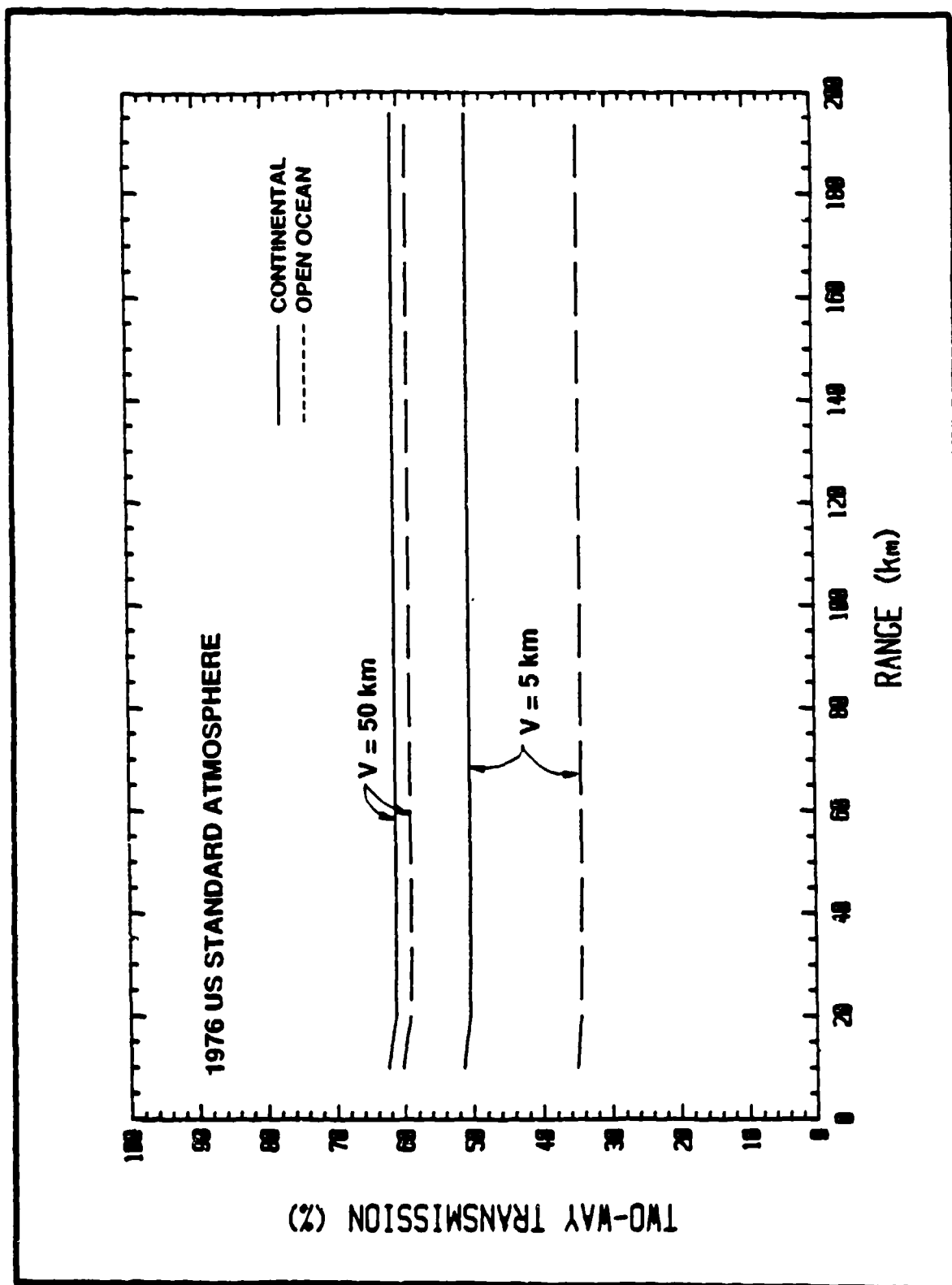


Fig. 2.10 Two-way atmospheric transmission at $10.6 \mu\text{m}$ calculated with LOWTRAN7 for 1976 U.S. Standard Atmosphere (30° elevation angle).

The results are shown in Figs. 2.11 and 2.12 for wavelengths of 0.53 and 1.06 μm , respectively. In these figures, the energy fraction is given as a function of altitude rather than range, which depends on the zenith angle θ . The weak signal from higher altitudes may require longer integration times, larger receiver apertures, and/or more powerful laser transmitter.

2.4 Conclusions and Recommendations

Collection of quantitative data on signatures of space objects requires real-time measurements of atmospheric transmission at the geographical site of interest. Review of the different techniques for transmission measurements led to the conclusion that either such measurements are difficult to implement in real time, or that they require untested assumptions about the nature of extinction, scattering, or multiple scattering. Therefore, we began the development of a novel real-time multipath lidar.

The main disadvantage of the multipath lidar is common to all remote sensing lidars; i. e., it relies on backscattering to provide the signal and may thus be limited by weak scattering at high altitudes. Therefore, averaging over several pulses may be required to improve the SNR.

On the other hand, the multipath lidar has many advantages. First of all it is very simple: except for the steering mechanism, it can be built with off-the-shelf hardware. Measurements can be made in real time. Simple data processing is needed to obtain the values of transmission coefficient as a function of range or extinction coefficient as a function of altitude and zenith angle without prior assumptions about scattering and extinction. Determination of the backscattering coefficient, however, requires absolute calibration of the system.

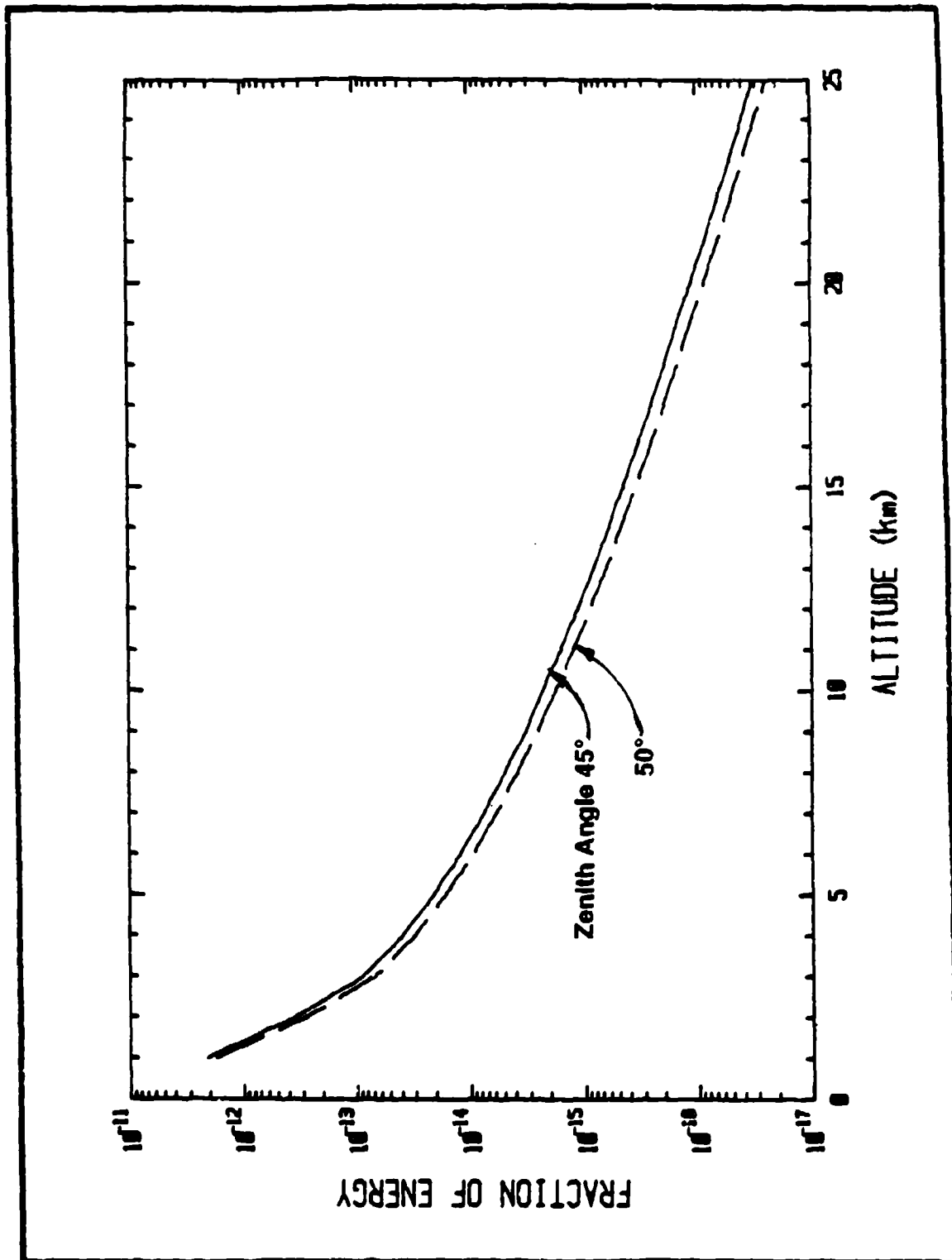


Fig. 2.11 Fraction of transmitted energy collected by the lidar receiver as a function of altitude for different zenith angles and $\lambda = 0.53 \mu\text{m}$.

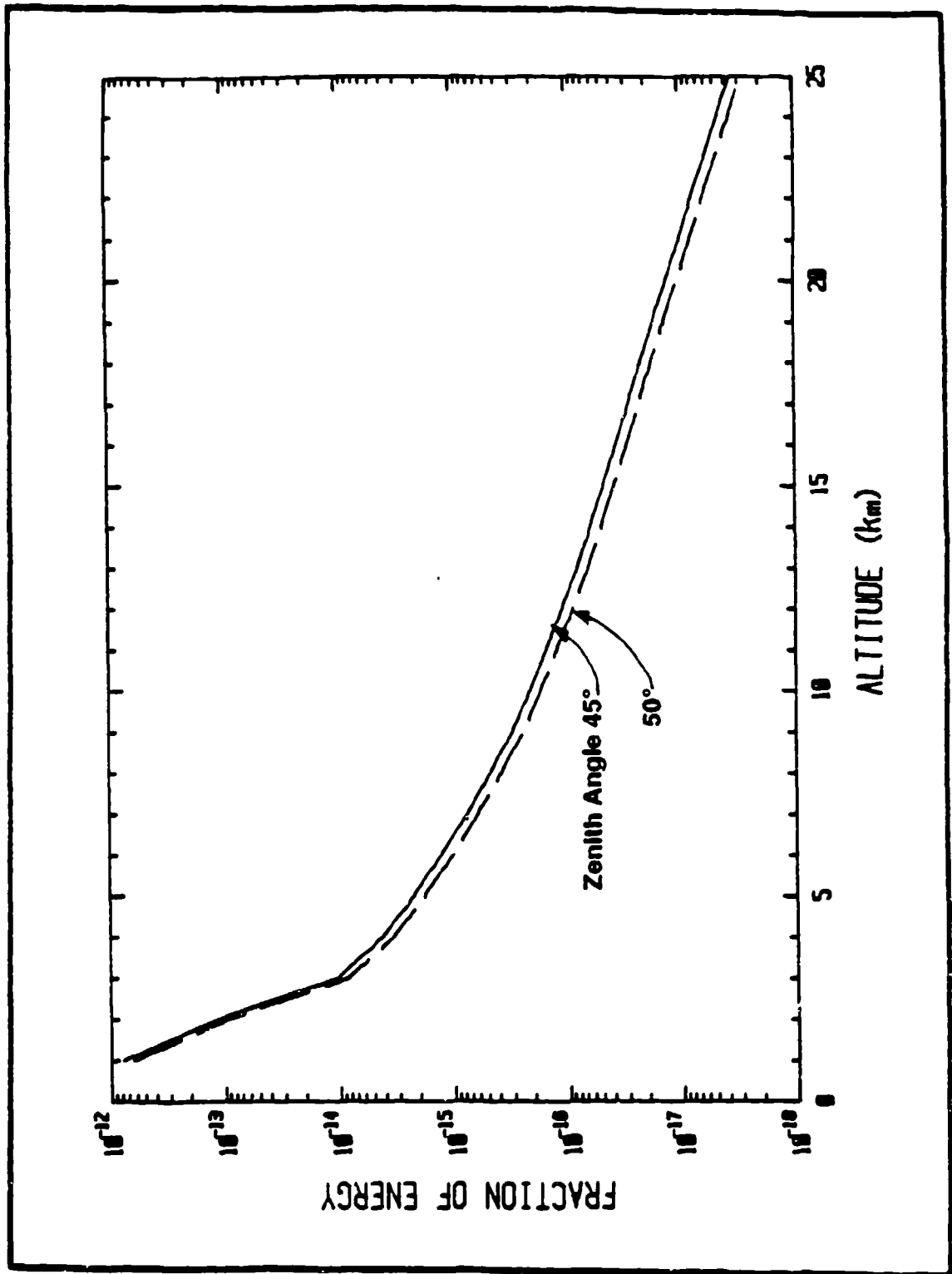


Fig. 2.12 Fraction of transmitted energy collected by the lidar receiver as a function of altitude for different zenith angles and $\lambda = 1.06 \mu\text{m}$.

RIVERSIDE RESEARCH INSTITUTE

The multipath lidar can be used to determine the characteristic length scales for horizontal inhomogeneities in scatterer properties as a function of altitude by varying the beam azimuth angle for a fixed zenith angle. Extinction and scattering by inhomogeneities of angular size greater than the angular separation between two beams could also be measured. Such inhomogeneities may include clouds and aircraft contrails.

If a dye laser is used in this lidar, the wavelength dependence of scattering and extinction coefficients could be determined. This is very important for measuring molecular absorption and, therefore, concentration of absorbing species, and also for determining the aerosol size distribution.

Several issues pertaining to the multipath lidar still have to be addressed. One of them, common to all lidars, is the effect of clear-air turbulence which may induce beam wander or spreading.¹²⁻¹⁴ Narrow (compared to the turbulence length scale) beams may wander, leading to uncertainties in the zenith angle, while wide beams may spread, leading to uncertainty in the geometric form factor for the lidar. The choice of the optimal beam width must be investigated. Averaging over pulses may be useful in separating the effect of clear-air turbulence and should also be analyzed.

The other issue is the possible alignment of nonspherical scatterers, e. g., ice particles in cirrus clouds. Possible advantages of polarization sensitive measurements should be investigated.

The proposed single-ended multipath lidar can be tested by using a transmissometer with an airborne receiver (or transmitter). Transmissometer measurements are very important not only for determining the overall accuracy of the proposed system but also for assessing its performance under different meteorological conditions.

2.5 References

1. W. C. Malm and E. G. Walther, "A Review of Instrument-Measuring Visibility-Related Variables", U.S. Environmental Protection Agency Report, Las Vegas, 1980.
2. R. M. Measures, "Laser Remote Sensing", Wiley, New York, 1984.
3. P. S. Bhardwaja, ed., "Visibility Protection: Research and Policy Aspects", APCA, Pittsburgh, 1987.
4. G. J. Kunz, "Bipath Method as a way to Measure the Spatial Backscatter and Extinction Coefficients with Lidar," Appl. Opt. 26 (5), 794 (1987).
5. H. G. Hughes and M. R. Paulson, "Double-Ended Lidar Technique for Aerosol Studies," Appl. Opt. 27 (11), 2273 (1988).
6. L. R. Bissonnette and D. L. Hutt, "Remote Sensing of the Aerosol Scattering Coefficients with a Multi-Field-of-View Lidar," to be published.
7. L. R. Bissonnette, "Multiscattering Model for Propagation of Narrow Light Beams in Aerosol Media," Appl. Opt. 27 (12), 2478 (1988).
8. A. D. Jursa, ed., "Handbook of Geophysics and the Space Environment", Air Force Geophysics Laboratory, 1985.
9. D. Gutkowitz-Krusin and Y. B. Fung, "On Radiation Scattering by Aerosols in the Earth Atmosphere", Research Note R-1/C56-7-10, Riverside Research Institute, New York, 1989.
10. J. D. Klett, "Stable Analytical Inversion Solution for Processing Lidar Returns," Appl. Opt. 20, 211 (1981).
11. C. F. Bohren and D. R. Huffman, "Absorption and Scattering of Light by Small Particles", Wiley, New York, 1983.
12. J. I. Davis, "Consideration of Atmospheric Turbulence in Laser Systems Design", Appl. Opt. 5, 139 (1966).
13. R. J. Cook, "Beam Wander in a Turbulent Medium: An Application of Ehrenfest's Theorem", J. Opt. Soc. Amer., 65, 942 (1975).
14. A. M. Whitman and M. J. Beran, "Beam Spread of Laser Light Propagating in a Random Medium", J. Opt. Soc. Amer., 60, 1595 (1970).

3.0 AUTODYNE DETECTION

RRI proposed to use the optical autodyne detection^{1,2} system to improve the performance of passive and conventional active sensors in detection, recognition and tracking. The proposed technique can be applied against ground and aerospace targets in a variety of scenarios as well as for booster and satellite imaging and tracking. The work presented here is a part of the continuing effort to develop an analytic framework for the detection and parameter estimation of autodyne signals, an analysis applicable in a variety of scenarios with targets such as rotating (or vibrating) satellites, or tracking hardbody-plume booster interface. This analysis will be useful in evaluating other techniques based on light intensity interferometry such as correlography, for diffuse and complex targets with strong specular components and will be extended to spatio-temporal light intensity interferometry where correlography and autodyning are limiting special cases.

When an incoherent laser illuminator is replaced by a coherent one, active images are degraded by laser speckle. It is possible, however, to obtain Doppler measurements providing information about the target radial velocity and possibly its vibration. This signature permits the detection of moving or vibrating targets in the presence of fixed or static targets, even when the signature from the fixed target is of magnitude greater.

One can employ heterodyne reception in the image plane when the detector array is illuminated by a local oscillator laser and outputs are properly processed. This provides velocity information in each resolution cell of the active imaging sensor and reduces the contribution from background (clutter) and detector noise. Measurement of the velocity distribution within the illuminating beam can also be obtained without resorting to the imaging system, by employing a single detector properly matched to the size of speckle produced by reflections of the illuminating beam and using heterodyne detection. The heterodyne detection technique requires very precise frequency matching of illuminator and local oscillator lasers and precise alignment of the signal and local oscillator beams. This may be quite difficult to achieve and maintain, especially for shorter wavelengths.

RRI proposed to replace the sophisticated and sensitive heterodyne method by a more robust autodyne technique. Optical autodyne detection is a direct detection method for measuring the relative Doppler frequency shifts using a coherent laser illuminator. Various frequency components of the received optical signal are mixed together on a square-law photodetector to produce an output containing the spectrum of frequencies related to the relative velocity spectrum of the target and background components. The main advantage of autodyne detection, as compared with the usual heterodyning techniques, is its simplicity; a local oscillator is not necessary. The increased robustness of an autodyne system makes it attractive for many applications. Such an active system may consist of a pulsed laser transmitter and a photon bucket receiver, although an array of autodyne detectors in the focal plane of the imaging sensor may also be employed. One deficiency of autodyne detection is that it provides information about autocorrelation of functions proportional to the reflectivity of elements moving with a given radial velocity, while heterodyne technique in principle can provide direct information about the reflectivity as a function of radial velocity. In many scenarios, however, a simple autodyne detector will provide a signature sufficiently complementing the information obtained by the passive - active sensor suite.

A limited experimental proof-of-principle laboratory demonstration has been already performed^{1,2}.

In the next funded program phase, it is recommended that RRI design more complete and realistic experiments illustrating the capabilities of the autodyne technique for pulsed lasers, and define hardware requirements for the autodyne system in various scenarios of interest. Different algorithms capable of extracting relevant information for complex targets, containing a mixture of diffuse and specular reflectivity components, could be proposed and sensitivity studies performed to evaluate the applicability of such systems to the ONR mission.

The program presented by RRI will lead to the development of a new class of autodyne sensors useful in various scenarios of practical interest. It will also help to establish

which additional measurements of target, and background signature, and what additional data related to sensor pattern selection are necessary to arrive at a realistic assessment of the feasibility of the proposed technique.

3.1 Background, Technical Approach, and Anticipated Benefits

3.1.1 Background

In many applications, an improved performance of optical passive and active sensors against ground, airspace and space targets is required. This enhancement can be achieved by the addition of a coherent laser illuminator. If an active imaging receiver is employed, speckled images of the target can be obtained, and with appropriate wavefront modulation one obtains range information. Employment of the autodyne array for an active imager will provide information about the relative velocity distribution in a resolution cell of the active imager. A photon bucket receiver with autodyne detector will provide information about the relative velocity distribution in the illuminated region. An array of properly distributed photon bucket receivers will not only improve the appropriately defined signal-to-noise ratio, but may give some information about the spatial distribution of the target and background components and their velocities (imaging and Doppler measurement with spatio-temporal intensity interferometry). While coherent (heterodyne) detection can provide unambiguous information about absolute velocity distribution, the autodyne mode of detection can offer a practical scheme of sufficiently robust and inexpensive sensor for many applications.

A meaningful evaluation of an active system requires a good understanding of the role it has to fulfill in various missions and scenarios. It could vary from detection of a moving target within a set of possible targets selected by passive sensors in a cluttered background to the determination of the type of target from vibration spectrum or the detection and tracking of a selected feature in a complex target. The capability of providing rapid illuminator beam steering may be required; weather constraints may be an important factor to be considered. Important elements defining optical system performance include illuminator

power, beam wavefront quality, pulse repetition rate, constraints and effects of the selection of illuminator and receiver platform, the properties of bidirectional propagation channel, target and background effects, detector characteristics, resolution and sensitivity of spectrum analyzers or digitizers. RRI is aware of these effects and has the capability to bound and quantify their contribution to the overall system performance. Understanding these issues and their impact on the performance of heterodyne and autodyne systems, together with the knowledge of the state of the art is essential to assess the potential and the deficiencies of these two techniques.

3.1.2 Technical Approach

Let us assume that both receiver and transmitter are located on the ground. The performance of a highly coherent laser transmitter illuminating the target with known intensity distribution may be affected by platform vibration and optical path phase and amplitude distortions. Platform vibrations are important for a sufficiently narrow beam, when the induced beam jitter becomes comparable with the beam size. Part of the optical degradation is due to the index of refraction fluctuations caused by clear weather turbulence³ of the atmosphere. The size of these fluctuations depends on weather conditions, transmitter and receiver location, transmitter line of sight (LOS), and for fixed aperture size their contribution increases as the wavelength becomes shorter.

The presence of the turbulence effects may produce additional beam jitter or more serious degradation of illuminating beam for larger apertures or ranges.

It is useful to divide the effects of turbulent atmosphere into two parts corresponding to segments of a bidirectional earth - space - earth propagation channel. The highly coherent earth based laser transmitter illuminates target in space with a beam of optically flat distribution or other known intensity distribution (uplink). Diffuse and specular reflection of the laser illuminator is detected by the ground based receiver (downlink).

RIVERSIDE RESEARCH INSTITUTE

A rudimentary analysis reveals that turbulence - induced beam spreading will increase the diffraction limited far field beamwidth of the laser transmitter, and angle-of-arrival fluctuations may limit the power collection capability of the diffraction limited receiver (if it is sufficiently large). While atmospheric beam spreading may degrade system performance operating in low light conditions (e.g., at large ranges), both in correlography in autodyne detection (with nonimaging receiver), the use of diffraction limited receivers is not required and atmospheric limitations on the size of PSF are not especially significant for a receiver that is essentially an aperture integrator (photon bucket). Both uplink transmission and downlink reception are subject to scintillation fading, and those effects may significantly affect the performance of various techniques employing analysis of spatio-temporal behaviour of speckle patterns to obtain the desired target characteristic. In general, both uplink and downlink effects will be present simultaneously. It is instructive, however, to consider degradations produced in a simplified case when only one of these two effects is present. In particular, compensating optics can be used to combat uplink fading, while on the downlink this can be accomplished by spatial averaging of atmospheric speckle with sufficiently large receivers (if target generated speckle is sufficiently large), or by increasing the number of receivers.

If we assume that the target is far above the atmosphere, then all turbulence in the propagation path is located near the receiver and transmitter plane. Because of this concentration of turbulence near receiver and transmitter, the earth-space channel behaves as though the vacuum channel was dominating through most of the propagation path from transmitter (receiver) to target, with turbulence creating a random phase and amplitude screen in the transmitter (receiver) plane. This simple modeling which neglects the thickness of atmospheric layer may occasionally, depending on applications, be inadequate or even lead to contradictions. Defining the conditions when simple modeling of the propagation channel with one of a few properly positioned random screens is adequate for a given application would greatly contribute to better understanding of the requirements for the different techniques of spatio-temporal speckle processing to provide satisfactory estimates of target parameters.

It can be easily shown that downlink effects are equivalent to multiplicative random modulation intensity distributions of target generated speckle patterns in the receiver plane (provided that the target is smaller than the isoplanatic patch size). Similarly, uplink effects are equivalent to random modulation of illuminator beam wavefront which multiplies target reflectivity amplitude. The result of uplink and downlink turbulence effects can be presented as generating different type of bias of the estimates of various target characteristics.

It is worth noting that the resolution of passive and active sensors will be similarly affected by turbulence. If the angle-of-arrival fluctuations cause a degradation of active images, this will affect the autodyne as well as the heterodyne detection techniques. If a non-imaging receiver that is essentially an aperture integrator (photon bucket) is employed, this atmospheric degradation is not important for the autodyne technique, but it may degrade the efficiency of heterodyne detection if the correlation scale of the angle-of-arrival fluctuations is comparable to the detector size. If non-imaging arrays of detectors are employed, the presence of the channel induced degradation further diminish the attractiveness of heterodyne schemes. Since both parts of the propagation channel are subject to scintillation fading effects, they may influence the performance of autodyne as well as heterodyne detection schemes. In some scenarios, non-imaging arrays of autodyne detectors could produce outputs which, when properly processed, would allow resolution exceeding the limitations imposed by the turbulence effects on imaging sensors.

All this indicates that the presence of atmospheric turbulence induced degradation either worsens both systems in a similar fashion or makes the autodyne scheme more attractive. Other changes in the signal, due to absorption by atmospheric gases or scattering by molecules or aerosols which could be of great importance in some scenarios, will affect both techniques in a similar fashion and could be the decisive factors in wavelength selection.

The laser radar signatures of the different targets and their proper characterization in various operational scenarios is an important element of performance evaluation of an active

sensor. Many targets of interest represent geometrically complex objects. For instance, some satellites should be modeled by several flat and curved surfaces and edges. This may result in rather complicated signatures, strongly dependent on the relative configuration of the transmitter, receiver, and target. The relative contribution to the observed signatures of the specular component of the target reflectance due to edges and flat surfaces normal to the transceiver vs the diffuse component of the target reflectance, their stability and classification potential will affect the choice and mode of operation of an active sensor.

Let us assume that the target is illuminated with a beam which is larger than the target dimensions, and that longitudinal coherence of the transmitted illumination pulse is determined by the finite duration of the pulse. We may be interested in target vibration spectrum where the target may represent a helicopter in the vicinity of clouds.

Let us assume that A_B is an effective illuminator beam area in the target plane. Then a properly matched receiver at distance R should have the dimensions

$$A_R = \left(\lambda^2 / A_B \right) R^2. \quad (3.1)$$

The number of photons/sec incident on the receiver is given by

$$N_{PR} = \left[\left(\epsilon_\rho / \pi \right) d\Omega \right] N_{PT} \quad (3.2)$$

where \hat{N}_{PT} is the number of photons/sec transmitted, λ is laser wavelength, and $d\Omega$ is the solid angle given by A_R/R^2 . We also assumed that the illuminated spot can be described by a Lambertian scatterer with effective reflectivity ϵ_ρ . Therefore,

$$\begin{aligned} N_{PR} &= \left[\left(\epsilon_\rho / \pi \right) \left(\lambda^2 / A_B \right) \right] N_{PT} \\ &= \left(5 \cdot 10^{24} \right) \left(\epsilon_\rho / \pi \right) \left(\lambda^3 / A_B \right) P_T \cdot \left(1 / \text{watt} \cdot \text{meter} \cdot \text{sec} \right) \end{aligned} \quad (3.3)$$

where P_T is the power in watts.

RIVERSIDE RESEARCH INSTITUTE

The Doppler shift of backscattered radiation is given by:

$$\Delta\nu = \left(2v/c\right)v_0 = 2v_r/\lambda \quad (3.4)$$

where ν_0 is the light frequency, and v_r is the radial velocity of the scatterer. The smallest temporal scale is related to the largest relative velocity $\Delta\nu_{rmax}$ present among scatterers (the so-called temporal size of speckle), and is given by

$$T_{sp} = 1/\Delta\nu_{rmax} = \lambda/2\Delta\nu_{rmax}. \quad (3.5)$$

This important parameter defines the required detector response. The number of photons registered in this characteristic time is given by

$$N = \left(\epsilon/\rho\right) \left(\lambda^4/\lambda_B\right) \left(P_T/\Delta\nu_{rmax}\right) \left(5 \cdot 10^{24}\right) \left(1/\text{watt} \cdot \text{meter}\right) \quad (3.6)$$

In order to achieve autodyne detection which is not shot noise limited (and assuming that detectors are shot noise limited), a minimum N of 5 + 10 photons are required per temporal speckle⁵; therefore, to operate in this regime, the expression for the power requirement is given by:

$$P_T [W] = \frac{2\pi}{\epsilon/\rho} \cdot \frac{N\lambda_B\Delta\nu_{rmax}}{\lambda^4 \left[5 \cdot 10^{24}\right] \left[\eta_{TOT}\right]} \quad [\text{meter}] \quad (3.7)$$

where η_{TOT} describes the total transmitter and receiver efficiency, and includes possible atmospheric losses.

The amount of energy per pulse is determined by the velocity resolution requirement and defined by pulse duration. This second characteristic time scale is given by

$$T_p = \lambda/\Delta\nu_{rmin}. \quad (3.8)$$

and leads to the following energy requirement:

RIVERSIDE RESEARCH INSTITUTE

$$E[J] = \frac{2\pi}{\epsilon_{\rho}} \cdot \frac{N \lambda_B \Delta v_{rmax}}{\lambda^3 \Delta v_{rmin} \eta_{TOT} [5 \cdot 10^{24}]} \quad [\text{meter}] \quad (3.9)$$

This amount of energy (for N of the order of 5 + 10) would allow for "semiclassical" operation. Note that in addition to the expected dependence on illuminated area, receiver and transmitter efficiency, it is proportional to the inverse of the cube of the wavelength and the number of velocity resolution cells defined by

$$N_{res} = \left(\Delta v_{rmax} / \Delta v_{rmin} \right). \quad (3.10)$$

Increasing laser energy beyond that required for semiclassical operation will not bring about any significant improvement (for shot noise limited detectors) and fixed pulse deviation. In semiclassical operation, after proper signal processing, we can obtain autocorrelation of reflected intensity distribution as a function of radial velocity. Each "resolution" cell in this image will be corrupted by noise. Typically, SNR defined as signal divided by the square root of variance of the signal can be of the order of 1/2 (results depend on the signal processing scheme and on target signatures).

Consider the following numerical example:

$$\begin{aligned} \epsilon_{\rho} &= 0.1, \quad \eta_{TOT} = 0.05, \quad \lambda_B = 100 \text{ m}^2, \quad \lambda = 10^{-6} \text{ m} \\ N &= 10, \quad \left(\Delta v_{rmax} / \Delta v_{rmin} \right) = 100. \end{aligned} \quad (3.11)$$

This leads to $E_T = 25J$. In the visible range, for $\lambda = .5 \cdot 10^{-6} \text{ m}$, $E_T = 200J$ and for long wavelength $\lambda = 10 \cdot 10^{-6} \text{ m}$, $E_T = (1/40)J$. This rather considerable energy requirement for short wavelength cannot in general be easily decreased by any significant amount without paying a price somewhere else. For instance, a decrease of the energy by a factor of two can be compensated to produce the same SNR by using two autodyne detectors or two (so that the number of photons per temporal speckle N is reduced from 10 to 5) pulses; further decrease of the energy transmitted may require a disproportional increase of the number of autodyne receivers. For lowlight conditions, this number would be proportional to the square of the

inverse of transmitted energy. For longer wavelength the energy requirements as listed do not represent a significant constraint, but the formulas are too optimistic, since infrared detectors are not shot noise limited. One can, however, easily replace the formula presented above by interpolating the expression which takes into account the detector noise. Let us note that energy requirements for heterodyne reception are similar, except that detector noise is usually negligible.

When tracking booster-plume interface with a narrow beam with effective area of $4m^2$ we obtain much more moderate energy requirements in the visible range of $E_T = 8J$.

It is worthwhile to compare the energy requirement of non-imaging autodyne detection and that of an imaging sensor (in non-autodyne mode, to assure a performance which is not shot noise limited). In this case the number of photons incident on the imaging receiver is given again by:

$$N_I = \left[\left(\epsilon_\rho / \pi \right) d\Omega \right] N_T = \left[\left(\epsilon_\rho / \pi \right) \left(A_R / R^2 \right) \right] N_T \quad (3.12)$$

where A_R is the area of imaging receiver and N_T is the number of photons transmitted. Since the area of resolution cell in the target plane is given by $(\lambda^2/A_R)R^2$, the number of photons from the resolution cell of the illuminated spot is given by

$$\begin{aligned} N_{IR} &= \left[\left(\epsilon_\rho / \pi \right) \left(\lambda^2 / A_B \right) \right] N_T \\ &= \left[5 \cdot 10^{24} \right] \left(\epsilon_\rho / \pi \right) \left(\lambda^3 / A_B \right) \hat{N}_T \left[1/\text{Joule} \cdot \text{meter} \right] \end{aligned} \quad (3.13)$$

where \hat{N}_T is pulse energy in Joules. In order to achieve an image quality which is not shot noise limited (and assuming coherent illumination and shot noise limited detectors), we need an N_{IR} of the order of 5 per resolution cell. Therefore, to operate in this regime, we obtain the following energy/pulse requirement:

$$E[J] = \left(\pi / \epsilon_\rho \right) \frac{N_{IR} A_B}{\lambda^3 \eta_{TOT} \left[5 \cdot 10^{24} \right]} \text{ [meter]} \quad (3.14)$$

RIVERSIDE RESEARCH INSTITUTE

and η_{TOT} again describes the transmitter and receiver efficiency together with atmospheric channel losses.

This expression is similar to the one obtained for autodyning, except that it does not involve a multiplier equal to the number of velocity resolution cells. Note that a factor of two is also missing and our estimate of N_{IR} necessary to attain the classical regime can also be lower by a factor of two, one has to be careful, however, with such order-of-magnitude estimates.

Thus, accepting the numbers from the previous numerical example, we have an energy requirement which is more than a hundred times lower than in autodyning. In addition, for the imaging sensor we can trade directly the laser energy/pulse for the number of pulses or the number of receivers, which, as mentioned above, is possible only for a limited energy range in autodyning. Another condition necessary for achieving a performance which is not shot noise limited is the requirement for the minimum power. Decreasing laser power and increasing the pulse duration with fixed energy increases the resolution of the autodyne technique. For an imaging system and low light level conditions, the resolution can be traded directly for SNR. Similar direct tradeoffs for autodyning are possible only for a limited range of power, without causing SNR degradation. If, however, energy beyond that required for semiclassical operation is available, increasing pulse duration is often beneficial. The energy requirement for an autodyne array of an imaging system is similar to that of a nonimaging system. It is important to note that employment of an imaging sensor with too high resolution may rule out the appearance of an autodyne signal if the target signal components with different velocities are separated into different resolution cells.

This general discussion needs refinement and should be more strongly connected to various scenarios and detected target signatures. For instance, when the velocity spectrum contains only two points as in the case of aircraft moving in a clouded background, detection and estimation of the signal may require lower laser power than in the case of the general velocity distribution. This should be included in the discussion of the value of a priori

knowledge in estimating the parameters of interest. A major section of this report is devoted to this problem. Another important case corresponds to the target with specular reflection. In some cases glint reflection would serve as a local oscillator for the reflected diffuse component and effectively convert the autodyne system into heterodyne detection⁶. Improvement of SNR by the employment of several autodyne detectors was mentioned above in the context of shot-noise reduction. In many cases using sparse arrays of autodyne detectors would lead to noise reduction due to fading. To introduce proper spatio-temporal sampling redundancy, helpful in improvement of SNR (if possible), it is necessary to have a good understanding of target signatures, and in particular the target coherence properties.

Another problem not discussed here is the use of proper wavefront modulation to enhance the range estimation, and also to obtain information about the target depth. While range information can be easily extracted for relatively short pulses, with simple amplitude modulation more information about the target in the line of sight direction can be obtained using autodyne detection by appropriate phase modulation similar to the one employed with conventional radar. We will briefly touch upon this problem in the next section.

3.1.3 Anticipated Benefits

The discussion of issues outlined above could be carried out in more detail for various scenarios of interest in the future to establish when the autodyne system can enhance the performance of a passive and conventional active sensor suite. The development of an analytical framework would help to understand the potential of the autodyne system. This would also help to assess the usefulness of the autodyne photon bucket detector array in obtaining both target images⁴⁻⁹ and velocity information for various scenarios. Such an analysis will help to select proper sensor architecture (imaging or nonimaging) for limited demonstration and short- and long-term applications. The results obtained would be useful to guide technology development in the area of lasers, spectrum analyzers and digitizers.

3.2 Fundamental Limits on Range and Velocity Resolution for Autodyne Detection of Two Point Target

In this section we will consider limits on range and velocity resolution for autodyne detection of a two point target with a pulsed laser radar consisting of a transmitter collocated with a photon bucket receiver. In this type of system the target is illuminated with a beam which is typically larger than the target dimension and the received signal is registered by a square-law photodetector. The longitudinal coherence of the transmitted illumination pulse is determined by the finite duration of the pulse. In our analysis we assumed that the amplitude of the transmitted pulse is Gaussian. The considered model includes linear modulation of the phase of the transmitted pulse.

We will discuss the estimation of ranges, relative velocity, and amplitudes of a two point target when laser backscattered radiation is collected with a photon bucket receiver of proper dimensions and registered by an incoherent autodyne detector. An analytical framework is developed to establish the fundamental limits on the resolution of such a system to obtain a quantitative understanding of the dependence of the accuracy of estimation on target separations, amplitudes, relative velocities, and on the number of photons available. The value of a priori knowledge to obtain a desired accuracy for estimation of a parameter of interest is computed and discussed for selected cases. The analysis is carried for Poisson photon statistics. The performance of various estimators is evaluated by utilizing the Cramér-Rao bound^{10,11} (CRB) for both shot noise and background limited conditions. The results presented have applications for robust laser radars and contribute to a better understanding of the performance and potential of an autodyne detection system.

There are several special cases corresponding to interesting problems. When the relative velocity of two points is known and equal to zero then we have to determine longitudinal separation of two fixed points, i.e., time delay between echo signals registered by the detector. This problem is a one dimensional temporal analogue of the estimation of a spatial separation of two point sources from their image^{12,13}. Another problem corresponds to the case when separation between two points is zero and when Doppler shift gives

information about relative velocity of the target component. This can be the case for instance in some geometries when the nozzle and reflection plume are illuminated by a laser pulse. The case when reflectivity of one of the point targets is known and much higher than another brings autodyne detection into analogy with heterodyne detection.

Analysis presented in this paper will remain valid if the assumptions that a target consists of two points are relaxed. Indeed, two targets illuminated by a relatively narrow laser beam can have finite dimensions in the directions perpendicular to the line of sight (LOS) of illumination beam (provided that they do not rotate). The longitudinal dimensions of the target, however, should be sufficiently small so that the echo signal produced by the individual target component, pulse spreading or distortion of phase modulation are negligible. Transverse dimensions of a two component target will affect performance of an autodyne detector through limitations imposed on the size of the photon bucket. Indeed, since the photon-bucket area should not exceed $(\lambda^2/A_{TR})R^2$ where λ - wavelength, R - range and A_{TR} - transverse area of illuminated target assuming that all separations are much smaller than R) the transverse target dimensions limit the power collection capability of individual photon-buckets.

One of the important problems addressed is how the estimation accuracy of a subset of parameters depends on the knowledge (and the numerical value) of the remaining parameters. Indeed, it is important to recognize that the longitudinal resolution of two point targets (their separation and relative velocity) depends not only on the temporal pulse distribution, total signal and background noise level but equally important, on the state of our knowledge about the object prior to measurement.

Our goal is to determine theoretical limits on the accuracy of estimating the values of a set of parameters describing the echo signals from a two point source. Analysis of the accuracy with which one can measure separations, individual positions and relative velocity can be extended to other parameters or their combinations. A way to determine the number

of signal photons necessary to measure echo signal parameters with desired accuracy is indicated. We assume that the echo signal representing backscattering from two point targets and which may be embedded in a uniform background is registered by an incoherent (square-law) detector. Calculations are performed in the limiting case of ideal detectors with negligibly small (compared to the fine structure of the backscatter signal) response time, detecting the entire echo signal. The analysis is carried out for Poisson photon statistics. The Cramer-Rao bounds (CRB) for various parameters describing echo signal are computed and the sensitivity of the CRB to different parameters and changes in the number of unknown parameters is examined. The results presented here provide a more comprehensive definition of resolution of longitudinal separation and relative velocity for autodyne signals and are important in such applications as: astronomy, light communications and reconstruction of images from the recorded spatio-temporal evolution of speckle patterns.

3.2.1 Statistics and Parametrization of Echo Signals

Let $P(t, \underline{A})$ be the power distribution on the detector as a function of time, where $\underline{A} = (A_1, \dots, A_n)$ denotes a set of deterministic parameters describing the echo signal. The normalization of $P(t, \underline{A})$ is such that the probability of n_k photocounts in the k -th time slot on a detector with integration time τ is given by:

$$p(n_k | \underline{A}) = \frac{1}{n_k!} \left[E_k(\underline{A}) \right]^{n_k} e^{-E_k(\underline{A})}, \quad (3.15)$$

where:

$$E_k(\underline{A}) = \int_{(\tau)_k} dt P(t, \underline{A}) + \rho\tau = N_k(\underline{A}) + N_B, \quad (3.16)$$

P denotes the signal and ρ -uniform background power. In our analysis we assume that the backscattered signal is embedded in Poisson background noise and is continuously sampled through the entire echo signal. We assume the detector response time much smaller than integration time of the detector and small enough so we can write

RIVERSIDE RESEARCH INSTITUTE

$$E_k(\underline{A}) = \tau [P(t_k, \underline{A}) + \rho] = N_k(\underline{A}) + N_B \quad (3.17)$$

where t_k denotes sampling time of the detector. The joint probability distribution of collected photocounts is given by

$$P(\underline{n} | \underline{A}) = \prod_{k=1}^1 P(n_k | \underline{A}) \quad (3.18)$$

where \underline{n} is a vector representing the photocounts registered during observation time.

Let the time dependent part of the complex amplitude of the illuminating pulse be described by $f(t)$:

$$f(t) = Z(t) e^{i t \omega_0 \gamma(t)} \quad (3.19)$$

where $Z(t)$, $\gamma(t)$ describe the amplitude and frequency modulation. We selected Gaussian amplitude and linear frequency modulation:

$$Z(t) = \left(2\pi\sigma^2 \right)^{-1/4} e^{-t^2/4\sigma^2} \quad (3.20)$$

$$\gamma(t) = (1 + at)$$

Assuming that Doppler shifts are due to the linear (and nonrelativistic) motion of two target components, the power intercepted by the receiver can be parameterized as follows;

$$P(t, \underline{A}) = N_{s1} Z^2(t - \tau_1) + N_{s2} Z^2(t - \tau_2)$$

$$+ 2\sqrt{N_{s1} N_{s2}} Z(t - \tau_1) Z(t - \tau_2) \cos[2\omega_0 a(\tau_1 - \tau_2)(t - (\tau_1 + \tau_2)/2)$$

$$+ \Delta\omega(t - (\tau_1 + \tau_2)/2) + \psi]$$

$$= N_s \left\{ p Z^2(t - \tau - \Delta\tau/2) + (1-p) Z^2(t - \tau + \Delta\tau/2) \right.$$

$$\left. + 2\sqrt{p(1-p)} Z(t - \tau - \Delta\tau/2) Z(t - \tau + \Delta\tau/2) \right.$$

$$\cos \left[\Delta\omega(t-\tau) + 2\omega_0 a\Delta\tau(t-\tau) + \Psi \right] \quad (3.21)$$

where the Doppler shift of carrier angular frequency is given by

$$\Delta\omega = \omega_0 (2\Delta v/c) = 2\pi \left(\frac{2\Delta v}{\lambda} \right) \quad (3.22)$$

with Δv representing the relative velocity of the two target components along the LOS; $N_{s1} = N_s p$ ($N_{s2} = N_s(1-p)$) represent the average number of photons backscattered from the first (second) target registered by the detector when another target is absent; τ_1 and τ_2 are round trip time delays and Ψ is the phase offset; p is related to the relative backscattered signal from the target components, τ is round trip time delay $\tau = (\tau_1 + \tau_2)/2$ of the transmitted pulse to the midpoint of the line segment connecting two points along the LOS, and $\Delta\tau = (\tau_1 - \tau_2)$ is differential time delay which we can call temporal separation of two point targets. In deriving this equation we neglected several terms which were of the order of v_i/c (v_i - velocities) as compared to those already present. Another term which was omitted in the argument of the $\cos(\cdot)$ function was of the form $a\Delta\omega(t-\tau)^2$; dropping this term is justified provided that $a\sigma \ll 1$ which we assume is satisfied. One may add that although the definition of pulse duration can vary depending on the application, its values typically are between 2σ and 4σ .

The set of parameters (A) describing backscattered signal registered by the detector consist of

$$\underline{\lambda} = [\tau, \Delta\tau, \Delta\omega, p, N_s, \Psi, \rho] = (\lambda_1, \lambda_2, \dots, \lambda_7) \quad (3.23)$$

and the total (average number of signal photons registered by detector) is given by

$$N_T = N_s \left\{ 1 + 2p\sqrt{p(1-p)} e^{\rho} \cos\Psi \right\}$$

$$s = - \frac{(\Delta\tau)^2}{8\sigma^2} - \frac{\sigma^2}{2} [\Delta\omega + 2\omega_0 a\Delta\tau]^2 \quad (3.24)$$

From this expression we can see that N_g is equal to the average number of photons only when $\psi = 0^\circ$ or 180° and approximate equality holds when separation between two point sources (along the LOS) or $\sigma^2[\Delta\omega + 2\omega_0\Delta\tau]^2$ is sufficiently large. Out of six parameters describing the pattern of echo signal, two (τ and N_g) define the pattern translation in time and scaling, respectively, and the remaining four define the pattern shapes.

In some calculations under shot noise limited conditions, one has to proceed with a special care if the echo pattern has zeros. Such zeros of pattern are present (excluding zeros for $t \rightarrow \pm\infty$), when pattern parameters satisfy the relation:

$$\psi + (\Delta\omega + 2\omega_0\Delta\tau) \left(\frac{\sigma^2}{\Delta\tau} \ln \left(\frac{P}{1-P} \right) \right) = (2k+1)\pi \quad (3.25)$$

where k is an arbitrary integer and $\Delta\tau \neq 0$.

Various cases of echo signal patterns are shown in Figs. 3.1, 3.2 and 3.3 for the special case of $p = 1/2$, when the backscatter signal from two target components is of equal strength and in the absence of phase modulation. In these and other figures, td , tdd and vd denoted time delay to the midpoint, temporal separation of two point targets, and relative angular Doppler shift measured in units of σ , i.e.; $td = \tau/\sigma$, $tdd = \Delta\tau/\sigma$, $vd = \Delta\omega\sigma$. The three special cases of received echo signals when phase $\psi = 0^\circ$ (solid line) $\psi = 90^\circ$ (dashed line) and $\psi = 180^\circ$ (dotted line) are shown in several figures and this convention is preserved throughout this work unless indicated otherwise.

In Fig. 3.1 we displayed the set of patterns obtained when relative LOS velocity of two points is zero, i.e., relative longitudinal position is fixed and temporal separation varies. This case is similar to the problem of spatial resolution¹³. In Fig. 3.1a the echo pattern for $\psi = 180^\circ$ corresponds to zero signal. Echo signal for $\psi = 0^\circ$ is twice the signal for $\psi = 90^\circ$. In Fig. 3.1b the pattern for $\psi = 180^\circ$ is barely discernible. In Fig. 3.1c and 3.1d the echo signals corresponding to three different relative phases are quite distinct. When temporal separation increases, echo signals become less sensitive to the value of phase, and in Fig. 3.1f

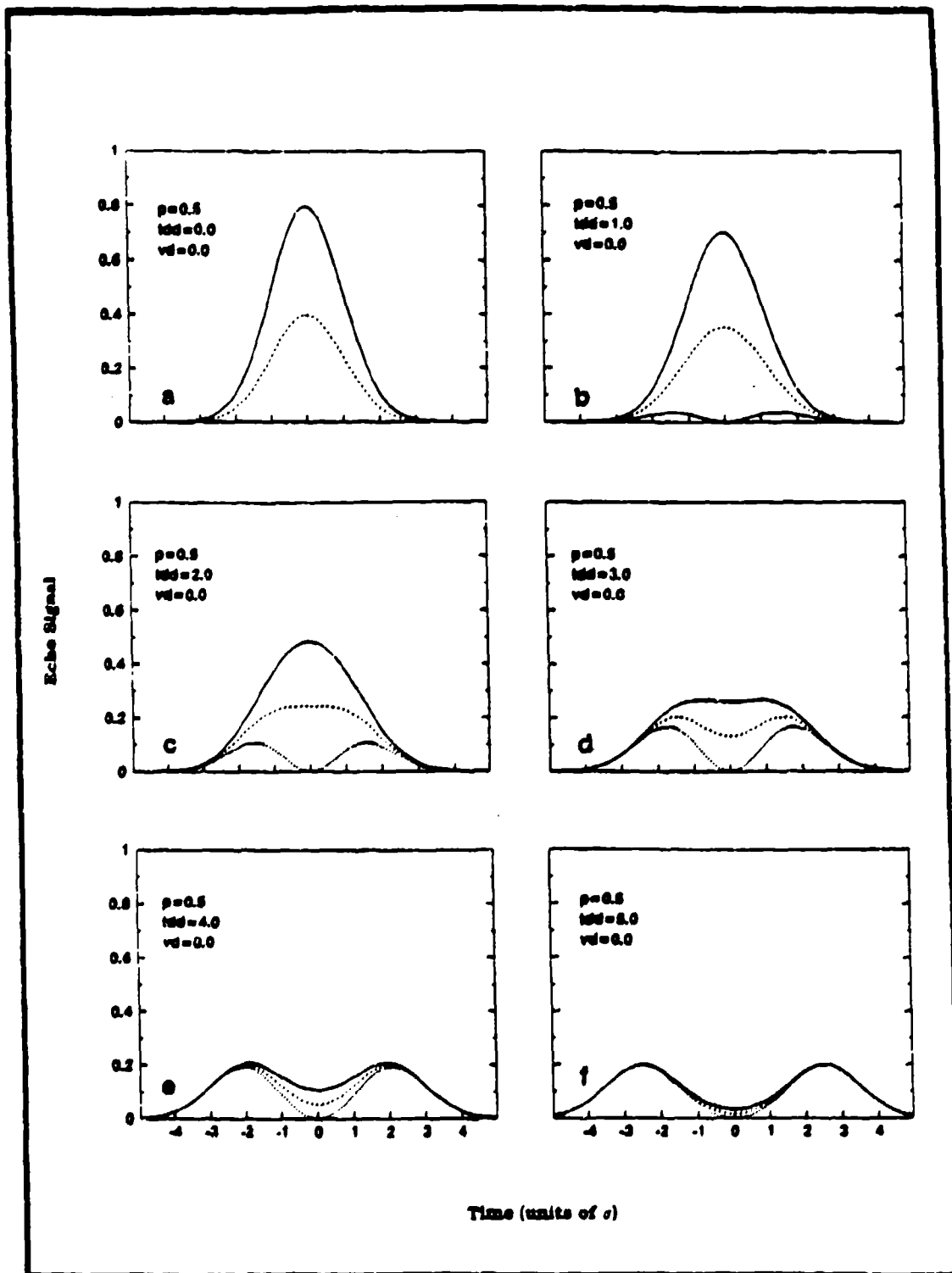


Fig. 3.1 Echo signal patterns from two equal strength, stationary backscatters, with changing values of separation. Solid line phase angle $\psi = 90^\circ$; dotted line - phase angle $\psi = 180^\circ$ for this and all subsequent figures (3.1 - 3.13).

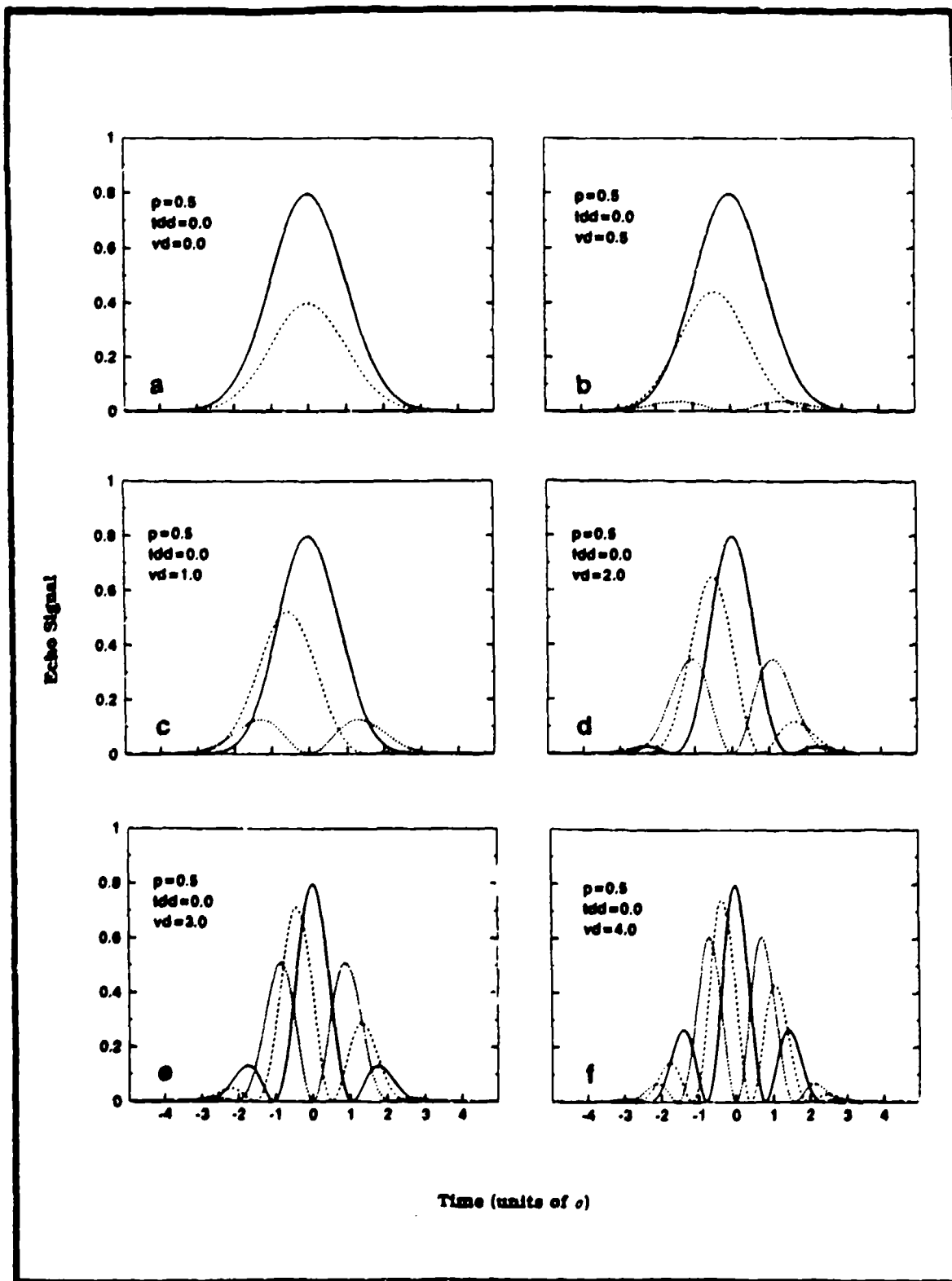


Fig. 3.2 Echo signal patterns from two equal strength, moving backscatters with changing values of relative velocity and separation value of zero.

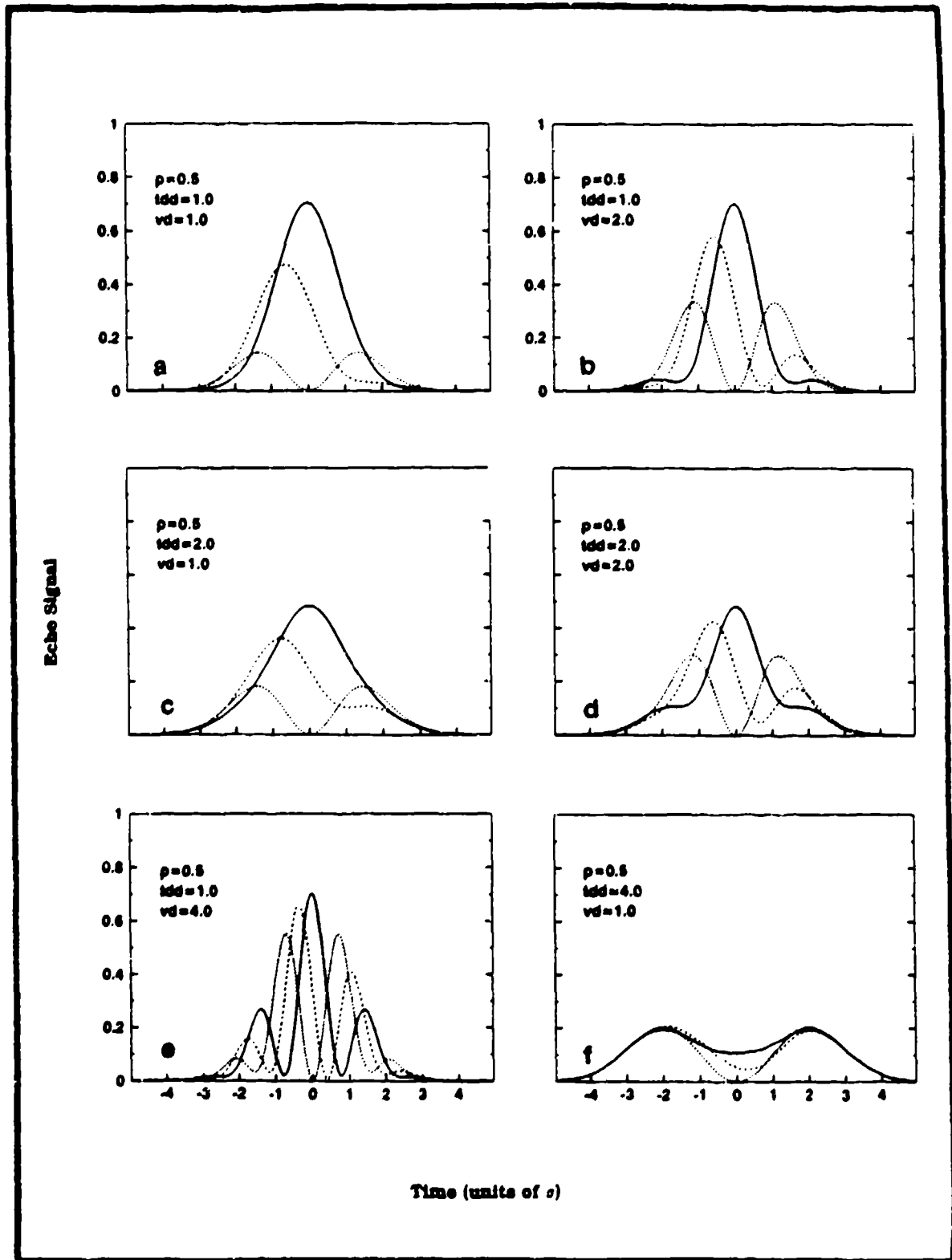


Fig. 3.3 Echo signal patterns from two equal strength backscatters; selected values of separation and relative velocity.

all three patterns are almost identical, as the overlap between signals from two components of the target becomes negligible. Fig. 3.2 shows the echo patterns for maximum overlap of backscattered fields when temporal separation of targets is zero and for different relative velocities. Note the similarity of patterns corresponding to $\psi = 180^\circ$ in Fig. 3.2b and 3.1c with the pattern corresponding to the same phase in Fig. 3.1b and 3.1c. In Fig. 3.2d we observe asymmetry for the case corresponding to $\psi = 90^\circ$. As relative velocity increases, echo signals are becoming more oscillatory, the width of individual peaks narrows ($\sim 1/vd$) and the envelopes of oscillatory pattern are provided by patterns for $vd = 0$, $\psi = 0^\circ$ and $\psi = 180^\circ$ (for arbitrary p).

In Fig. 3.3 we plotted echo signals for selected cases of nonzero temporal separations and relative angular Doppler shifts. While some patterns are quite different from those in Fig. 3.1 and 3.2, some are similar. For instance, comparing Fig. 3.1e and Fig. 3.3f we expect it may be difficult to make proper pattern classification in the presence of noise. As we could expect, only patterns corresponding to $\psi = 180^\circ$ have zeros. It is important to note that patterns with $p = 1/2$ have a structure that is most pronounced, for p approaching 0 (or 1) the echo signal will be represented by a Gaussian shape with weak modulations.

3.2.2 Performance Measures

The performance of the estimators of pattern parameters is evaluated by utilizing the Cramér-Rao bounds¹⁰. These bounds are simple lower bounds on variances of unbiased estimators. In this report we study the sensitivity of the CRB's to the temporal separation of point targets, their amplitudes, relative phase and relative velocity (Doppler shift).

In general, if parameters (\underline{A}) are arranged in such a way that the first m components of vector \underline{A} denote unknown deterministic parameters, then the Cramer-Rao bounds on the variance of unbiased estimators \hat{A}_i ($i = 1, \dots, m$) are computed from the $m \times m$ Fisher information matrix $J(\underline{A})$ with elements $J(\underline{A})_{ij}$ given by:

$$J(\underline{A})_{ij} = \left\langle \left\langle \frac{\partial \ln p(\underline{n} | \underline{A})}{\partial A_i} \cdot \frac{\partial \ln p(\underline{n} | \underline{A})}{\partial A_j} \right\rangle \right\rangle_{\underline{n}} \quad (3.26)$$

where $\langle \cdot \rangle_{\underline{n}}$ stands for averaging over all realizations of \underline{n} governed by the distribution $p(\underline{n} | \underline{A})$.

The CRB's for variance of estimators A are given by the diagonal elements of the inverted information matrix denoted as $(J^{-1}(\underline{A}))_{ij}$ so that:

$$\text{var } \hat{A}_i \geq (J^{-1}(\underline{A}))_{ii} = \text{CRB}(\hat{A}_i, \underline{A}) \quad (3.27)$$

Set (\underline{A}) of deterministic parameters can contain $\tau, \Delta\tau, \Delta\omega, p, N_s$ and ψ (or related parameters). For the probability distribution functions (PDF) $p(\underline{n} | \underline{A})$ which are the products of PDF's such as those in Eq. (3.18), the Fisher information matrix $J(\underline{A})_{ij}$ is given by:

$$J(\underline{A})_{ij} = \sum_{k=1}^L \left\langle \left\langle \frac{\partial \ln p(n_k | \underline{A})}{\partial A_i} \cdot \frac{\partial \ln p(n_k | \underline{A})}{\partial A_j} \right\rangle \right\rangle_{\underline{n}} \quad (3.28)$$

When signal statistics are governed by Poisson distribution, Eq. (3.28) becomes:

$$J(\underline{A})_{ij} = \sum_{k=1}^L \frac{1}{\langle n_k \rangle} \frac{\partial \langle n_k \rangle}{\partial A_i} \cdot \frac{\partial \langle n_k \rangle}{\partial A_j} \quad (3.29)$$

where $\langle n_k \rangle$ denotes the expected values of registered photocounts.

In the limit of small integration times covering an entire echo signal, Eq. (3.29) can be written in the following form:

$$J(\underline{A})_{ij} = \int_{-\infty}^{\infty} dt \frac{\left[\frac{\partial}{\partial A_i} P(t, \underline{A}) \right] \left[\frac{\partial}{\partial A_j} P(t, \underline{A}) \right]}{P(t, \underline{A}) + \rho} \quad (3.30)$$

This expression remains valid when the observation time is finite, provided that infinite time domain is replaced by integration over a finite one.

The selection of parameters describing the pattern of interest depends on the application. In general, the Fisher information matrix J_{ij} for parameters $B_i = B_i(\underline{A})$ ($i = 1, \dots, m$) is related to the Fisher information matrix J_{ij} for parameters A_i ($i = 1, \dots, m$) as follows:

$$J(\underline{A})_{ij} = \sum_{k, l} \frac{\partial B_k(\underline{A})}{\partial A_i} \tilde{J}(\underline{B})_{kl} \frac{\partial B_l(\underline{A})}{\partial A_j} \quad (3.31)$$

Two important special cases are obtained when the power density of the uniform background is negligible compared to the power of the echo pattern and when the background power is much larger than the signal power. We will refer to these two limiting cases as signal shot noise and background shot noise limited, respectively. In the second case, Eq. (3.30) for the Fisher information matrix may be approximated by:

$$J(\underline{A})_{ij} = \frac{1}{\rho} \int_{-\infty}^{\infty} dt \left[\frac{\partial}{\partial A_i} P(t, (\underline{A})) \right] \left[\frac{\partial}{\partial A_j} P(t, (\underline{A})) \right] \quad (3.32)$$

$\rho = A_n \quad i, j \neq n$

where we assume that the set of estimated parameters does not include μ .

3.2.3 Expressions Used In Numerical Calculations

When computing the Fisher information matrix, for the most general case of six unknown parameters, twenty-one integrals have to be computed since matrix $J(\underline{A})_{ij}$ is symmetric. Each integral may depend on up to seven parameters (including background density ρ). Diagonal matrix elements of the inverse of this 6 x 6 matrix provide the bounds on parameter estimation. Note that for small temporal or small velocities separations of point targets, the Fisher information matrix can become ill-conditioned.

In order to achieve numerical stability, it may be helpful to find the relationships between various matrix elements. To reduce the amount of numerical computations, and to

clarify the dependence on various parameters defining the pattern of interest, it is useful to identify those parameters which can be removed by appropriate transformations of matrix elements. It is also useful to determine the minimum number of significant parameters. Examining Eq. (3.30), we note that by multiplying elements of the Fisher information matrix by some power of N_{S0} , we can make these elements dependent on N_{S0} only through a factor of ρ/N_{S0} . This scaling property allows the following factorization of the bounds:

$$\begin{aligned} N_s \text{ CRB} (\hat{A}_i) &= N_s f_{A_i} \left(\tau, \Delta\tau, \Delta\omega, p, N_s, \psi, \rho \right) \\ &= f_{A_i} \left(\tau, \Delta\tau, \Delta\omega, p, N_s, \psi, \rho/N_s \right) \end{aligned} \quad (3.33a)$$

for $A_i \neq N_s$, and

$$\begin{aligned} \frac{1}{N_s} \text{ CRB} (\hat{N}_s) &= \frac{1}{N_s} f_{N_s} \left(\tau, \Delta\tau, \Delta\omega, p, N_s, \psi, \rho \right) \\ &= f_{N_s} \left(\tau, \Delta\tau, \Delta\omega, p, 1, \psi, \rho/N_s \right) \end{aligned} \quad (3.33b)$$

If the observation time covers the entire echo pattern, in the limit of small integration times, we observe that all matrix elements are τ independent. This is due to the fact that the dependence on τ in Eq. (3.30) can be removed by a simple change of variables (consisting of translation by τ). Without any loss of generality, we may set τ equal to 0 in Eqs. (3.33a) and (3.33b).

These considerations lead to the reduction of the number of nontrivial parameters from seven to five, i.e., $\Delta\tau, \Delta\omega, p, \psi, \rho/N_s$. In the shot noise limited case, the number of parameters is equal to four. This is also the number of parameters in background limited case if the CRB's are scaled by an additional factor of N_s/ρ (or N_s/N_B where $N_B = \rho\sigma$ if we adopt our convention for time scale) to obtain results that are independent of N_s/ρ .

Since the Fisher information matrix can be ill-conditioned, it is useful to establish additional relations in special cases in order to detect possible numerical instabilities which may occur. An important special case corresponds to the signal shot noise limited conditions. If we set $\rho = 0$, the following matrix elements can be easily evaluated (see Eq. (3.30):

$$J_{N_s N_s} = N_T / N_s^2, \quad J_{N_s A_i} = \left(\frac{\partial N_T}{\partial A_i} \right) \frac{1}{N_s}, \quad (A_i \neq N_s) \quad (3.34)$$

In addition, an interesting special case under signal shot noise limited conditions is obtained if we assume the value of $\Psi = 0$ or π (Ψ maybe known or unknown) and the remaining part of the argument of $\cos(\cdot)$ function in Eq. (3.21) identically vanish, which happens when $\Delta\omega + a\omega_0\Delta\tau = 0$. In this case most of the matrix elements of the Fisher information matrix can easily be evaluated. Indeed, let us assume for simplicity that $\Delta\omega = 0$, then, all nontrivial matrix elements $J_{ij}; A_i, A_j \neq \Psi, \Delta\omega$ can be explicitly evaluated.

$$P(t; (\underline{A})) = \left\{ \sqrt{N_s} \left[\sqrt{p} z(t + \tau - \frac{\Delta\tau}{2}) + \epsilon \sqrt{(1-p)} z(t + \tau + \frac{\Delta\tau}{2}) \right] \right\}^2$$

$$= (L(t; (\underline{A})))^2; \quad \epsilon = \cos\Psi \quad (3.35)$$

Therefore, the information matrix $J((\underline{A}))_{ij} (A_i, A_j \neq \Delta\omega, \Psi)$ can be written in the following form:

$$J((\underline{A}))_{A_i A_j} = 4 \int_{-\infty}^{\infty} dt \left[\frac{\partial}{\partial A_i} L(t; (\underline{A})) \right] \left[\frac{\partial}{\partial A_j} L(t; (\underline{A})) \right] \quad (3.36)$$

$$= 4 \frac{\partial}{\partial \tilde{A}_i} \frac{\partial}{\partial A_j} \int_{-\infty}^{\infty} dt L(t; (\tilde{\underline{A}})) L(t; (\underline{A})) \Big|_{(\tilde{\underline{A}}) = (\underline{A})}$$

Since L is the sum of two Gaussians and the product of two L -functions is again a combination of Gaussians, the integral in Eq. (3.36) can be easily evaluated. After taking appropriate derivatives, we obtain:

$$J_{N_s N_s} = (1/N_s) (1 + 2\tau T(\Delta\tau, p)), \quad J_{N_s \tau} = 0$$

$$J_{N_s p} = \epsilon \frac{(1-2p)}{p(1-p)} T(\Delta\tau, p), \quad J_{N_s \Delta\tau} = \frac{\epsilon \Delta\tau}{2\sigma^2} T(\Delta\tau, p)$$

$$\begin{aligned}
 J_{pp} &= \frac{N_s}{p(1-p)} [1 - 2\epsilon T(\Delta\tau, p)], & J_{p\tau} &= \frac{\epsilon N_s \Delta\tau}{2p(1-p)\sigma^2} T(\Delta\tau, p) \\
 J_{p\Delta\tau} &= \frac{N_s(2p-1)}{4p(1-p)\sigma^2} \Delta\tau T(\Delta\tau, p), & J_{\tau\Delta\tau} &= \frac{N_s}{2\sigma^2} (2p-1) \\
 J_{\tau\tau} &= \left[N_s / \sigma^2 \right] \left[1 + 2\epsilon \left(1 - (\Delta\tau)^2 / 4\sigma^2 \right) T(\Delta\tau, p) \right] \\
 J_{\Delta\tau\Delta\tau} &= \left[N_s / 4\sigma^2 \right] \left[1 - 2\epsilon \left(1 - (\Delta\tau)^2 / 4\sigma^2 \right) T(\Delta\tau, p) \right] \quad (3.37a)
 \end{aligned}$$

where

$$T(\Delta\tau, p) = \sqrt{p(1-p)} \exp \left[-(\Delta\tau)^2 / 8\sigma^2 \right] \quad (3.37b)$$

Another special case in the shot noise limited regime is obtained when $\Delta\tau = 0$ and $p = 1/2$. Again, one can write $P(t, \underline{A})$ as a square of the simple expression

$$\begin{aligned}
 P(t, \underline{A}) &= \left\{ \left[\frac{2N_s}{\pi\sigma^2} \right]^{1/4} z(t-\tau) \cos \left[\frac{(t-\tau)\Delta\omega + \psi}{2} \right] \right\}^2 \quad (3.38) \\
 &= \left[L'(t; \underline{A}) \right]^2
 \end{aligned}$$

and the information matrix can be written in a form analogous to Eq. (3.26) with function L replaced by L' . After evaluating the integral and its derivatives, we obtain:

$$\begin{aligned}
 J_{N_s N_s} &= (1/N_s) (1 + S(\Delta\omega) \cos\psi), & J_{N_s \tau} &= 0, \\
 J_{N_s \Delta\omega} &= -\sigma^2 \Delta\omega S(\Delta\omega) \cos\psi, & J_{N_s \psi} &= -S(\Delta\omega) \sin\psi, \\
 J_{\tau\tau} &= \left[N_s / \sigma^2 \right] \left[(\sigma \Delta\omega)^2 + 1 + S(\Delta\omega) \cos\psi \right], \\
 J_{\Delta\omega \Delta\omega} &= \sigma^2 N_s \left[1 + S(\Delta\omega) \left((\sigma \Delta\omega)^2 - 1 \right) \cos\psi \right],
 \end{aligned}$$

$$\begin{aligned}
 J_{\tau\Delta\omega} &= -N_s S(\Delta\omega) \sin\psi, & J_{\psi\psi} &= N_s [1 - S(\Delta\omega) \cos\psi], \\
 J_{\psi\Delta\omega} &= N_s \sigma^2 \Delta\omega S(\Delta\omega) \sin\psi, & J_{\tau\psi} &= -\Delta\omega
 \end{aligned}
 \tag{3.39a}$$

where

$$S(\Delta\omega) = \exp(-(\sigma\Delta\omega)^2/2)
 \tag{3.39b}$$

Similar formulas can be obtained for the background limited case when the information matrix $J(\underline{A})_{ij}$ can be written in the following form:

$$J(\underline{A})_{A_i A_j} = (1/\rho) \frac{\partial}{\partial A_i} \left. \frac{\partial}{\partial \tilde{A}_j} \int_{-\infty}^{\infty} P(t, \underline{A}) P(t, \tilde{\underline{A}}) dt \right|_{\tilde{\underline{A}} = \underline{A}}
 \tag{3.40}$$

Again, the integral can be evaluated and derivatives performed leading to closed form expressions for all matrix elements. These important formulas are more complicated and will be presented and discussed elsewhere.

In numerical calculations of the Fisher information matrix, an integration time interval of 15σ was used. The integration grid consisted of 1000 points. The loss of accuracy due to a finite integration region and coarseness of the integration grid did not exceed a few percent for the considered values of the parameters.

In some trials for very small temporal separations and velocities ($td \leq 0.1$, $vd \leq 0.1$) the Fisher information matrix became numerically unstable and quadruple precision was necessary to obtain meaningful results.

3.2.4 Discussion of Results

The sensitivity of estimation for any given parameter depends on the actual values of that parameter, and on parameters describing a two point target. In addition the accuracy of estimation depends on whether the other parameters are known. Once the Fisher information matrix is computed for the general case, the bounds can be obtained for special cases by

inverting an appropriate submatrix when some of the parameters are known. Eq. (3.31) allows us to derive the transformed Fisher information matrix for any function of our selected canonical parameter set and thus obtain the desired bounds.

Two limiting cases discussed here correspond to the signal shot noise and background limited cases. In these two limits the signal dependence is easily scaled out and results depend on the values of only four parameters: temporal separation of two targets $\Delta\tau$, fractional strength of the first target P , and the relative phase angle Ψ and angular Doppler frequency shift $\Delta\omega$.

The following figures describe the accuracy of estimation of the echo for various pattern parameters as a function of temporal separation between two point targets and relative Doppler shift. Six consecutive figures, 3.4 through 3.9, are arranged in similar fashion: the left panels refer to cases when all parameters are known except the one being estimated; the right panels refer to cases when all parameters are unknown. All panels correspond to the true value of $p = 1/2$ and each panel contains three graphs corresponding to different values of relative phase; $\Psi = 0^\circ$ (solid line) $\Psi = 90^\circ$ (dashed line) and $\Psi = 180^\circ$ (dotted line) used before. Alternate sets of figures show signal shot noise limited cases and background shot noise limited cases, respectively. Note that dependence on signal value was scaled out. In these figures, N_B denotes the average number of background photons registered in time σ .

We first consider the estimator for the temporal separation of two point targets. A comparison of three cases in Fig. 3.4a shows behavior which may be surprising: for small separations it is advantageous to have point targets in phase opposition rather than in phase or phase quadrature. This is despite the much smaller number of photons available in the pattern (see Fig. 3.1a - 3.1b). The apparent contradiction is easily explained since this is a case in which all other parameters and, in particular, the expected number of photons are known. It is this small number of registered photons that indicates that the temporal distance between point targets must be small. Indeed, in Fig. 3.4b, corresponding to the case in which all parameters are unknown, the performance of the estimator of temporal separation is reversed; it is best when targets are in phase, and worst when they are in phase opposition.

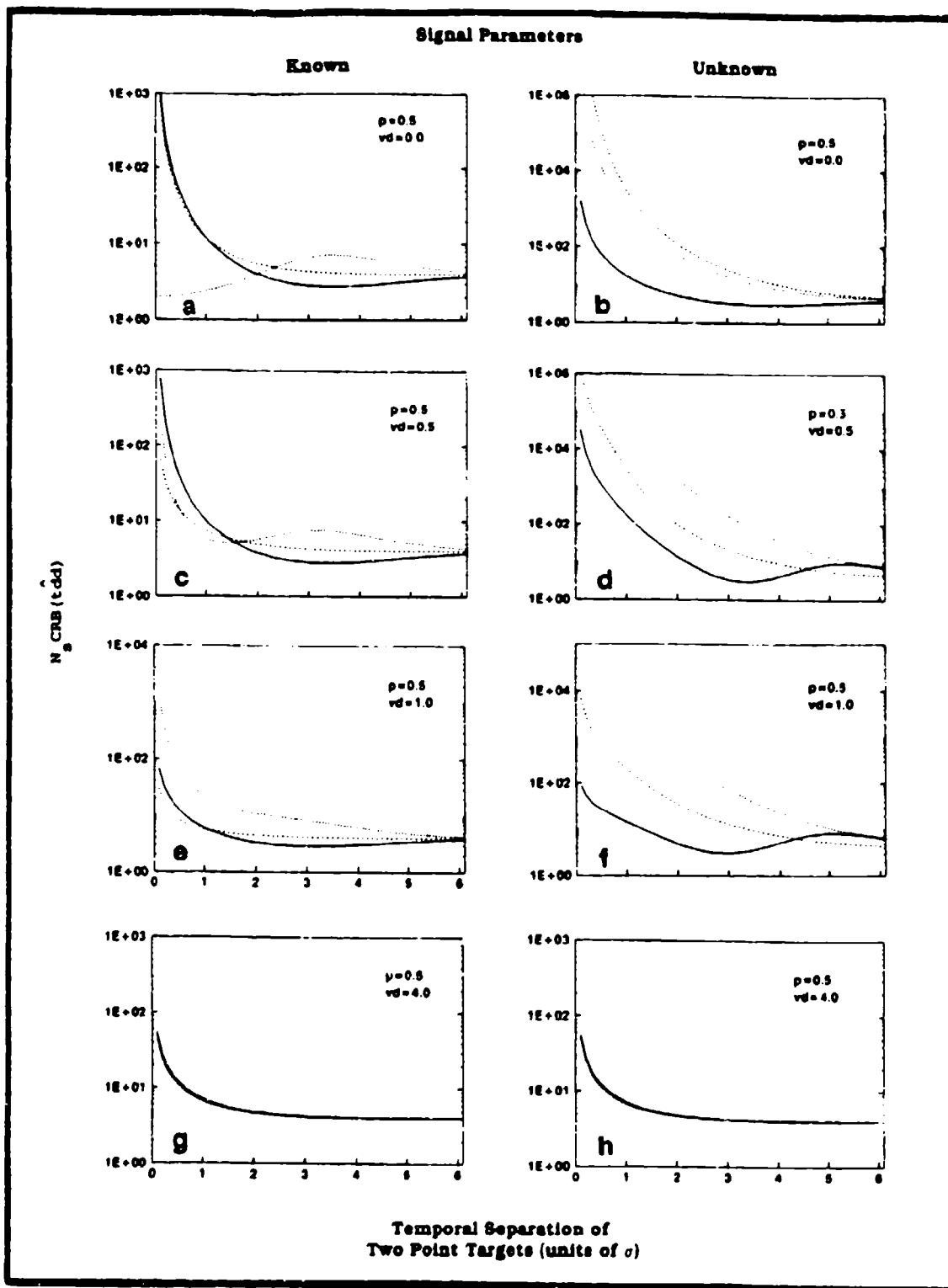


Fig. 3.4 Dependence of scaled CRB (tdd) on temporal separation of two point targets of equal strength; selected cases for different values of relative velocity. Signal shot noise limited conditions.

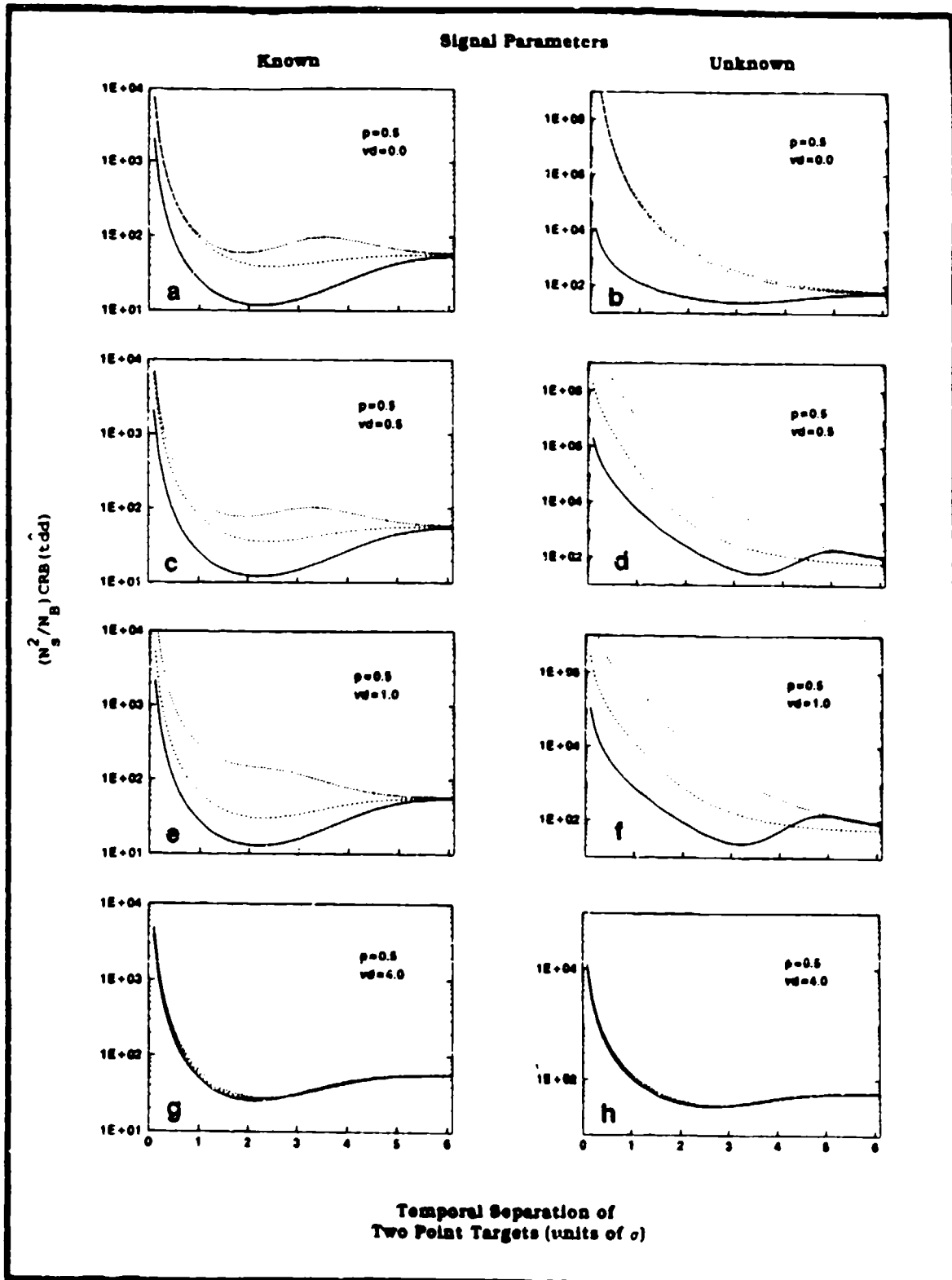


Fig. 3.5 Dependence of scaled CRB (tdd) on temporal separation of two point targets of equal strength; selected cases for different values of relative velocity. Background shot noise limited conditions.

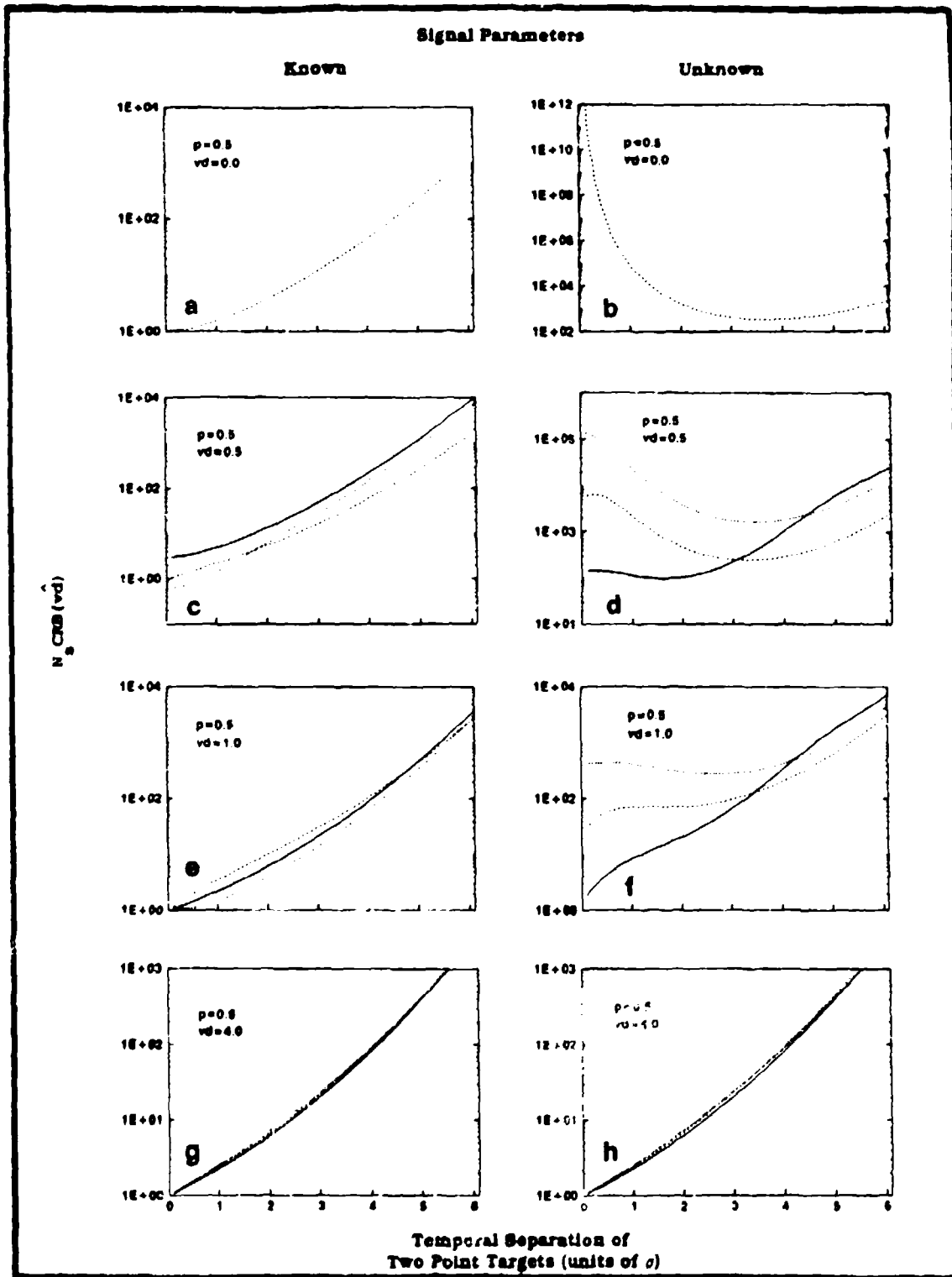


Fig. 3.6 Dependence of scaled CRB ($\hat{v}d$) on temporal separation of two point targets of equal strength; selected cases for different values of relative velocity. Signal shot noise limited conditions.

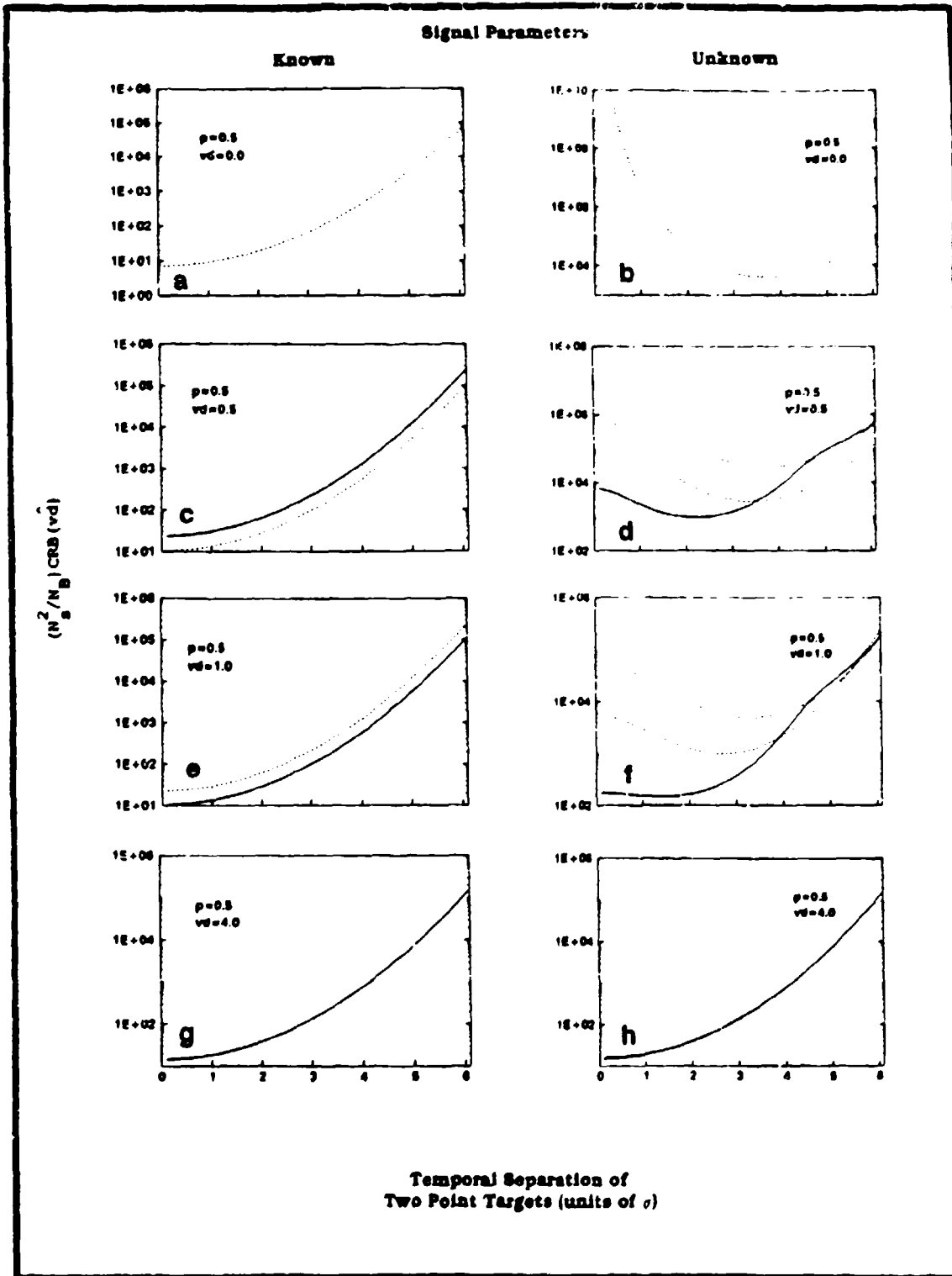


Fig. 3.7 Dependence of scaled CRB ($\hat{v}d$) on temporal separation of two point targets of equal strength; selected cases for different values of relative velocity. Background shot noise limited conditions.

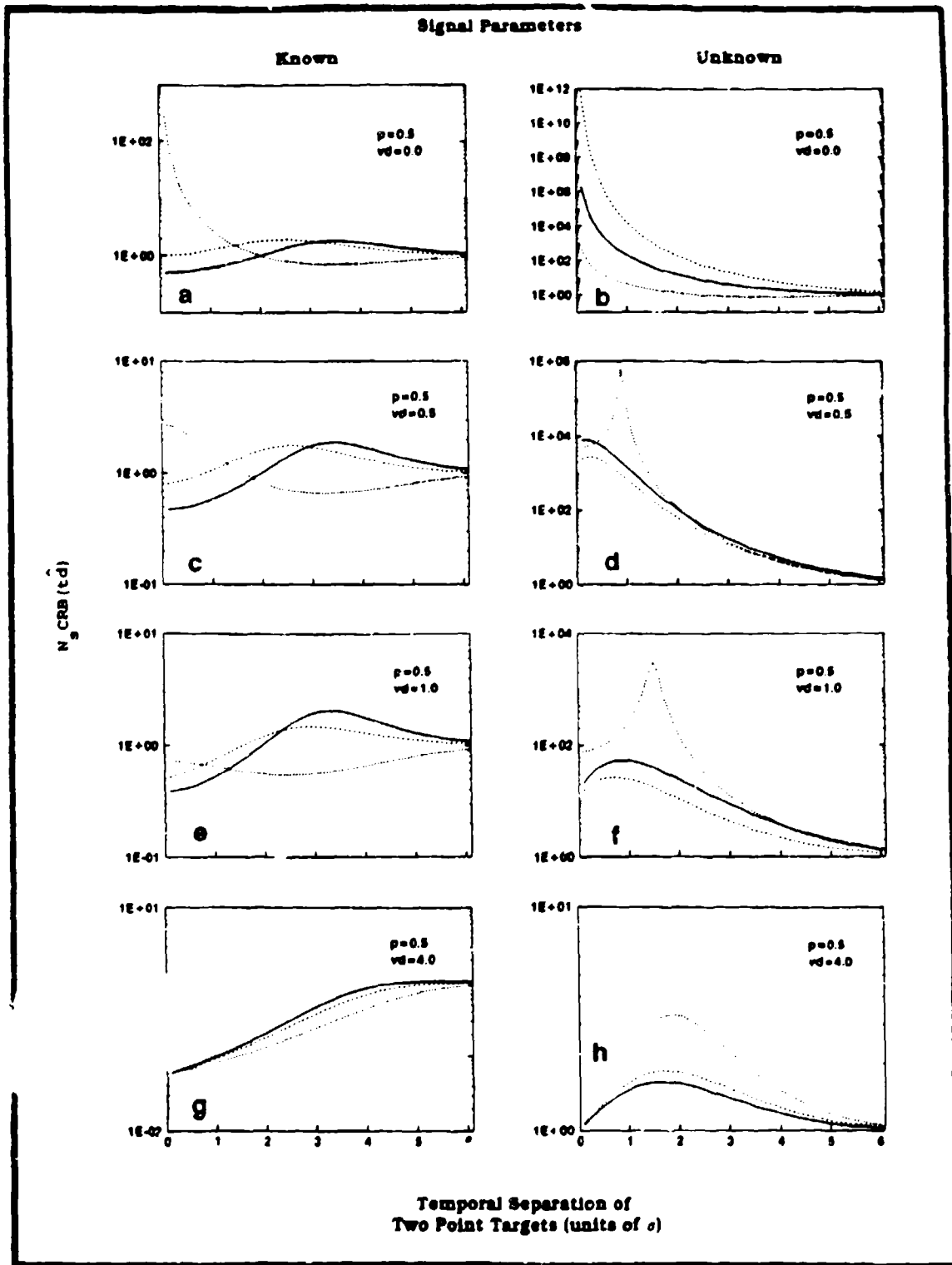


Fig. 3.8 Dependence of scaled CRB (\hat{d}) on temporal separation of two point targets of equal strength; selected cases for different values of relative velocity. Signal shot noise limited conditions.

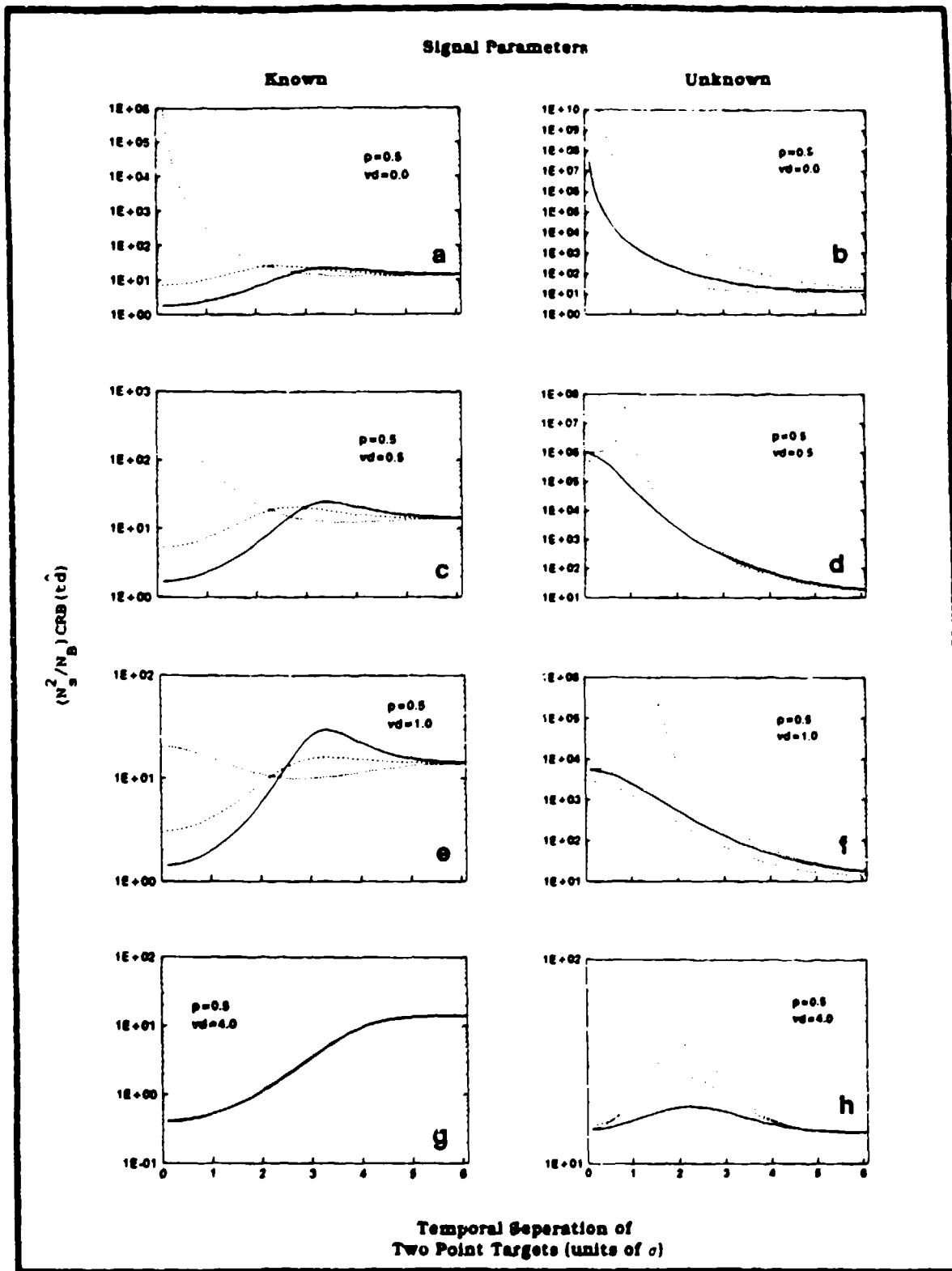


Fig. 3.9 Dependence of scaled CRB (\hat{td}) on temporal separation of two point targets of equal strength; selected cases for different values of relative velocity. Background shot noise limited conditions.

RIVERSIDE RESEARCH INSTITUTE

Fig. 3.5a (background limited case), shows that for small separations, performance is best for the case when targets are in phase, and slightly worse when the targets are in phase opposition or quadrature. This is what one would expect; in the presence of background generated shot noise, absence of the signal is not a very good indicator of temporal separation. Figs. 3.4c, 3.4e, and 3.4g describe the performance of estimator of temporal separation for nonzero relative target velocity. In contrast to the static case, selection of $\psi = 180^\circ$ no longer gives the best performance of the estimator. The presence of relative motion can lead to improved performance for some values of temporal separations and phases, and degraded performance for others. It is important to note that for angular Doppler shifts (vd) of the order of four and larger, the performance of estimators of temporal separations becomes phase and velocity independent (Fig. 3.4g). Since for large temporal separation overlap of backscattered fields from two target components is negligible, independence of the estimator of separation on phase, velocity and temporal separation is expected for large tdd . This behavior is indeed observed in all panels of Figs. 3.4 and 3.5.

When we examine Fig. 3.4b, 3.4d, 3.4f and 3.4h, where all parameters are unknown and compare them with the corresponding cases when all parameters but separation are known, we will notice that strong sensitivity to phase decreases with increasing relative velocity and the very poor estimator performance (for small relative velocities) improves as well. Indeed, when $vd = 4.0$, Fig. 3.4g and 3.4h are practically identical, showing little value of a priori knowledge in this case. This is in contrast with the static case, when two sources are in quadrature ($\psi = 90^\circ$) and temporal separation is 1σ ; a comparison of Fig. 3.4a and 3.4b shows that we need approximately twenty-five times more photons to compensate for the lack of a priori knowledge of the other parameter values.

Computation of the minimum average number of registered photons necessary to perform a measurement of temporal separation with given accuracy is straightforward when all other parameters are known. For instance, let $p = 0.5$, $vd = 4.0$, $\psi = 90^\circ$, (so that CRB is described by Fig. 3.4g and assume that we want to measure temporal separations of $tdd = 0.5$

RIVERSIDE RESEARCH INSTITUTE

with accuracy 0.1 (1σ error). From Fig. 3.4g we can determine that $N_s \text{CRB}(\hat{tdd})$ is approximately 10 for temporal separation 0.5. Since the $\text{CRB}(\hat{tdd})$ has to be smaller than $(0.1)^2 = .01$ for the required accuracy, the minimum required number N_s of photons is 1000. When more parameters are unknown, such calculations may not be sufficient and may require for instance finding the bound on $\text{CRB}(\hat{tdd})$ when other parameters vary within the required range. (See some additional comments in the discussion of midpoint time delay estimation).

Note that for very small separation, the estimation bounds in some cases seem to diverge. In Fig. 3.4a, we can see that for small separations and sources in phase opposition, the bound has a finite limit, while for sources in phase, we observe divergent behavior. This also seems to be true for sources in quadrature. One can analytically verify this behavior. For the case when all parameters are known, divergent behavior is often observed only for special parameter values, e.g., $p = 1/2$. When all parameters are unknown, however, divergent behavior for small separations is prevalent. This divergence is related to the nonexistence of unbiased parameter estimators for small temporal separations. This behavior for small separations will be discussed elsewhere. The present remarks apply as well to the behavior observed for the other parameter estimators.

With the exceptions mentioned already, Fig. 3.4 and Fig. 3.5 are remarkably similar. In the background limited case temporal separation estimators seem to be more phase sensitive and their variance may vary within a larger range.

The next estimator considered is for angular Doppler frequency shift shown in Fig. 3.6 and 3.7 for signal shot noise and background limited conditions, respectively. The first observation is that Fig. 3.6a as well as Fig. 3.6b, 3.7a and 3.7b display only one bound corresponding to $\psi = 90^\circ$. This is because finite variance unbiased estimators of vd do not exist for $\psi = 0^\circ$ and 180° and for relative velocities approaching zero. It is not difficult to understand why this is the case. Angular Doppler frequency shift enters echo signal in Eq. 3.38 through a $\cos(\cdot)$ factor. For phase angle $\psi = 0^\circ$ and 180° and for very small velocities,

RIVERSIDE RESEARCH INSTITUTE

expansion of $\cos(\cdot)$ leads to a term proportional to $(\Delta\omega)^2$. For $\psi = 90^\circ$ in similar conditions, the first term in expansion is proportional to $\Delta\omega$. This indicates that an unbiased estimator of $\Delta\omega$ may exist for $\psi = 90^\circ$ but not for $\psi = 0^\circ$ or 190° (and an unbiased estimator of $(\Delta\omega)^2$ may, however, exist for these two phase angles). Already for small relative velocities, however, corresponding to $vd = 0.5$, we have a full set of bounds for three phase angles. In fact, in the case of known values of pattern parameters, the dependence of the Doppler shift estimator on phase angle is rather weak both for signal shot noise (Fig. 3.6c, 3.6e, 3.6g) and background (Fig. 3.7c, 3.7e, 3.7g) limited performance. For relative velocities of four (Fig. 3.6g and 3.7g) corresponding to vd of the order and larger, the performance of the estimator of relative Doppler shift becomes phase and velocity independent in full analogy with the performance of the estimator of temporal separation. The dependence on phase angle is much stronger when all parameters are unknown (Fig. 3.6d, Fig. 3.6f, Fig. 3.7d, Fig. and 3.7f) but this sensitivity rapidly diminishes with increasing velocity, and for $vd = 4$ (Fig. 3.6h and 3.7h) the performance of an estimator of relative Doppler shift becomes essentially the same case when knowledge about the values of other parameters is available. As we could expect, the performance of estimator of relative Doppler shift rapidly deteriorates with the increase of temporal separation between point targets. The flatness of the performance curve in Fig. 3.6b and 3.7b is due to the choice of performance scale, but it is interesting to note that optimal performance for small velocities is often obtained for rather large temporal separation of point targets.

The next estimator considered is for midpoint time delay. In the static case when all parameters are known, Fig. 3.8a and 3.9a show the expected behavior for small separations; it is more advantageous to have target components in phase rather than in quadrature or phase opposition. This is consistent with the larger number of photons available in such patterns. Different behavior is observed (for small separations) when all parameters are unknown: the performance of the estimator is best when targets are in phase opposition and worst when they are in phase. This result can be explained by correlation of this estimate with an estimator of P (see discussion in reference 13). As expected, for large separation, the performance becomes phase and relative velocity independent and approaches a common limit in all cases whether parameters are known or unknown. Rather unexpected and exotic behavior is observed in cases when all parameters are unknown and relative velocity is nonzero. In both signal shot

RIVERSIDE RESEARCH INSTITUTE

noise and background limited cases for $\Psi = 180^\circ$, the performance bound shows a sharp peak (Fig. 3.8d, 3.8f, 3.9d and 3.9f). This behavior is quite common for small values of P and is due to various exponential and trigonometric factors in elements of the Fisher information matrix, which may lead to rapid change of behavior. With increase of velocity, the dependence on phase is decreasing, but in contrast to two previous estimators, no common limiting performance curve is attained for the cases when pattern parameters are known or unknown. In fact, one can show that for small temporal separations when all parameters are known, CRB ($\hat{\tau}$) decreases as $1/(vd)^2$ (see Eq. (3.39a) for large enough velocities. This supports our intuitive feeling that it is easier to measure position displacement of a more structured pattern. On the other hand, this example shows that some care is necessary in interpreting CRB predictions. Indeed, since CRB is decreasing like $1/(vd)^2$, in order to perform a measurement of pattern position with given accuracy, we will require less than one photon if relative Doppler shift is sufficiently large. This is obviously not a sensible answer. In order to properly use the prediction given by CRB, we should remember that it is a local bound useful only for small parameter changes (compared to fine structure). To use CRB for prediction of pattern shifts in the present application, we should be interested in shifts with errors smaller than the distance between interference fringes. since this distance is of the order of $1/vd$, we can easily establish that sufficiently accurate measurement requires a few dozens of photons. If we examine behavior of the midpoint time delay estimator in the case when all parameters are unknown, behavior of CRB for small displacement seems to indicate that it is also decreasing with increase of relative Doppler shift. However, when we examined the behavior of the bound for $vd = 5$ and $vd = 6$ we observed no further significant decrease from the value observed for $vd = 4$.

Establishment of asymptotic behavior of CRB's for large vd is certainly of interest. Indeed, if observed stagnation of CRB is real, arguments similar to those used in the case when all parameters are known would indicate that the number of photons required for fine pattern shift estimation increases as $(vd)^2$.

RIVERSIDE RESEARCH INSTITUTE

Figures 3.10 and 3.11 are arranged in different fashion than the previous six figures. All panels refer to the cases when signal is unknown and $p = 0.01$. The top four panels describe the performance of the estimators of angular relative Doppler shift for selected values of Doppler shift as a function of temporal separation between point targets, while the bottom four describe the performance of estimator of temporal separation for similar cases. This important case, when backscatter signal from one target component has much higher strength than return from the other component, exhibits highly structured behavior of performance curves. Comparison of Fig. 3.10 for signal shot noise limited case and Fig. 3.11 for background limited performance shows very similar behavior. As relative velocity increases in a similar way as for $p = 1/2$, the performance of estimators becomes phase and relative velocity independent. Similar plots for the case when all parameters are known (not shown) show less dependence on phase angle than for $p = 0.5$, and for high relative velocity they approach the same phase and velocity limit. One can also observe a correlation between some of the kinks and brakes in performance curves of the estimator of Doppler and separation. A more detailed discussion of this behavior in the background limited case will be presented in a forthcoming paper, when analytic results will be available for the Fisher information matrix.

The next two figures illustrate performance of estimators of relative Doppler shift and separation as a function of shot noise limited performance. Fig. 3.12 is for $p = 1/2$, and panels on the left are for signal parameters known while panels on the right are for unknown signal parameters. This figure provides an excellent illustration of how with increase of relative velocity the performance of estimators becomes velocity and phase independent. Similar illustration is provided in Fig. 3.13 where all panels are for unknown signal and panels on the left are for $p = 0.1$ and on the right for $p = 0.01$. Again, one can see a correlation between various abrupt changes in the performance of various estimators. Another interesting type of plots of estimator performance is to present their behavior as a function of phase angle. These figures are not shown here but they demonstrate that best (or worst) performance corresponds in general (for $v_d \neq 0$) to phase angles different than three standard phases selected in our figures.

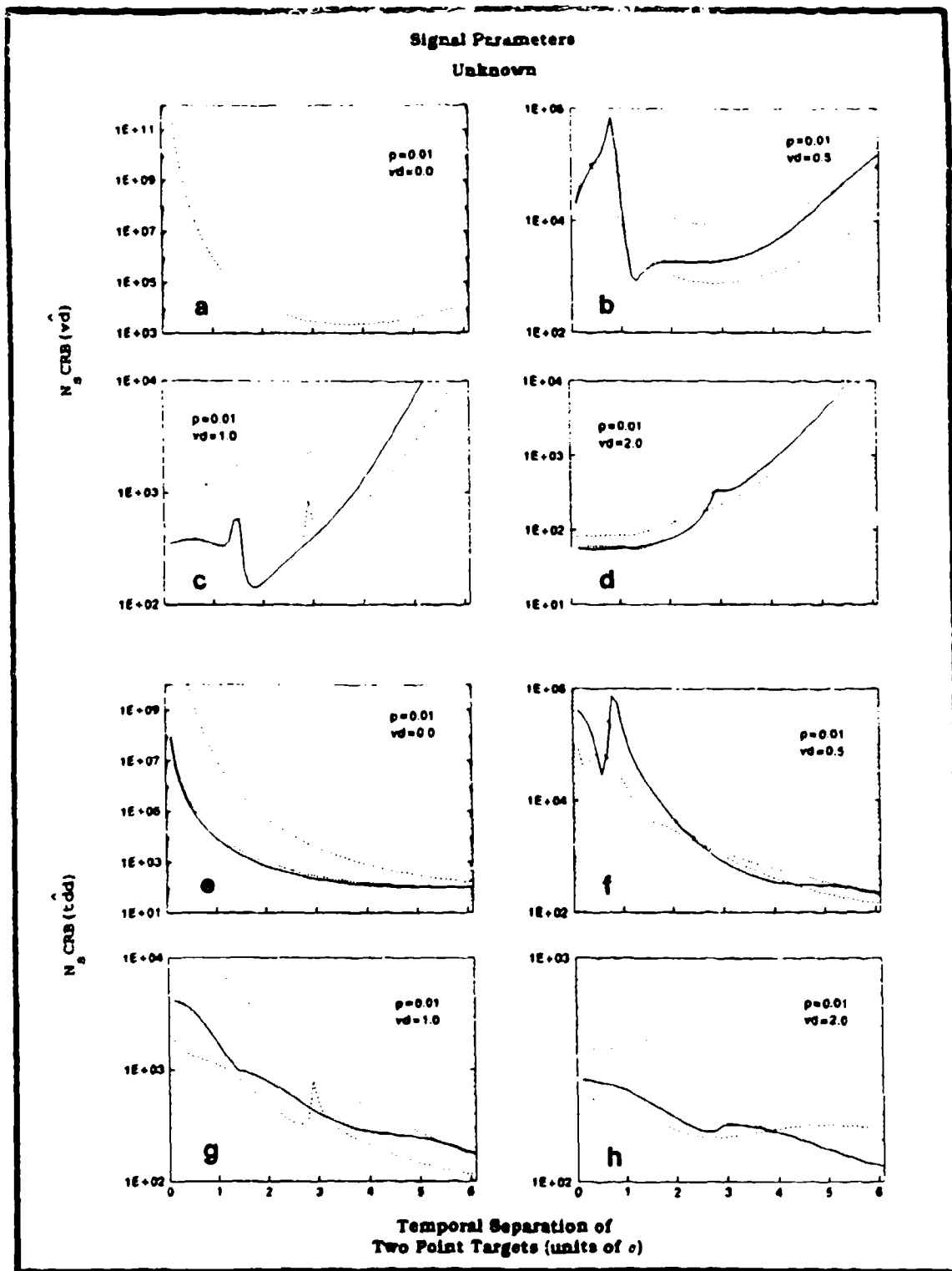


Fig. 3.10 Dependence of scaled CRB ($\hat{v}d$) and CRB ($\hat{t}dd$) on temporal separation of two point targets of differing strength; selected cases for different values of relative velocity. Signal shot noise limited conditions.

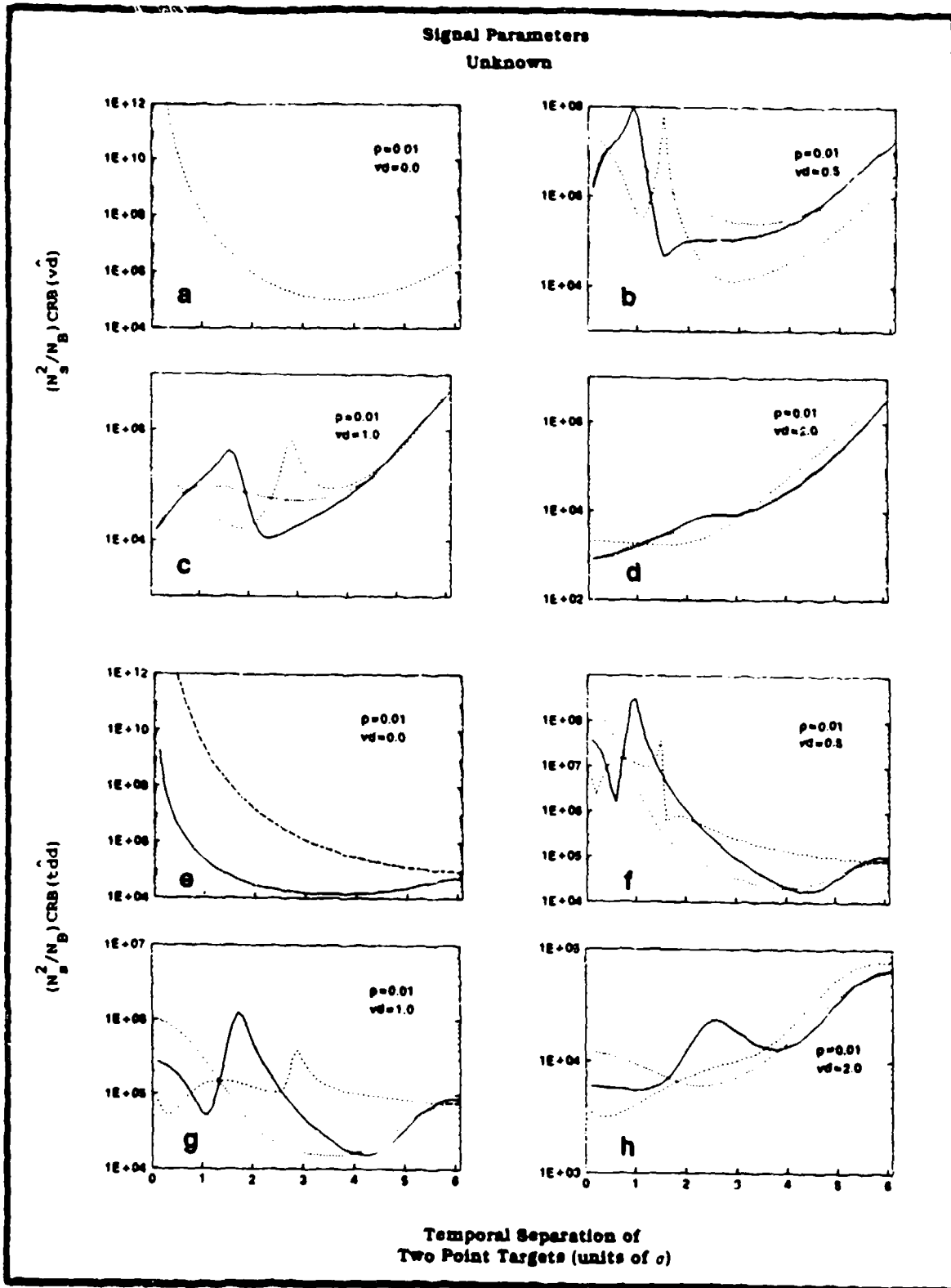


Fig. 3.11 Dependence of scaled CRB (\hat{v}_d) and CRB (\hat{t}_{dd}) on temporal separation of two targets of differing strength; selected cases for different values of relative velocity. Background shot noise limited conditions.

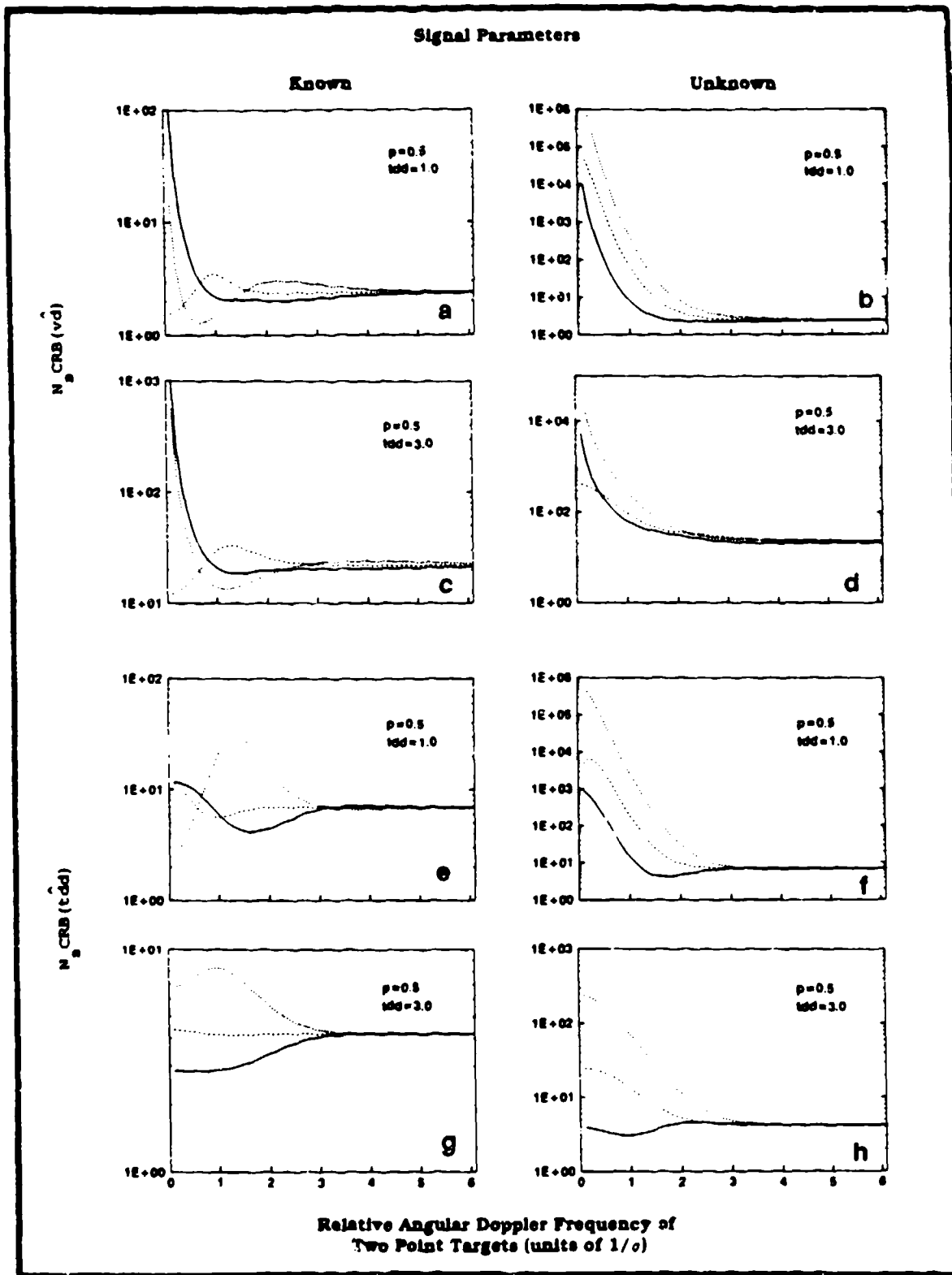


Fig. 3.12 Dependence of scaled CRB (\hat{v}) and CRB (\hat{t}) on relative angular Doppler shift; of two point targets of equal strength; selected cases for different values of temporal separation. Signal shot noise limited conditions.

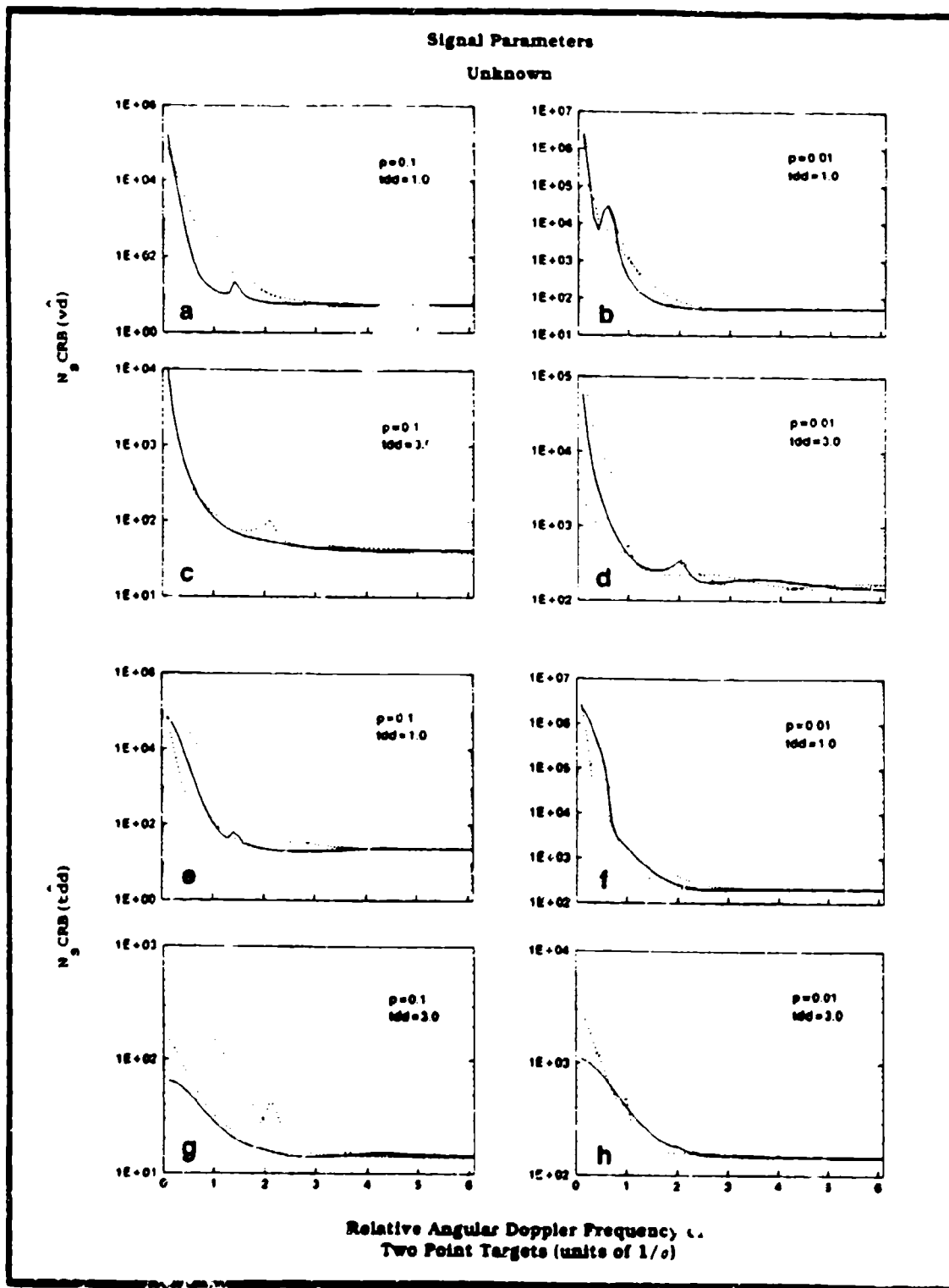


Fig. 3.13 Dependence of scaled CRB (\hat{v}_d) and CRB (\hat{t}_{dd}) on relative angular Doppler shift; at two point targets of different strength; selected cases for different values of temporal separation. Signal shot noise limited conditions.

The value of a priori knowledge in parameter estimation is illustrated in Fig. 3.14. This figure shows the sensitivity of midpoint time delay and relative angular Doppler shift estimation for varying numbers of unknown parameters for signal shot noise limited performance. Panels on the left are for phase $\Psi = 0^\circ$ and on the right for $\Psi = 180^\circ$. Top panels and for $p = 1/2$ and bottom panels are for $p = 0.01$.

When we examine Fig. 3.14a we observe that knowledge of P (cases b) or Ψ (case c) brings substantial improvement in estimator performance in some ranges of temporal separation. When both parameters are known (case d) performance is essentially the same as in case of knowledge of all parameters. Fig. 3.4b shows a more dramatic change. Knowledge of p (case a) or Ψ (case b) leads to the performance close to one obtained with knowledge of all nuisance parameters (case d). In fig. 3.14c and 3.14d we observe more gradual improvement with increase of a priori knowledge. This improvement can be expressed in terms of smaller number of photons necessary to perform the measurement with required accuracy. Such considerations provide good illustration of the observation that achievable resolution depends not only on signal value but also on the amount of a priori knowledge available about the echo pattern.

3.2.5 Summary and Conclusions

The fundamental limits were established for the accuracy of the estimation of range and velocity resolution for autodyne detection of a two point target with pulsed laser radar consisting of a transmitter collocated with a photon bucket receiver. The Cramer-Rao bounds (CRB's) were computed for both the signal shot noise and background limited cases. From these bounds, the number of signal photons necessary to estimate a parameter with a desired accuracy may be determined. The study of longitudinal position estimation can be of interest in tracking applications.

The sensitivity of the bounds to different parameter values and changes in the number of unknown parameters was established. The value of a priori knowledge in parameter estimation was demonstrated and related to the number of unknown

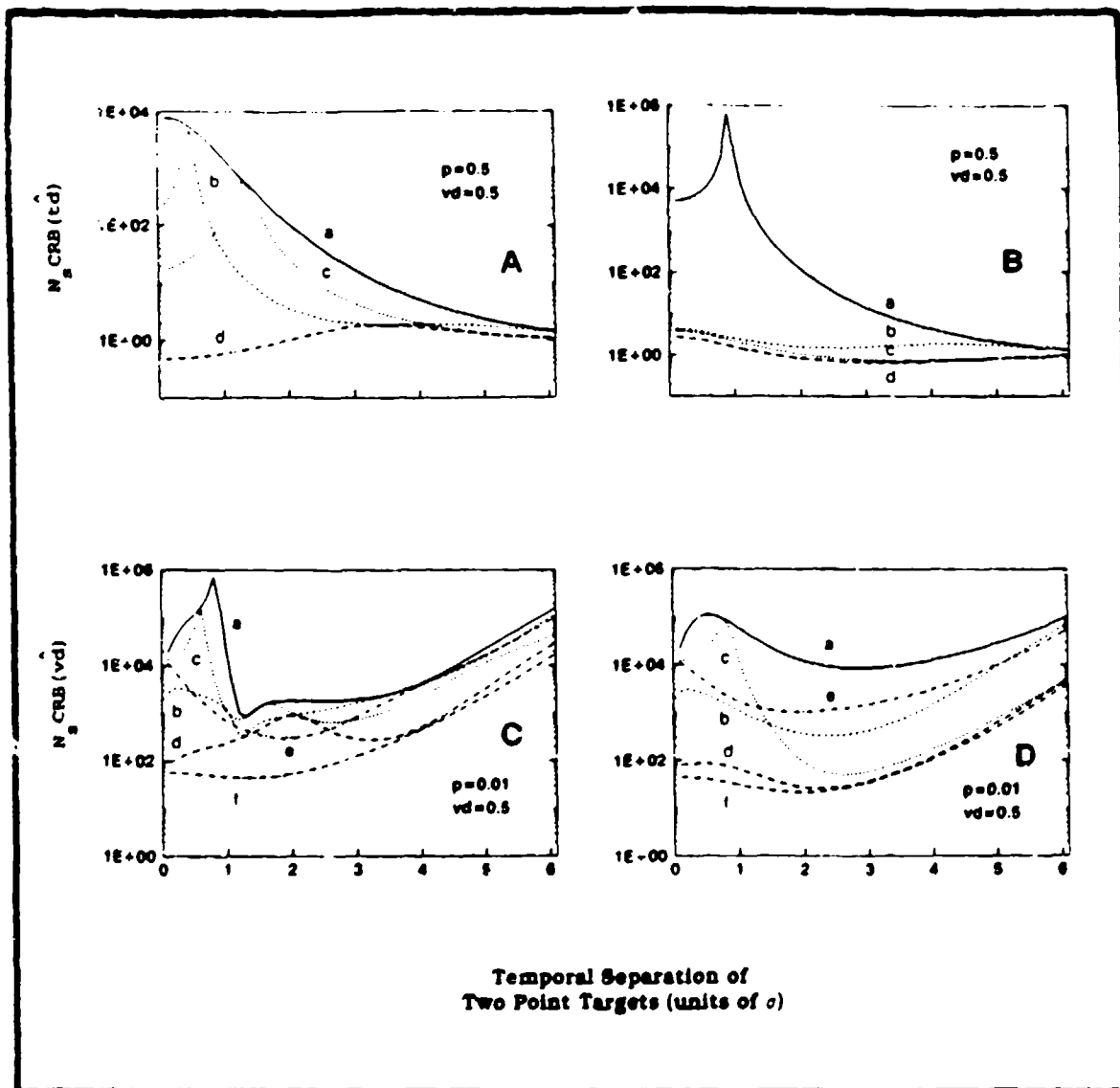


Fig. 3.14 Dependence of scaled CRB ($\hat{t}d$) and CRB ($\hat{v}d$) on the number of unknown parameters. Panels A and C: phase angle $\psi = 0^\circ$; panels B and D: phase angle $\psi = 180^\circ$. For panels A and B, curve designations are: a - all parameters unknown; b - all parameters except p unknown; c - all parameters except ψ unknown; d - all parameters except p and ψ unknown (in this case identical curves are obtained if all parameters are known). For panels C and D, curve designations are: a, b, c and d - as in panels A and B; e - all parameters except t_d and t_{dd} unknown; f - all parameters are known.

RIVERSIDE RESEARCH INSTITUTE

parameters. An important issue of practical consequence, which remains to be addressed in future work is the effect of detector response time on parameter estimation of echo signals.

The double point target provides us with a wide parameter space. The extension of this work could be useful in introducing the natural metric in parameter space for the proper evaluation of the information content in echo signals. The bound on estimator performance was obtained for a single laser pulse. In many situations of practical interest, the values of N_{s1} , N_{s2} and Ψ will fluctuate from pulse to pulse. Evaluating the performance of a multipulse system is certainly of great interest. A few minor gaps remain to be filled in order to make this analysis complete. This includes analysis of potential benefits of pulse wavefront design.

One of the results obtained was that for large relative Doppler shift a few tens of photons are required to measure the Doppler shift with moderate accuracy (say $\Delta v d \sim 1$). To put such predictions on a firm footing, one has to construct estimators with variances approaching the CRB. It is easy to find such an example applicable to problems in which fine parameter estimation is of interest, e.g., alignment and calibration when the uncertainty of the parameter value is small. The form of locally optimal estimators is given by:

$$\hat{\Delta \underline{A}}_i = \sum_{j=1}^6 \frac{\partial \ln p(\underline{n} | \underline{A})}{\partial A_j} [J(\underline{A}_0)]_{ij}^{-1} \Big|_{\underline{A}=\underline{A}_0} \quad (3.41)$$

This estimator is for small displacement of \underline{A} from \underline{A}_0 . It is a biased estimator; however, its bias is negligibly small for small displacements from \underline{A}_0 and its variance attains the CRB at \underline{A}_0 .

Another important class of estimators useful for a larger class of applications are the maximum likelihood estimators (MLE). These estimators are applicable to larger parameter variations, and approach the CRB for large signal values. The methods of implementation for the MLE estimators, together with other practical considerations and types of estimators are important problems which should be addressed in future work.

3.3 REFERENCES

1. D. V. Fluckiger, R. J. Keyes, and J. H. Shapiro, "Optical Autodyne Detection Theory and Experiment", *Appl. Opt.* 26, 318 (1987).
2. Elbaum, M., Kingsbury, B., Nowakowski, J., Shultz, T., and Simuoli, V., "Moving Target: Indication and Position Estimation with Autodyne Detection", *SPIE*, Vol. 1111, p. 226, (1989).
3. R. E. Hufnagel, "Propagation Through Atmospheric Turbulence", *The Infrared Handbook*, W. L. Wolfe, G. J. Zissis, (Editors), ERIM (1978).
4. J. Nowakowski, Y. Gorlin, and M. Elbaum, "Imaging Correlography", RRI preprint, (1987).
5. J. Nowakowski, "Analysis of Autodyne Detection", RRI preprint (1987).
6. P. S. Idell, J. R. Fienup, P. S. Goodman, *Opt. Lett.* 12, 858 (1987).
7. Elbaum, M., Nowakowski, J., Gutkowitz-Krusin, D., Wlodawski, M., and Gorlin, Y., "Self-Reference Holographic Imaging Using Nonuniform Illumination", *Opt. Lett.*, Vol. 13, p. 81, (1988).
8. Elbaum, M., Nowakowski, J., Gutkowitz-Krusin, D., and Wlodawski, M., "Coherent Radiation Imaging and Tracking via Illumination Coding (CRITIC)", *SPIE*, Vol. 1111, p. 241, (1989).
9. Elbaum, M., Nowakowski, J., Gutkowitz-Krusin, D., and Wlodawski, M., "Robust High Resolution Laser Radar". 14th DARPA Strategic Systems Symposium", Monterey, CA, October 14-17, (1988).
10. H. L. Van Trees, "Detection, Estimation, and Modulation Theory", Part 1, pp. 66-73, John Wiley and Sons, Inc., (1968).
11. Nowakowski, J., and Elbaum, M., "Fundamental Limits in Estimating Light Pattern Position", *J.O.S.A.*, Vol. 73, p. 1744, (1983).
12. D. L. Fried, "Resolution, Signal-to-noise Ratio, and Measurement Precision", *J.O.S.A.*, Vol. 69, No. 3, 399-406 (1979).
13. Nowakowski, J., Simuoli, V., and Elbaum, M., "Fundamental Limits in Resolution of Double Star Targets", *SPIE*, Vol. 1111, p. 352, (1989).

Appendix 1

Acquisition, Tracking, and Pointing III

A Reprint from the

PROCEEDINGS

Of SPIE - The International Society for Optical Engineering



Volume 1111

Acquisition, Tracking, and Pointing III

27-29 March 1989

Orlando, Florida

Coherent radiation imaging and tracking via illumination coding (CRITIC)

Marek Elbaum, Jerzy Nowakowski, Dina Gutkowitz-Krusin, Mitchell Wlodawski

Riverside Research Institute

330 West 42nd Street, New York, New York 10036

Coherent Radiation Imaging and Tracking via Illumination Coding (CRITIC)

Marek Elbaum, Jerzy Nowakowski, Dina Gutkowitz-Krusin, and Mitchell Wlodawski

Riverside Research Institute, 330 West 42nd Street
New York, NY 10036

ABSTRACT

A novel architecture for a lidar transceiver is proposed to achieve high-resolution imaging and precision tracking of complex targets. This architecture combines a conventional imaging receiver (telescope) with a noncoherent sparse array of photon buckets into one system. The diffraction limited resolution of the array exceeds that of the telescope. This lidar architecture is designed to use a new technique, CRITIC, which is based on combining the relevant information obtained simultaneously with the telescope and the array. In particular, the CRITIC technique allows one to overcome several drawbacks of conventional monostatic ladars and opens new prospects for both the ground- and space-based ladars.*

1. INTRODUCTION

Fine resolution imaging of space objects and precision measurement of their angular position is of interest in numerous situations. Active laser sensor systems are considered for these applications.

Conventional tracking ladars use telescopes (coherent antennas) to image a laser illuminated target onto an array of photodetectors. The target image which is formed using a single laser pulse is used for estimating the target position. Typically, the image resolution and angular position estimation achievable with these systems are on the order of the diffraction-limited resolution of the telescope^{1,2}. These ladars operate at the short wavelengths: in the UV, the visible, or SWIR, in order to take advantage of the diffraction-limited performance.

Simplicity of the monopulse ladars is their main advantage for space applications: direct detection method is used for photosensing, high laser spectral purity is not required^{1,2}, and the state-of-the-art lasers and focal planes may be used for illumination and detection.

Conventional monopulse ladars have, however, two important drawbacks: (1) They are not robust in the presence of strong specular scattering components produced by the target glints or by optical countermeasures such as corner cubes³. (2) The telescope images may be highly degraded by the atmospheric turbulence, which severely limits their applicability as ground based ladars⁴. To overcome corner cubes as the countermeasures, one remedy is to separate the transmitter and the receiver, so that the receiver is kept away from highly directional corner cube reflections. In many situations such a bistatic configuration is not practical. Also, more progress is needed before the active methods for controlling the figure of large telescopes, and the adaptive optics designed for real-time compensation of atmospherically induced wavefront aberrations will meet some of the more challenging performance requirements.

Nonconventional active imaging sensor systems were proposed as an alternative to very large, expensive imaging telescopes using adaptive optics. We refer here to an imaging sensor as a nonconventional when: (1) the receiver antenna is noncoherent and consists of an array of photon buckets, and (2), the target images are obtained by processing the target interferograms^{5,6}.

* Patent pending.

The reconstructed images approach the diffraction-limited resolution of the noncoherent antenna when the target is within an isoplanatic patch of the atmospheric turbulence. Performance-degrading laser speckles, are the well known side-effect of coherent illumination. They can be reduced by ensemble averaging over a number of independent realizations of target interferograms prior to the reconstruction, or by ensemble averaging of images reconstructed from the individual interferograms.

Nonconventional imaging systems represent an attractive alternative to conventional imaging systems when it comes to high-resolution imaging. Another attribute of these type of sensors is their relative robustness to the presence of the strong specular components. These sensors cannot be used for the target position estimation, however, since a noncoherent array of photonsensors cannot measure the absolute value of the angle-of-arrival.

The CRITIC (Coherent Radiation Imaging and Tracking via Nonuniform Illumination) technique, which we propose in this paper, makes use of the attributes of both the conventional and the nonconventional imaging systems and is free from their drawback. The technique is introduced in the next section. In Section 3 we provide qualitative examples of the CRITIC's performance. The last section is a summary.

2. THE CRITIC

In this section we describe the CRITIC's transceiver and its operational principles.

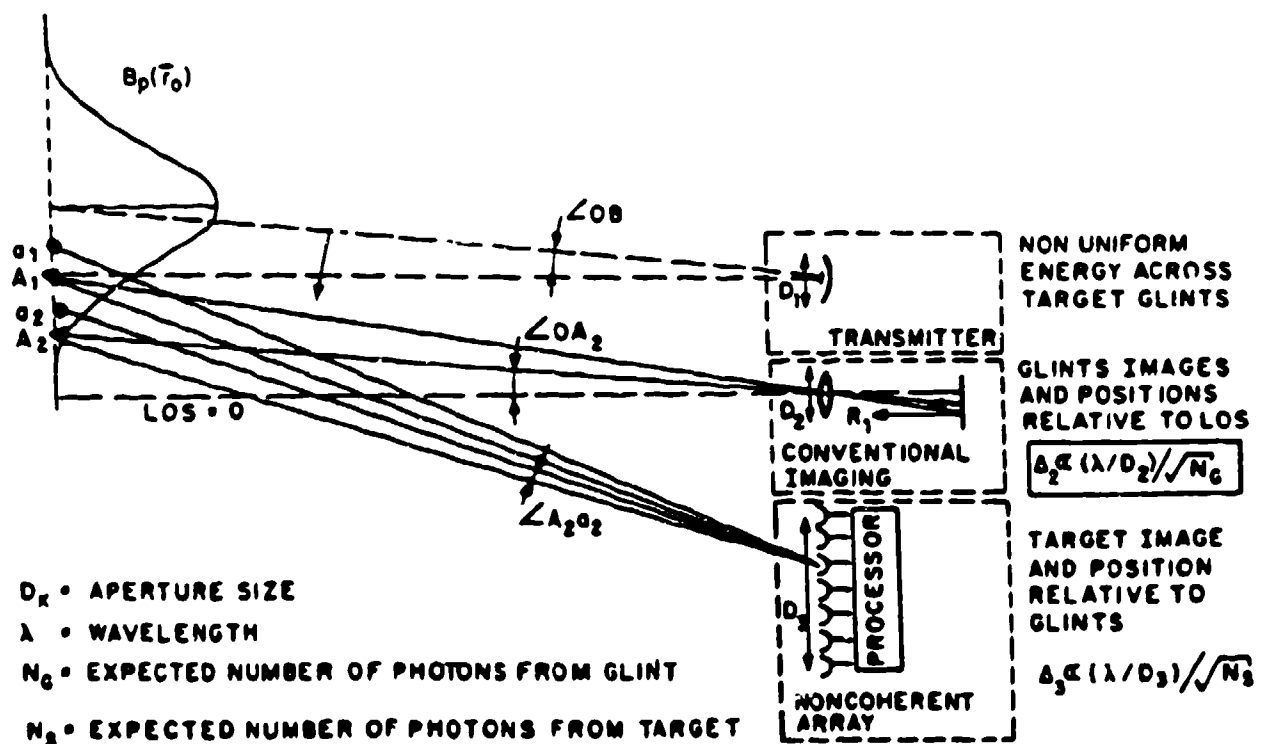


Figure 1. Schematic of the CRITIC Transceiver.

As seen in Fig. 1, the system receiver consists of two different imaging sensors: one is a conventional imaging system, in which telescope images are sensed at the focal plane with an array of photodetectors and another is a nonconventional imaging system consisting of a sparse array of photon buckets for sensing the target interferograms in the aperture plane. The diffraction-limited resolution of the telescope is typically much smaller than that of the noncoherent antenna.

A single transmitter is used by both imaging receivers. The transmitter delivers to the target a laser pulse with a known and nonuniform spatial intensity distribution in the target plane. As discussed below, the known beam nonuniformity is necessary for unambiguous reconstruction of target images from the interferograms recorded in the aperture plane. The transmitter and the receiver telescope are optically aligned with high precision. This alignment is required in order to measure the beam position across the target from the telescope images.

The telescope images and interferograms are collected and processed in parallel for each illuminating pulse. Whereas the telescope images are produced in a single pulse, the reconstruction of images from the interferograms may require more than one beam intensity distribution across the target and therefore more than one pulse.

The main idea behind the CRITIC is: (1) use the telescope images for measuring the angular position of specular elements, (2) use the interferograms to produce high resolution images of the diffuse elements by employing a technique recently invented by us called self-reference ambiguity-free holography⁹, (3) derive the angular positions of the target diffuse elements relative to the receiver LOS telescope by analyzing the images obtained with both receivers.

2.1 TARGET MODEL

The complex reflectance of the target can be modeled as:

$$a_T(\vec{r}_0) = \begin{cases} a(\vec{r}_0) + \lambda(\vec{r}_0), & \vec{r}_0 \in s \\ 0, & \vec{r}_0 \notin s \end{cases} \quad (1)$$

s is the target support, $a(\vec{r}_0)$ and $\lambda(\vec{r}_0)$ are the diffuse and specular components, respectively. The specular component is assumed to be deterministic and is due to the target glints or corner cubes. The diffuse component is due to an optically rough surface and is modeled as a complex circular Gaussian process:

$$\langle a(\vec{r}_0) \rangle = 0 \quad (1a)$$

$$\langle a(\vec{r}_0) a(\vec{r}'_0) \rangle = 0$$

$$\langle a(\vec{r}_0) a^*(\vec{r}'_0) \rangle = \langle |a(\vec{r}_0)|^2 \rangle \delta(\vec{r}_0 - \vec{r}'_0),$$

where $\langle \cdot \rangle$ stands for ensemble averaging. (In Fig. 1 we denote the diffuse components as a_1 and a_2 , and the specular components as A_1 and A_2 .)

2.2 CONVENTIONAL IMAGING SYSTEM

The image intensity distribution of a coherently illuminated target in the focal plane r_i is given by:

$$I(\vec{r}_i) = \int d\vec{r}_0 \int d\vec{r}'_0 a_T(\vec{r}_0) a_T^*(\vec{r}'_0) B(\vec{r}_0) B^*(\vec{r}'_0) h(\vec{r}_0 - \vec{r}_i) h^*(\vec{r}'_0 - \vec{r}_i), \quad (2)$$

where $B(\vec{r}_0)$ is the amplitude of the incident nonuniform illumination beam, and $h(\vec{r}_0 - \vec{r}_i)$ is the coherent point-spread function.

Consider, for example, the case in which the specular components are seen through the telescope as discrete point-like sources, and are several orders of magnitude brighter than the diffuse parts of the target, i.e.,

$$a_T(\vec{r}_0) = \lambda(\vec{r}_0) = \sum_{n=1}^N \lambda_n \delta(\vec{r}_0 - \vec{r}_n) \quad (3)$$

In Refs. 1 and 2, we analyzed methods of estimating the target position from its image under the following conditions: the image intensity has the form of Eq. 2; the intensity is sensed by an array of photodetectors with apertures smaller than the Airy disc of the imaging telescope; and the accuracy of measurement of any point source is not affected by the presence of others. Under these conditions, we have shown that the accuracy of measuring the angular position Δ_2 of a point source (see Fig. 1) is:

$$\Delta_2 = \gamma(\lambda/D_2) / \sqrt{N_g} \quad (4)$$

where λ is the illumination wavelength, D_2 is the diameter of the telescope aperture, γ is a constant which depends on the point-spread function, and N_g is the expected number of photocounts from a glint collected by all photodetectors. Eq. 4 is valid in the limit when the signal-generated shot noise is the dominant source of noise. Typically, practical considerations such as quality of the optics, finite extent of the "point" target, and nonuniformity of the focal plane do not allow one to improve the angular accuracy Δ_2 to less than $(\lambda/D_2)/(10 - 100)$ merely by increasing the signal.

In the CRITIC, the telescope images are used to measure the angular position of glints \vec{r}_n and their strength $|A_n|^2$. The angular position of glints is measured with accuracy better than the diffraction-limited resolution of the telescope (λ/D_2). According to Eq. 4, accuracy 100 times better than the diffraction-limited resolution can be achieved when a point-glint produces 10,000 photocounts (the constant γ , typically does not exceed unity)⁷. According to Eq. 2, measurement of the glint strength is possible when the illumination beam intensity is known across the target. In the CRITIC, the knowledge of the beam intensity distribution is achieved through optical alignment of the imaging telescope with the transmitter and the high beam quality. The accuracy of the optical alignment should be at least as good as the accuracy of the angular position estimation of the point-glints.

2.3 NONCONVENTIONAL IMAGING SYSTEM

The CRITIC's nonconventional imaging system, shown schematically in Fig. 1, is a noncoherent sparse array of photon buckets, which is used to detect interferograms created by the interference of all target components under the nonuniform illumination.

We view an interferogram of a complex target, as a hologram, in which the glints serve the role of holographic references. The classical off-axis holographic techniques are not useful, however, to extract the images from such an interferogram since the reference is on the target and there may be more than one reference. Under such conditions the conventional techniques will produce multiple overlapping images with unknown angular position relative to the receiver⁸.

The self-reference ambiguity-free holography which we recently proposed⁹ is capable of extracting the images of the diffuse parts of the target and measure their angular position relative to the nonuniform illumination beam.

2.3.1 SELF-REFERENCE AMBIGUITY-FREE HOLOGRAPHY

The principle of the CRITIC holographic technique is illustrated in Fig. 2 below:

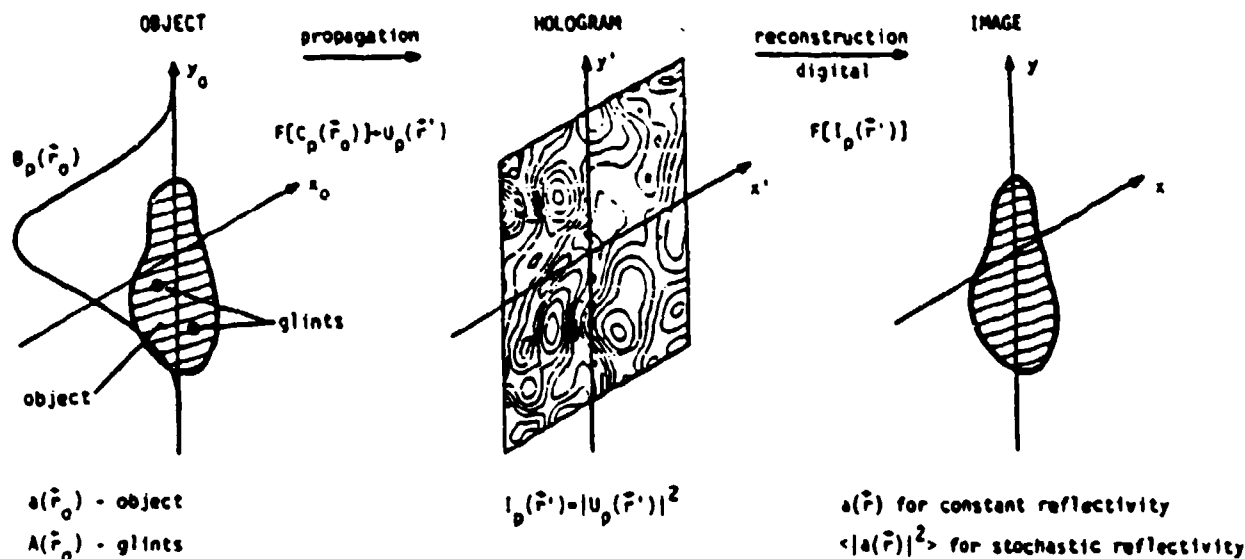


Figure 2. Schematic of Self-Reference Holographic Imaging.

The intensity distribution in the receiver plane at a distance z from the target may be written

$$I(\vec{r}') = \int d\vec{r}_0 \int d\vec{r}'_0 \bar{a}_T(\vec{r}_0) \bar{a}_T^*(\vec{r}'_0) B(\vec{r}_0) B^*(\vec{r}'_0) \exp \left[-i \frac{2\pi}{\lambda z} (\vec{r}_0 - \vec{r}'_0) \cdot \vec{r}' \right], \quad (5)$$

where $B(\vec{r}_0)$ is the amplitude of the incident nonuniform beam, and

$$\bar{a}_T(\vec{r}_0) \equiv a_T(\vec{r}_0) \exp \left[i \pi \vec{r}_0^2 / \lambda z \right]. \quad (6)$$

Taking the Fourier transform of the interferogram in Eq. (5) gives

$$F(\vec{z}) \propto \int d\vec{r}' \bar{a}_T(\vec{r}') \bar{a}_T^*(\vec{r}' - \vec{z}) B(\vec{z}') B^*(\vec{z}' - \vec{z}). \quad (7)$$

In the above equation, the effect of finite size of the receiver was neglected. The effect of the diffraction-limited resolution on the reconstructed images was investigated qualitatively and is illustrated in Section 3.

Further processing of information contained in Eq. (8) depends on the nature of target reflectivity. Consider for simplicity pointlike glint references. In this case the target reflectance may be written:

$$\bar{a}_T(\vec{z}) = \bar{a}(\vec{z}) + \sum_{n=1}^N \bar{A}_n \delta(\vec{z} - \vec{z}_n), \quad (8)$$

and the Fourier transform of the interferogram becomes

$$F(\vec{z}) \propto \bar{F}_{gg}(\vec{z}) + \bar{F}_{go}(\vec{z}) + \bar{F}_{oo}(\vec{z}), \quad (9)$$

where

$$\bar{F}_{gg}(\bar{z}) = \sum_{n=1}^N \sum_{m=1}^N \bar{A}_n \bar{A}_m^* B(\bar{z}_n) B^*(\bar{z}_m) \delta(\bar{z}_n - \bar{z}_m - \bar{z}) \quad (10)$$

describes interference between the glints;

$$\begin{aligned} \bar{F}_{g0}(\bar{z}) = & \sum_{n=1}^N \bar{A}_n^* B^*(\bar{z}_n) B(\bar{z}_n + \bar{z}) \bar{a}(\bar{z}_n + \bar{z}) \\ & + \sum_{n=1}^N \bar{A}_n B(\bar{z}_n) B^*(\bar{z}_n - \bar{z}) \bar{a}^*(\bar{z}_n - \bar{z}) \end{aligned} \quad (11)$$

is the interference between the glints and diffuse reflections; and lastly

$$\bar{F}_{00}(\bar{z}) = \int d\bar{z}' \bar{a}(\bar{z}') \bar{a}^*(\bar{z}' - \bar{z}) B(\bar{z}) B^*(\bar{z}' - \bar{z}) \quad (12)$$

is the autocorrelation function of the product of target reflectance and the beam amplitude distribution in the target plane.

For sufficiently strong glints ($|A_n| \gg |a(\bar{r})|$), the term $F_{00}(\bar{r})$ may be neglected. Since glint positions and amplitudes can then be determined with high precision by the conventional part of the system, the term $F_{gg}(\bar{r})$ can be removed from Eq. (5) by an appropriate processing. Therefore, we need to consider only the term $F_{g0}(\bar{r})$.

In order to obtain reconstructed images of diffuse targets it is useful to consider the correlation function:

$$C(\bar{z}) \equiv \langle \bar{F}_{g0}(\bar{z}) \bar{F}_{g0}^*(\bar{z}) \rangle \quad (13)$$

Using Eqs. (1a) and (11) we obtain

$$\begin{aligned} C(\bar{z}) = & \sum_{n=1}^N |A_n|^2 |B(\bar{z}_n)|^2 \left\{ |B(\bar{z}_n + \bar{z})|^2 \langle |a(\bar{z}_n + \bar{z})|^2 \rangle \right. \\ & \left. + |B(\bar{z}_n - \bar{z})|^2 \langle |a(\bar{z}_n - \bar{z})|^2 \rangle \right\}. \end{aligned} \quad (14)$$

This is an equation for $2N$ unknowns $\langle |a(\bar{r}_n + \bar{r})|^2 \rangle$ and $\langle |a(\bar{r}_n - \bar{r})|^2 \rangle$. The unknowns are solved by generating $2N$ equations, each resulting from a different beam position.⁹

Solution of Eq. 14 yields $2N$ images of the diffuse target; it is important to note that the position and orientation of each image is known with respect to positions of the glints. These images can be noncoherently combined to enhance the signal-to-noise ratio.

2.3.2 DESIGN CONSIDERATIONS

Target interferograms are spatially band-limited functions with the highest frequency determined by the target size. The highest spatial frequency dictates the smallest separation among the photon buckets in the array. The largest separation defines the receiver aperture and determines the diffraction-limited resolution of the array.

In the CRITIC architecture, the diffraction-limited resolution of the array is one or two orders-of-magnitude larger than that of the imaging telescope, i.e.:

$$(\lambda/D_3) = m(\lambda/D_2) , \quad (15)$$

where D_3 is the array aperture size, and m is always larger than unity and may be as large as a hundred. The resolution of the array, Δ_3 , depends on both the diffraction-limited resolution and the signal-to-noise considerations.

The resolution of the interferogram depends on the ability to measure the interference fringes between the diffuse and specular components. The signal is proportional to the product of their reflectivities weighted by the illumination intensity across them. Assuming orders-of-magnitude larger reflectivity for the glint, one deduces that in the shot noise limit, the glint is the main source of the noise, and the signal to noise ratio is proportional to the square root of the number of photons from the diffuse components of the target.

It is reasonable to expect that the resolution of the noncoherent array Δ_3 can not exceed,

$$\Delta_3 \approx (\lambda/D_3) / \sqrt{N_s} , \quad (16)$$

where N_s is the total expected number of photons from the diffuse elements. The overall performance is limited by the poorer of the two resolutions Δ_2 and Δ_3 .

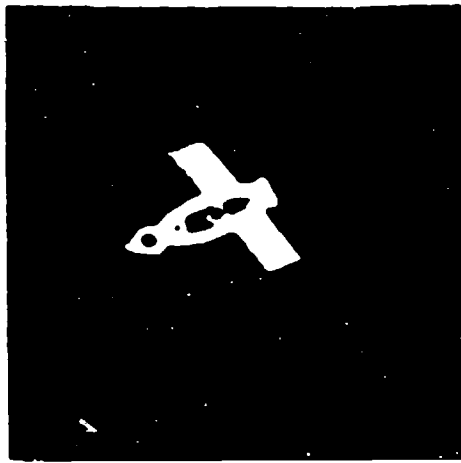
In the CRITIC technique, the transmitter is used to code the target reflectance with the laser illumination. By illumination coding we understand here that the nonuniform distribution of laser intensity is known across the target. As we stressed in the section 2.3.1, the intensity coding is the key for unambiguous reconstruction of the target images from their interferograms.

The longitudinal coherence of the laser illuminator must be at least twice the maximum path length difference between the target elements. The necessary laser power can be deduced from the system resolution requirement. The sufficient laser power is larger and depends on specific target and system characteristics, which must be taken into account in a quantitative analysis of the sensor system performance.

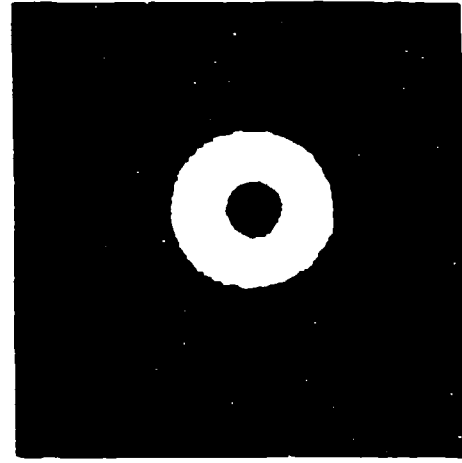
3. CRITIC PERFORMANCE: AN EXAMPLE

In this section we present results of computer simulations of the CRITIC performance in the strong signal limit, where the main source of error is due to the stochastic nature of the backscattered field arising from the random, target-induced phase modulation which results in the well-known phenomenon of the laser speckle.

We considered a model of a complex target shown in Fig. 3A illuminated by a Gaussian beam shown in Fig. 3B, with half-width equal to the target length. The locations of "glints" are indicated by dots. The amplitude of the "glint" in the center is 10^3 stronger than that from any diffuse element. The other "glint" is 10^2 stronger. The weaker "glint" models a strong specular component from, for example, a satellite, whereas the stronger "glint" models a corner cube.



A



B

Figure 3. Models of a Target and Illuminating Beam.

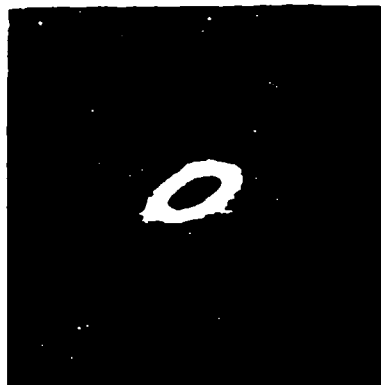
A CRITIC transceiver is used for imaging the target and estimating its position. Figure 4 shows images of the target obtained with the conventional telescope receiver considered for CRITIC in this example. Fig. 4A shows the target image under incoherent illumination and in the absence of glints, to give an example of the telescope diffraction-limited resolution. Fig. 4B is a realization of the telescope image when illumination is coherent. The diffraction-limited resolution is represented by the laser speckle size. We see that the resolution of the selected telescope is too poor to recognize the target from a single realization of the image, due to the noise-like laser speckle. Figures 4C and 4D are the telescope images of the target in the presence of the weaker and stronger glints, respectively. As expected, the telescope images show a point-like targets whose position can be found very accurately, but not a trace of the much weaker diffuse elements of the target can be found.

However, by shifting the Gaussian illumination beam to a different position and using the two different resulting holograms, we obtain, with our holographic technique, a target image shown in Fig. 5C. This image was obtained with a uniformly sampling array of photon buckets with an aperture four times larger than that of the telescope. Fig. 5D shows the reconstructed target image after averaging over 100 realizations of the laser speckles for each of the two beam positions. For completeness, Fig. 5B illustrates the expected failure of the conventional holographic method to produce the target image. The importance of the results in Fig. 5 is that they show target images which are produced simultaneously by the two sensors employed by the CRITIC system. Indeed, one can find the glint position (Fig. 5A) and have high-resolution images (Figs. 5C and D).

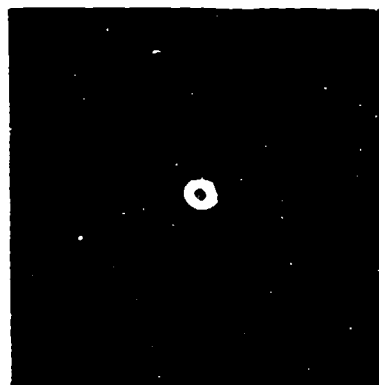
In Fig. 6 we show similar target images obtained with the CRITIC system for the case of a strong glint located in the middle of the target. The noise at the edges of Figs. 6C and D is an artifact due to the single-precision Fourier transformation used for the reconstructions, while the dark horizontal lines in the target images in Figs. 6C and D are the artifacts of the specific algorithm used.

In Fig. 7A we show a single realization of the target image in the presence of two glints: the weaker at the top of the target and the stronger in the middle. Images in Figs. 5A and 6A and 7A were simulated for the same illumination and receiver telescope. Our holographic technique, used with the same array of photon buckets as before, produces images shown in Figs. 7B, C and D after 1, 10, and 100 realizations for each of the four different beam positions across the target, respectively.

We have identified several promising candidate algorithms, in addition to those used to produce the results shown above. We continue our research to explore the CRITIC technique to its fullest potential.



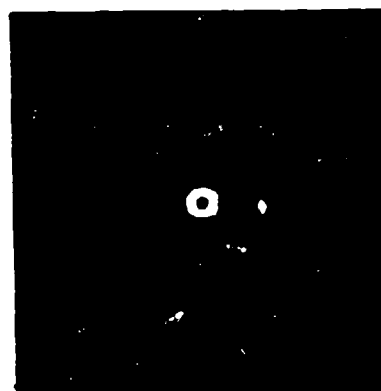
**A: Non-coherent
illumination**



**C: Coherent
illumination,
Glint = 10^2
(1 realization)**



**B: Coherent
illumination,
No Glints
(1 realization)**

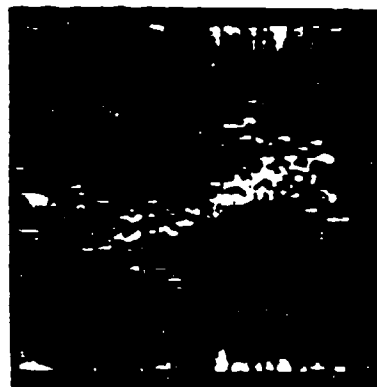


**D: Coherent
illumination,
Glint = 10^3
(1 realization)**

Figure 4. Telescope Images.



**A: Conventional
Image**



**C: Non-conventional
Reconstruction
(1 realization)**

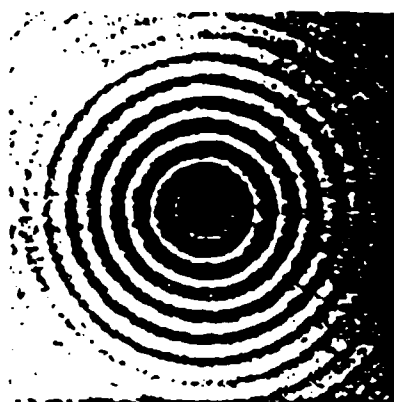


**B: Conventional
Holographic
Reconstruction**



**D: Non-conventional
Reconstruction
(100 realizations)**

Figure 5. CRITIC Images for Glint Strength = 10^2 .



**A: Conventional
Image**



**C: Non-conventional
Reconstruction
(1 realization)**



**B: Conventional
Holographic
Reconstruction**



**D: Non-conventional
Reconstruction
(100 realizations)**

Figure 6. CRITIC Images for Glint Strength = 10^3 .



**A: Conventional
Image**



**C: Non-conventional
Reconstruction
(10 realizations)**



**B: Non-conventional
Reconstruction
(1 realization)**



**D: Non-conventional
Reconstruction
(100 realizations)**

Figure 7. CRITIC Images for Two Glints (10^2 and 10^3).

4. SUMMARY

A novel lidar system is proposed to achieve high-resolution imaging and precision tracking of complex targets from a ground-based or space-based platforms. The system is based on the CRITIC technique in which telescope images of glints are produced simultaneously with holographic images of the diffuse target components obtained through a novel self-reference holographic imaging technique reported by us recently. In the technique, the glints are used as holographic references for the much weaker diffuse elements, which are uniquely coded by the nonuniform coherent laser illumination. By integrating into one system the imaging telescope of modest diffraction-limited resolution with a noncoherent array of photon buckets with an order-of-magnitude larger diffraction-limited resolution, the CRITIC overcomes several drawbacks of the conventional monostatic laser radars and the aperture plane interferometric receivers, while preserving all their attributes.

5. REFERENCES

1. Elbaum, M., Diament, P., King, M., and Williamson, B., "Maximum Angular Accuracy of Pulsed Radar in Photocounting Limits", *Applied Optics*, 16, (1977), p. 1982.
2. Elbaum, M., Diament, P., "Estimation of Image Centroid, Size and Orientation with Laser Radar", *Applied Optics*, 16, (1977), p. 2433.
3. Nowakowski, J., Gorlin, Y., Elbaum, M., "Effect of Target Signatures on Active Tracking". *Proceedings of SPIE*, Vol. 641, (1986), p. 10.
4. Goodman, J.W., *Statistical Optics*, Chapter 8, Wiley, New York, 1985.
5. Elbaum, M., King, M., Greenebaum, M., "Laser Correlography: Transmission of High Resolution Object Signatures Through the Turbulent Atmosphere", RRI Technical Report T-1/306-3-11, 1974.
6. Idell, P., Fienup, J.R., Goodman, R.S., "Image Synthesis from Nonimaged Laser Speckle Patterns", *Optics Letters*, Vol. 12, No. 11, November 1987.
7. Nowakowski, J., Elbaum, M., "Fundamental Limits in Estimating Light Pattern Position", *J. Opt. Soc. Am.* 73, (1984), p. 1744.
8. Goodman, J.W., "Introduction To Fourier Optics", McGraw Hill, New York, 1968.
9. Elbaum, M., Nowakowski, J., Gutkowitz-Krusin, D., Wlodawski, M., and Gorlin, Y., "Self-Reference Holographic Imaging Using Nonuniform Illumination", *Optics Letters*, 13, (1988), p. 81.

ACKNOWLEDGEMENT

The authors wish to thank Ms. J. Tyson and Mr. J. Walls for their able assistance in preparing the manuscript of the paper.

This research was sponsored in part by the ONR Contract "Innovative Techniques for High-Resolution Imaging and Precision Tracking".